UNIVERSIDAD DE CHILE
FACULTAD DE CIENCIAS FÍSICAS Y MATEMÁTICAS
DEPARTAMENTO DE ASTRONOMÍA

ESTUDIO DE SISTEMAS PLANETARIOS DE PERIODO CORTO ALREDEDOR DE ESTRELLAS GIGANTES

TESIS PARA OPTAR AL GRADO DE DOCTOR EN CIENCIAS, MENCIÓN ASTRONOMÍA

MATÍAS IGNACIO JONES FERNÁNDEZ

PROFESOR GUÍA:

PATRICIO ROJO RUBKE

MIEMBROS DE LA COMISIÓN:

JAMES JENKINS
CLAUDIO MELO
ALEKSANDER WOLSZCZAN
RENE MENDEZ BUSSARD
SEBASTIAN LOPEZ MORALES

SANTIAGO DE CHILE
ENERO 2013

Resumen

A la fecha más de 800 exoplanetas han sido detectados, la mayoría de ellos mediante el método de velocidad radial (VR). De forma tal de obtener VR's precisas, el espectro estelar debe contener miles de líneas de absorción delgadas, lo cual restringe ésta técnica a ser aplicada principalmente en estrellas de secuencia principal (SP), de tipos espectrales FGK ($M \lesssim 1.3 M_{\odot}$). Sin embargo, luego de la SP, estrellas tempranas (A y F) se expanden, por lo tanto se enfrían, y disminuyen su velocidad de rotación (Schrijver & Pols 1993), presentando un espectro rico en líneas espectrales delgadas. Por lo tanto, estrellas evolucionadas son un caso ideal para aplicar ésta técnica para detectar planetas alrededor de estrellas de masa intermedia ($1.3 \lesssim M/M\odot \lesssim 3.0$) y para estudiar el efecto de la interacción entre el planeta y su estrellas huésped.

Durante la última década, varios planetas han sido encontrados alrededor de estrellas post-SP, los cuales han revelado propiedades orbitales que contrastan con aquellos alrededor de estrellas de SP. En particular, se observa una falta de exoplanetas orbitando a menos de 0.6 AU de la estrella húesped, lo cual ha sido interpretado como la evidencia observacional de la destrucción de estos cuerpos durante la época de expansión del radio estelar, debido a la interacción de marea entre ambos cuerpos (e.g. Villaver & Livio 2009). Sin embargo, el efecto de la masa estelar también juega un papel importante en este resultado empírico (Johnson et al. 2007).

En ésta tesis se presenta un extenso estudio de VR's precisas, aplicado a una muestra de 166 estrellas gigantes. El objetivo principal de este estudio es la búsqueda de exoplanetas gigantes alrededor de tales estrellas, con el objetivo de determinar cúal es el rol de la evolución estelar en las órbitas de los planetas de período corto. Durante este proyecto, tres planetas masivos han sido descubiertos, todos ellos con distancia orbital mayor a 0.57 AU, alrededor de estrellas que recién comienzan la etapa gigante. Con los datos obtenidos durante éste

proyecto y aquellos publicados en la literatura científica, no es posible separar el efecto de la evolución estelar del efecto de la masa de la estrella huésped, por lo cual aún no es posible concluir en favor o en contra del mecanismo recientemente nombrado.

Abstract

To date, more than 800 exoplanets have been detected, most of them by the radial velocity (RV) technique. In order to achieve high enough RV precision, the stellar spectrum of the host star has to contain thousands of narrow absoprtion lines, which restricts this method mainly to FGK main-sequence stars ($M \lesssim 1.3 M_{\odot}$). However, after the main-sequence, earlier spectral type stars (A and early F) expand, hence becoming cooler and rotate slower than their former main-sequence progenitors (Schrijver & Pols 1993), hence presenting a spectrum containing thousands of narrow absorption lines. Therefore, evolved stars present an ideal case where we can use the RV technique to search for planets orbiting intermediate-mass ($1.3 \lesssim M/M\odot \lesssim 3.0$) stars and to investigate the effect of the post-MS star-planet interactions.

During the last decade, several exoplanets were detected around post-MS stars, revealing different properties than those orbiting solar-type stars. In particular, the semimajor axis distribution shows a lack of planets orbiting interior to 0.6 AU, which has been interpreted as the observational evidence of the engulfment of planets due to tidal decay (e.g. Villaver & Livio 2009). However, the effect of the stellar mass is also playing a role, which might be in part responsible for this observational result (Johnson et al. 2007).

In this dissertation a large RV study of 166 giant stars is presented. The main goal of this survey is to search for giant planets in close-in orbits, and to determine whether the effect of the stellar evolution is responsible for the observed lack of short period orbit planets around post-MS stars. During this project, three massive giant planets were detected, all of them having orbital distances greater than 0.57 AU, around first ascending giant branch stars. With the current statistics for these kind of objects, is not possible to dissentangle the effect of the stellar mass from the stellar evolution, thus there is still no conclusive evidence in favor of the afore mentioned mechanism.

DEDICATORIA

A mi estrella favorita, mi Trinita

Contents

List of Figures

List of Tables

Chapter 1

Introduction

Twenty years ago, Wolszczan & Frail (1992) announced the detection of a planetary system around the pulsar PSR 1257+12, based on the study of the variation of the pulsar period. At the time, this discovery was very controversial since one year before Bailes et al. (1991) announced a similar result, which was discarded by the same group several months later (Lyne & Bailes 1992). In addition, since pulsars are the remnants of the explosion of massive stars, no planet was expected to be found around them. However, three years later, by measuring the doppler shift of stellar absorption lines, Mayor & Queloz (1995) detected a Jupiter-mass planet (51 Peg b) around a solar-like star in a 4 days orbit[1], which was also surprising since giant planets (like Jupiter or Saturn) are expected to be formed beyond the snow line. This new discovery not only confirmed the presence of planets orbiting stars other than the sun (hereafter exoplanets), but also showed that, as in the case of the planetary system around PSR 1257+12, planets live in environments where they were not thought to exist.

These two discoveries revolutionazed modern Astronomy, opening a new field of investigation, that has experienced a very rapid growth in the last 15 years. Nowaday, hundreds of exoplanets have been detected, covering a wide range of masses, eccentricities and orbital periods. These planets have been found orbiting very different stars, having different masses, ages and enviroments. Among them, it is worth to highlight some recent discoveries such as

[1]These kind of planets were afterwards dubbed as "*Hot Jupiters*"

the transiting planet orbiting two stars (Doyle et al. 2011), a planetary system including up to seven members (Lovis et al. 2011), a Super-Earth in the habitable zone (Anglada-escude et al. 2012), an Earth-mass planet orbiting α Centauri B (Dumusque et al. 2012) and the multiple system detected around the radial velocity "stable" star τ Ceti (Tuomi et al. 2012).

1.1 Detection methods

In order to detect exoplanets, several different method have been developed, namely, the radial velocity (RV) technique, pulsar timing, the planet transit method, astrometric measurements, the microlensing technique, and more recently by direct imaging. The basic ideas behind these techniques are discussed in the following sections.

1.1.1 Astrometry

This method consists of measuring the position of the host star on the sky, in order to detect small variations that are induced by an orbiting planet. Considering that both the star and the planet orbit around the common center of mass, the expected amplitude of the ellipse described by the star (after correcting for the stellar parallax and proper motion) is given by:

$$a_\star = \frac{a_P \, M_p}{M_\star} \tag{1.1}$$

where $a_\star$ and a_p are the orbital distance of the host star and the planet around the center of mass of the system. $M_\star$ and M_p are their corresponding masses. Equation 1.1 shows that this technique is more effective for massive planets orbiting at large distances from the star. Certainly close-in planets are more difficult to be detected by this method. Figure 1.1 shows the angular amplitude in the sky as a function of the distance to the star for a 1.0 M_J size planet orbiting at 3 AU (black solid line) and a 0.5 M_J planet at 1 AU (dashed blue line). In both cases the mass of the host star was fixed to 1.0 $M_\odot$. As can be seen, the angular precision needed for such detections are below one miliarcsecond. Future missions such as

GAIA will be able to resolve angular variations at the $\sim 10\ \mu$arcsec level, making possible the detection of rocky planets orbiting nearby stars. The main advantage of this technique is that its sensitivity increases with the orbital distance, hence it is complementary to the RV technique, which is more sensitive to the inner region of planetary systems. However, very precise measurements of nearby stars have to be taken during several years in order to obtain a reliable astrometric solution. Also, starspots produce astrometric signals at the $\sim$ 10 micro arcseconds level in nearby solar-type stars (Hatzes 2002).

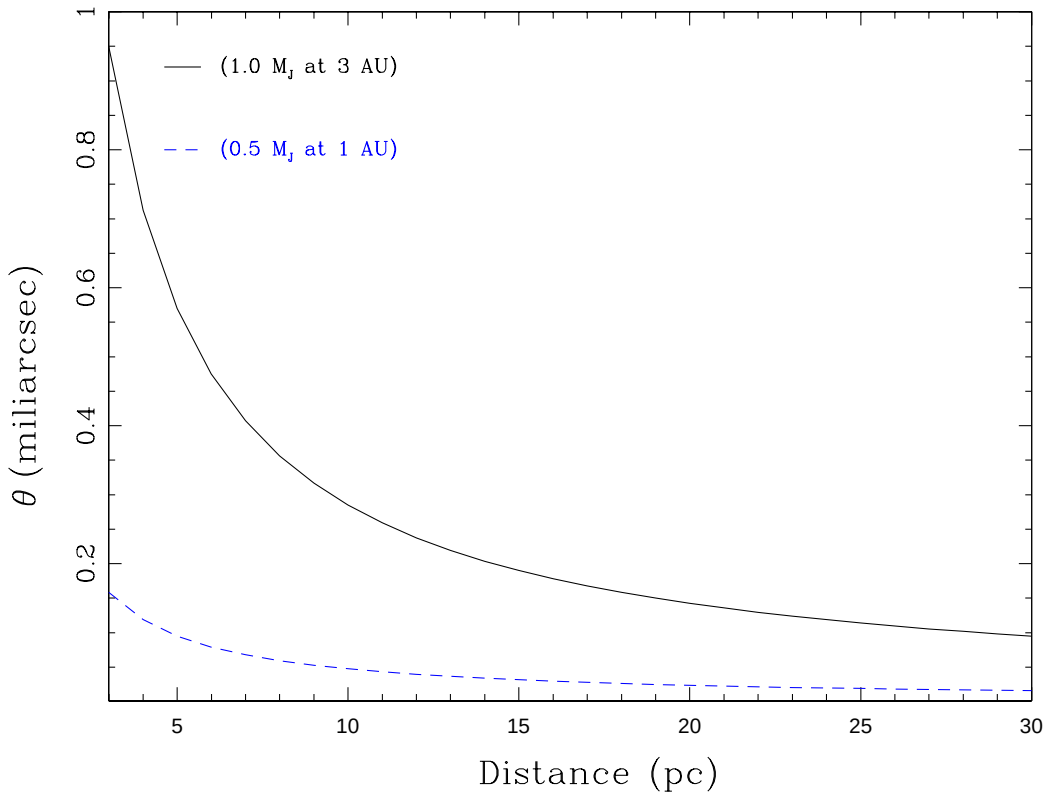

Figure 1.1: Astrometric amplitudes induced by an orbiting planet, as a function of the distance to the star. The black solid line corresponds to a 1.0 M_J planet orbiting at a distance of 3 AU, while the blue dashed line corresponds to a 0.5 M_J mass planet orbiting at 1 AU. In both cases the mass of the star was fixed to 1.0 $M_\odot$.

1.1.2 Transit method

When the orbital plane of the planet is aligned with the observer line of sight, then the transit of the planet that is passing in front of the star can be observed, in a similar way that Mercury and Venus passes in front of the Sun. However, it is not possible to observe spatially resolved transits in exoplanets. Instead, it is possible to measure the decrease of the stellar flux (Δf) during the transit, whose maximum is given by:

$$\frac{\Delta f}{f} = \left(\frac{R_P}{R_\star}\right)^2 \tag{1.2}$$

where f is the off-transit flux of the star, R_p is the planet's radius and $R_\star$ the star's radius. Since Δf is affected by a differential limb darkening in the stellar disk, is not straightforward to measure an arbitrarily accurate depth. Figure 1.2 shows the fraction of the flux blocked by the transiting planets as a function of the planet's radius. The black and blue lines correspond to a radius of 1.0 $R_\odot$ and 0.6 $R_\odot$ for the host star. It can be noticed that, for instance, Jupiter produces a $\sim$ 1 % decrease in the stellar flux when passing in front of the Sun, whereas the Earth ($R \sim 0.1\ R_J$) blocks only $\sim$ 0.01 % of the light. When the RV curve of the star is available, the shape and duration of the transit provide the orbital inclination, hence the planet's orbital and physical properties (M_P, R_P, a_P, e) can be fully derived. This method, is highly complementary with the RV technique as the combination of both gives us the planet's mass and density. Unfortunately, this method has the disadvantage that the transit probability is very low ($\sim$ 0.5 % for the Earth and $\sim$ 10 % for a *Hot Jupiter*), and considering typical photometric precision, it is mostly sensitive to large planets using ground based telescopes. However, space missions like KEPLER (precision better than 20 ppm for a V=12 mag star), have already detected around 2000 planet candidates (including a bunch of rocky planets) by this technique. In Figure 1.3 a schematic diagram of 5 confirmed transiting planets in the Kepler's field is shown. As can be noticed the amount of flux blocked by the transiting planets is below 1 %. Also, all of them are in short period orbits (P < 5

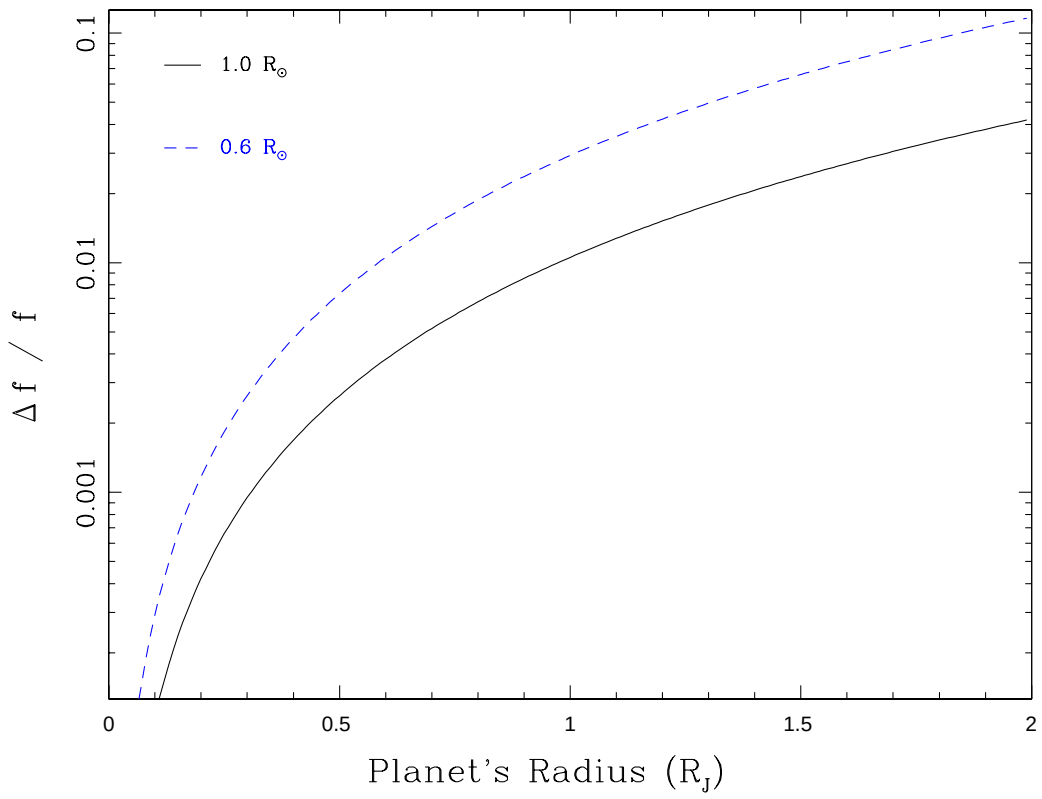

Figure 1.2: Transit depth as a function of the planet's radius. The solid black line and the dashed blue line correspond host stars with $R_\star = 1.0\ R_\odot$ and $R_\star = 0.6\ R_\odot$, respectively.

days), since as mentioned above, the probability of having a transit decreases linearly with the orbital distance.

During the transit, it is also possible to study the atmosphere of the planet via transmission spectroscopy or occultation. In the former case part of the stellar light crosses the planet's atmosphere, superimposing the absorption features of the elements present there in the stellar spectrum. This method has allowed us to detect the presence of different elements in the atmospheres of several transiting planets (e.g. Charbonneau et al. 2002). Also the thermal emission of the planet can be measured by substracting the stellar flux (measured during the secondary eclipse when the planet is passing behind the star) from the total flux of the system (star + planet emission; e.g. Zhao et al. 2012).

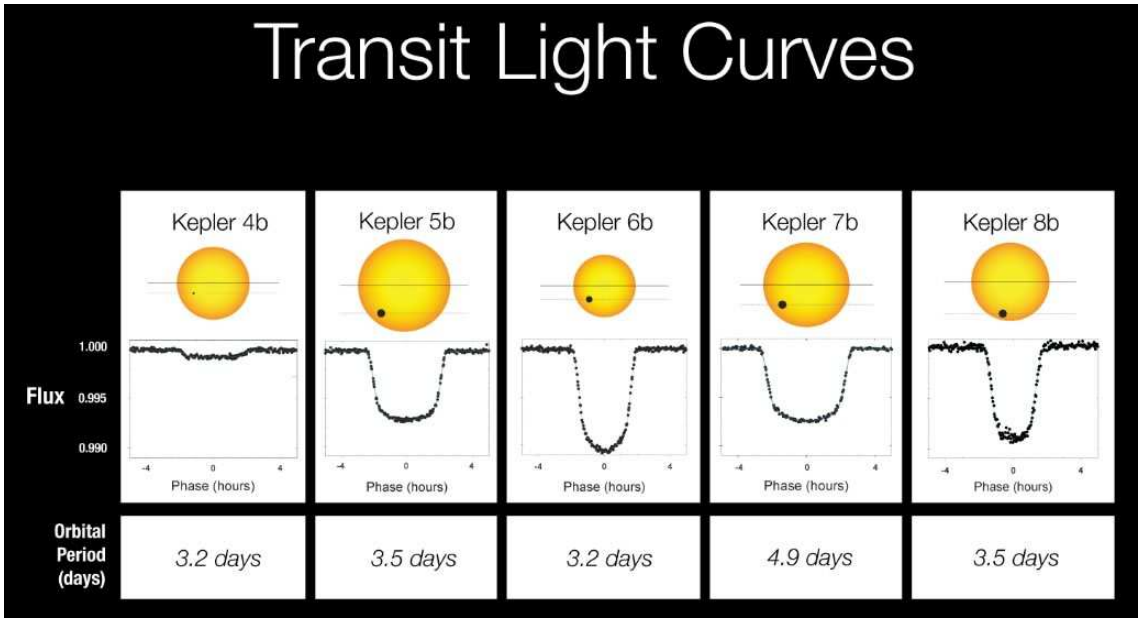

Figure 1.3: Schematic diagram of 5 transiting planets detected bty the Kepler mission. Image credit: NASA/Kepler

An extension of the transit technique is the so called TTV (*Transit Timing Variation*). The basic idea of this technique is to measure the variations in the predicted central time of the transit, which is attributed to the presence of other substellar objects that are perturbing gravitationally the orbit of the transiting planet.

1.1.3 Gravitational Microlensing

The microlensing effect is based around measuring the the temporal increase of the apparent brightness of an object, which is produced by the re-focusing of the light of the source in the direction to the observer, by some intervening object acting as a gravitational lens. This effect is explained by the curvature of the time-space produced by a compact object, as predicted by Einstein's General Relativity. This principle can be used to detect planets that induce a temporal magnification of the source brightness. However, this effect can only be measured when two stars, the source and the lensing system (a star hosting a planet) are more or less aligned and the planet produces an additional magnification effect, which is superimposed to

the one produced by the lensing star. The main advantage of this technique is that planets can be detected very far away from us, up to several kiloparsecs, and with very wide orbits. The disadvantages are the low probability of these events (low probability of the two stars alignment), and that the event will not be repeated (since stars are moving respect to each other).

1.1.4 Direct Imaging

The detection techniques presented in last few sections are based on indirect methods to detect the presence of a planet. The angularly resolved detection of exoplanets is extremely challenging because of the small angular separation between the planet and the parent star and due to the large ratio between their fluxes. However, with the use of new technologies

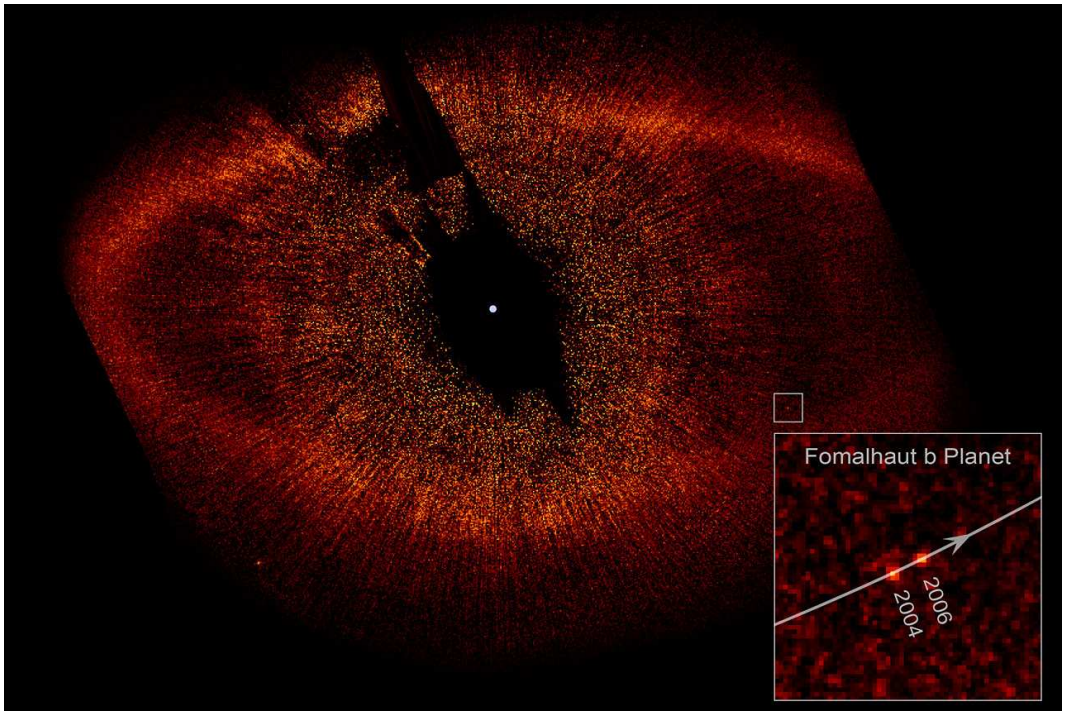

Figure 1.4: Image of Formalhaut and its orbiting planet. Image credit: NASA, ESA and P. Kalas (University of California, Berkeley, USA)

(such as coronographs) it has been possible to directly observe substellar companions around several stars. The first direct images of extrasolar planets came just a few years ago, with the discovery of a giant planet around a brown dwarf (Chauvin et al. 2004). More recently,

Marois et al. (2008) found a multiple planets system around the star HR 8799, all of them orbiting beyond 20 AU from the host star. At the same time, Kalas et al. (2008) observed a planet orbiting in the dusty belt around the star Formalhaut. The latter system is shown in Figure 1.4, where the displacement of the planet is also shown between 2004 and 2006. To date, several other systems have been detected by this method, using different instruments and techniques. The main advantage of this technique is that it is sensitive to planet in wide orbits, hence allow us to probe the outer part of planetary systems aswell as directly measure the thermal emission and spectral properties of the planet.

1.1.5 Pulsar Timing

The Pulsars are extremely precise cosmic clocks, as they emit regular radio frequency pulses induced by their strong magnetic fields generated by their fast rotation. However, in the presence of a stellar or substellar companion, the effect of their orbital motion around the center of mass of the system, translates into a periodic increase and decrease in the frequency of the pulse, due to the difference in the path traveled by the light emitted by the pulsar. For a planet in a circular orbit, the maximum difference in the time of arrival of the pulse is given by:

$$\Delta t = \left(\frac{a_P \sin i}{c}\right) \left(\frac{M_P}{M_\star}\right) \tag{1.3}$$

where a_p is the orbital distance of the planet, respect to the system's center of mass, i is the inclination angle of the orbit and c is the speed of light. M_P and $M_\star$ correspond to the mass of the planet and the pulsar, respectively. In Figure 1.5 the time delay amplitude in the orbital distance versus planet's mass plane is plotted. The orbits are assumed to be circular having an inclination angle $i = 90$ degrees. The mass of the pulsar was set to 1.4 $M_\odot$. The positions of the rocky planets in the Solar System are also shown. Since the typical precision achieved is ~ 1 μ s (lower line in Figure 1.5), it is possible to detect moon-sized objects and small asteroids in wide orbits.

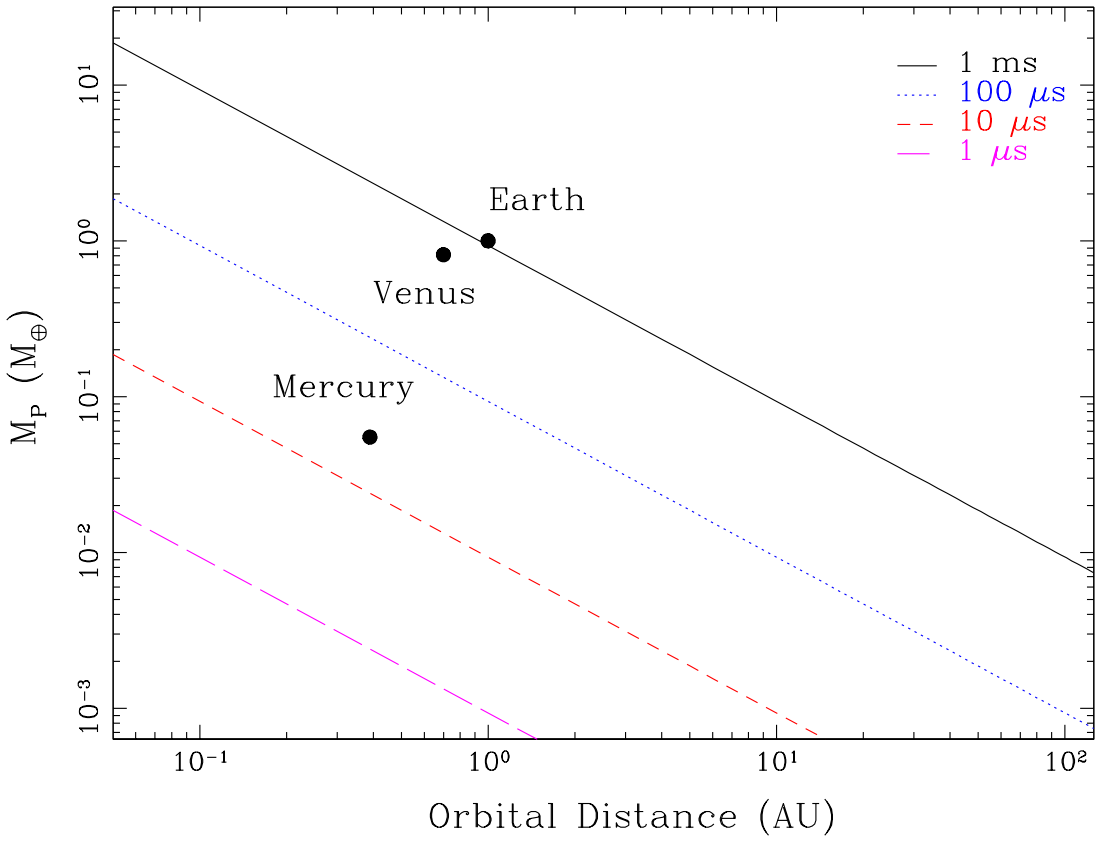

Figure 1.5: Maximum time delay observed in the pulsar frequency in the orbital distance versus planet's mass plane. The lines from bottom to top correspond to time delay amplitudes of 1, 10, 100 and 1000 μs, respectively. The orbital inclination angle is assumed to be i=90 degrees and the mass of the star is fixed to 1.4 $M_\odot$. The position of the inner planets in the solar systems are also labelled.

1.1.6 The Radial Velocity Technique

Among the detection methods developed for planet searches, the RV technique has been the most successfull one in terms of the rate of discoveries (around 500 exoplanets confirmed as of December of 2012[2]). The basic idea behind this technique is to measure the doppler shift induced by the gravitational pull of a substellar companion. This effect can be measured from the shifts in the position of the stellar spectral features, which are related to the stellar radial velocity relative to the observer simply by (in the non-relativistic regime):

[2]source: http://exoplanet.eu/

$$\frac{v}{c} = \frac{\Delta\,\lambda}{\lambda} \tag{1.4}$$

where v is the velocity of the star in the direction of the observer and c is the speed of light. $\Delta\,\lambda$ correspond to the wavelength shift at the wavelength λ. Since the velocity of the star along its orbital motion around the star-planet center of mass varies with time, the doppler shift measured from the stellar spectrum follows a periodical variation having the following form:

$$V_r(\nu) = K\,(cos(\nu + \omega) + e\,cos(\omega)) \tag{1.5}$$

where ν is known as the *true anomaly*, and corresponds to the angle between the periastron and the position of the planet, measured from the center of mass of the system, that corresponds approximately to the position of the host star. ω is a fixed quantity usually called as *argument of periastron or argument of periapsis* and corresponds to the angle between the line of nodes and the periastron, while e is the eccentricity of the orbit. Figure 1.6 shows a schematic diagram with the orbital elements of the planet.

The proportional constant K is the amplitude of the radial velocity curve, which is given by:

$$K = \frac{28.4}{\sqrt{1-e^2}} \left(\frac{M_p \sin i}{M_J}\right) \left(\frac{M_\star}{M_\odot}\right)^{-1/2} \left(\frac{a}{AU}\right)^{-1/2} \tag{1.6}$$

where M_p, $M_\star$ and a correspond to the mass of the planet, the mass of the star and the semimajor-axis, respectively. The i angle, corresponds to the inclination between the planet orbit and the plane of the sky, which is perpendicular to the observer's line of sight. The last formula is valid only when the mass of the star is much larger than the mass of the planet, i.e., $M_\star \gg M_p$. Figure 1.7 shows the RV amplitude K in the a-M_p plane, for planet orbiting a 1.0 $M_\odot$ star. The three lines from bottom to top correspond to RV amplitudes of 0.1 $m\,s^{-1}$, 1.0 $m\,s^{-1}$ and 10.0 $m\,s^{-1}$, respectively. The position of the the Earth, Jupiter and Saturn are

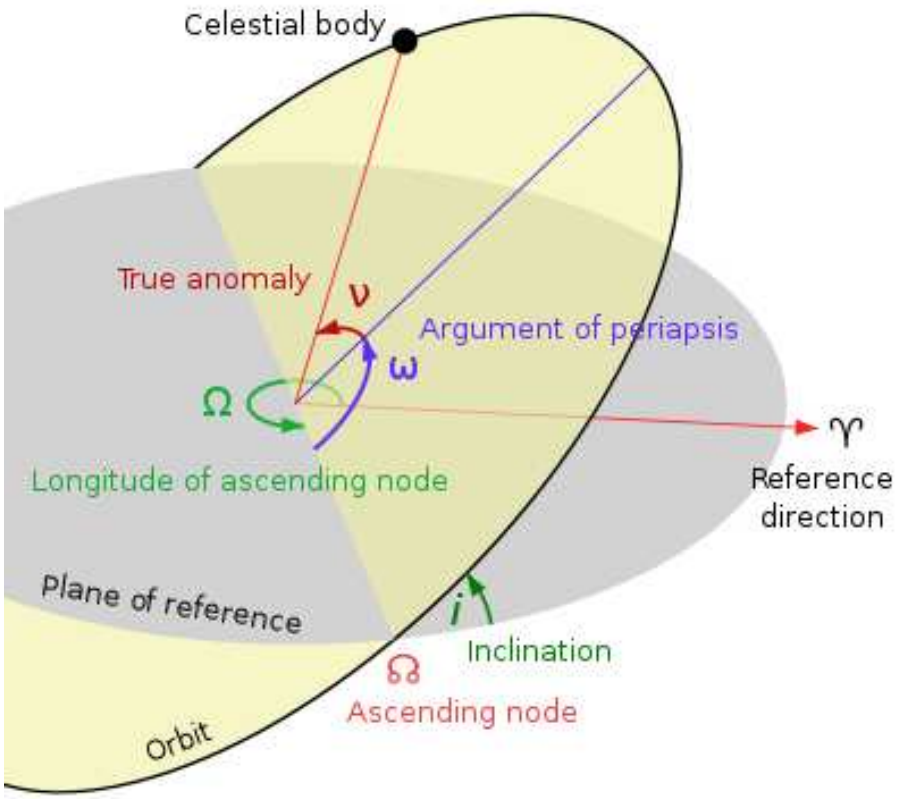

Figure 1.6: Schematic diagram of the planet's orbital elements. The reference direction is perpendicular to the observer's line of sight.

also plotted. As can be seen, a planet similar to the Earth would be barely detectable with a 10 $\mathrm{cm\,s^{-1}}$ precision.[3] Planets similar (in mass and orbital distance) to Saturn and Jupiter can easily be detected with the current instrumentation.

In order to convert from ν (which is not a direct observable quantity) into time, two trascendental equations are used:

$$\frac{2\,\pi\,(t - T_p)}{P} = E - e\,sin\,E \tag{1.7}$$

$$tan\left(\frac{\nu}{2}\right) = \left(\frac{1+e}{1-e}\right)^{1/2} tan\left(\frac{E}{2}\right) \tag{1.8}$$

[3]The next generation of high precision spectrographs such as ESPRESSO at VLT (first light schedule for 2016) are expected to reach ~ 10 $\mathrm{cm\,s^{-1}}$ level precision.

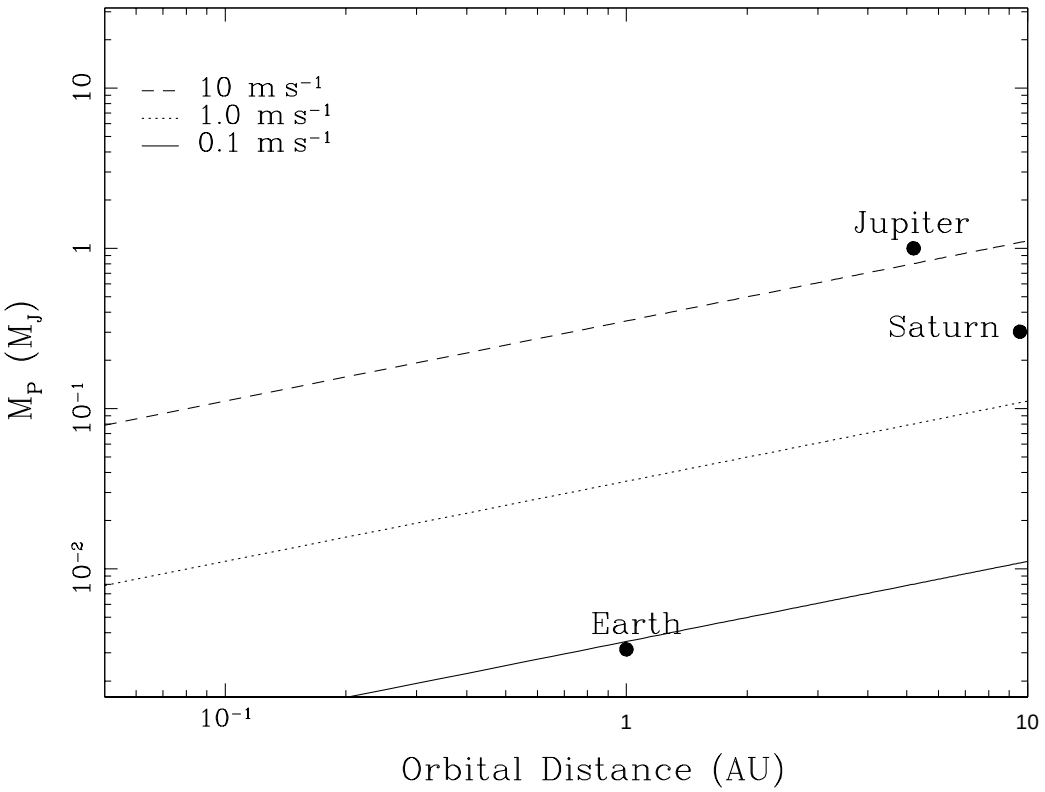

Figure 1.7: Radial velocity amplitude in the a-M_P plane. The lines from bottom to top correspond to K = 0,1, 1.0, 10 $m\,s^{-1}$. The mass of the parent star is fixed to 1.0 $M_\odot$.

where P is the orbital period and T_p is the time of periastron passage. These two equation can be solved numerically, and hence it is possible to derive the radial velocity variations of the star as a function of time.

With the current instrumentation (e.g. HARPS mounted on the 3.6 m telescope, at La Silla) it is possible to reach a single shot RV precision below $\sim 1\ m\,s^{-1}$, allowing us to detect planets having masses comparable to the mass of the Earth (e.g. Pepe et al. 2011; Forveille et al. 2011; Dumusque et al. 2012; Tuomi et al. 2012). Adittionally, the use of a laser comb [4] (which is under construction), will be used to compute a much more precise wavelength calibration through all of the optical range, allowing to improve the RV precision down to $\sim$

[4]The laser comb produces a uniformly distributed set of emission lines which are then used to derive a very high accuracy ($\sim 10\ cm\,s^{-1}$) wavelength solution

$30\ \mathrm{cm\,s^{-1}}$.

Unfortunately, this technique has also some disadvantages. First, from the RV curves it is possible to derive only the minimum mass of the planet ($\mathrm{M_p} \sin i$) since the inclination angle between the orbital plane of the substellar companion and the observer cannot be directly measured. However, when transiting observations of the planet are also available, the inclination angle of the orbit can be derived, and hence the orbital parameters can be fully resolved. Secondly, the RV curve requires several decades of continues observations to cover at least one orbital period for planets orbiting beyond a few AU's from the host star (like the giant planets in our solar system). Considering also that the RV amplitude decreases with the distance of the host star (see equation 1.6), the RV technique is most sensitive for planets orbiting within a few AU's. Finally, since precise RV measurements require thousands of narrow absorption lines in the stellar spectrum, the detection of exoplanets by this technique is mainly restricted to solar-type stars, having low rotational velocities[5].

1.1.6.1 Intrinsic Stellar Phenomena

Since the RV technique is based on the precise determination of the centroid of the spectral lines, other stellar phenomena producing a similar effect might mimic the doppler shift induce by an orbiting planets. The main sources of stellar phenomena affecting the RV measurements are:

- **Stellar oscillation modes.** As in the case of the Sun, most stars show a rich spectrum of stable radial and non-radial oscillation modes. In the case of solar-type stars, they present solar-like oscillations, having the maximum power at frequencies of ~ 3 mHz, corresponding to ~ 5 minutes. The effect of these oscillation modes has been usually average out (for solar-type stars) by taking longer exposure time ($\mathrm{t}_{exp} \gtrsim 10$ minutes) This method is very efficient at decreasing the RV variations induced by stellar oscillations well below the $1\ \mathrm{m\,s^{-1}}$ level (see O'Toole et al. 2008). Unfortunately this is

[5]The stellar rotation produces a significant broadening in the spectral lines, thus difficulting the precise RV measurements.

not possible for stars having much longer oscillation timescales (such as giant stars). In addition, since non-radial pulsations are expected to be accompanied by line shape variations, it is possible to use a bisector analysis in order to investigate the degree of asymmetry and to determine whether these variations are in phase with the RV curve (see section 4.3.2.1).

- **Rotational modulation**. When a spot (or group of spots) crosses the stellar disk of a rotating star, produces variations in the spectral lines profile, as shown in Figure 1.8. When the spot is passing in the front of the region that is approaching the observer (left spot in Figure 1.8), it blocks some of the blue shifted emission, producing an asymmetry in the spectral lines (the line centroid is red-shifted). A similar effect is caused by the spot after it moved toward the red shifted side of the disk (the line centroid is blue-shifted). Since the asymmetry induced by the rotating spot produces also a displacement of the spectral lines centroids, this effect might be interpreted as a radial velocity shift. In fact, when the spot remains stable during several rotational periods, the RV curve of the star will show a similar variation as the one produced by a substellar companion (e.g. Queloz et al. 2001). In order to discriminate between the companion interpretation and the rotating spot, a line bisector and/or photometric analysis is needed (the spots produce line asymmetries and photometric variability). In addition, since this effect is wavelength dependent, the RV curve computed at different wavelength might provide additional information (e.g. a flat curve in the near-IR; see Huelamo et al. 2008).

- **Magnetic activity** Another source of RV variations might be produced by inhomogeneities in the stellar convection, which are associated to magnetic activity in the stellar surface (e.g. Saar et al. 1998; Lovis et al. 2011). When convection is partially supressed or retarded in a region of the stellar surface, then a net RV velocity is measured when integrating the light from the stellar disk. One way to distinguish between the intrinsic and extrinsic scenarios is to study the emission of chromospheric lines (such as the Ca II HK lines). The emission of these lines is directly correlated

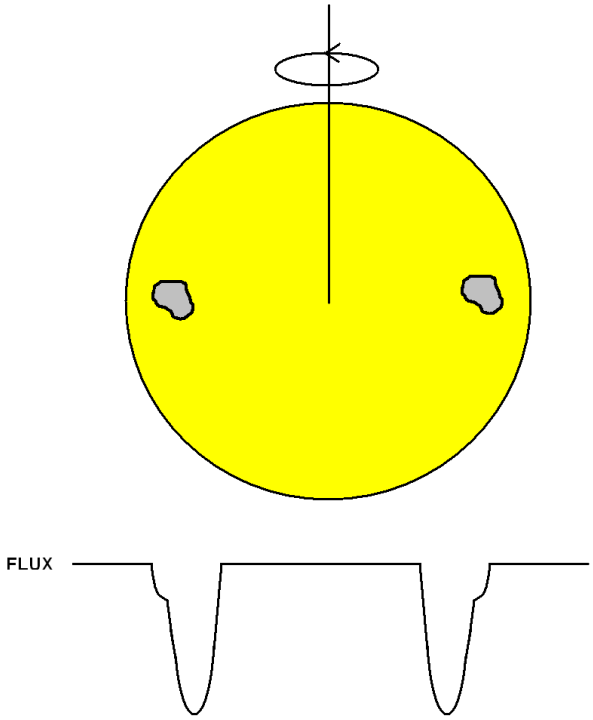

Figure 1.8: Schematic diagram of the effect of starspots in the shape of spectral lines. Since the spot is moving from the left (blue shifted emission) to the right (red shifted emission), the extra absorption in the stellar lines is also moving from the blue to the red, shifting the line centroids.

to the presence of bright plagues and dark spots in the stellar surface (e.g. Dorren & Guinan 1994). This emission is also observed to be stronger around active regions in the surface of the Sun.

1.2 The Observed Properties of Exoplanets

Since more than 800 exoplanets have been detected, it is possible to study in a statistical manner their properties and how they correlate with the stellar properties. These kind of analysis can provide valuable information about the planet formation/migration mechanisms, dynamical interactions and orbital evolution of planetary systems.

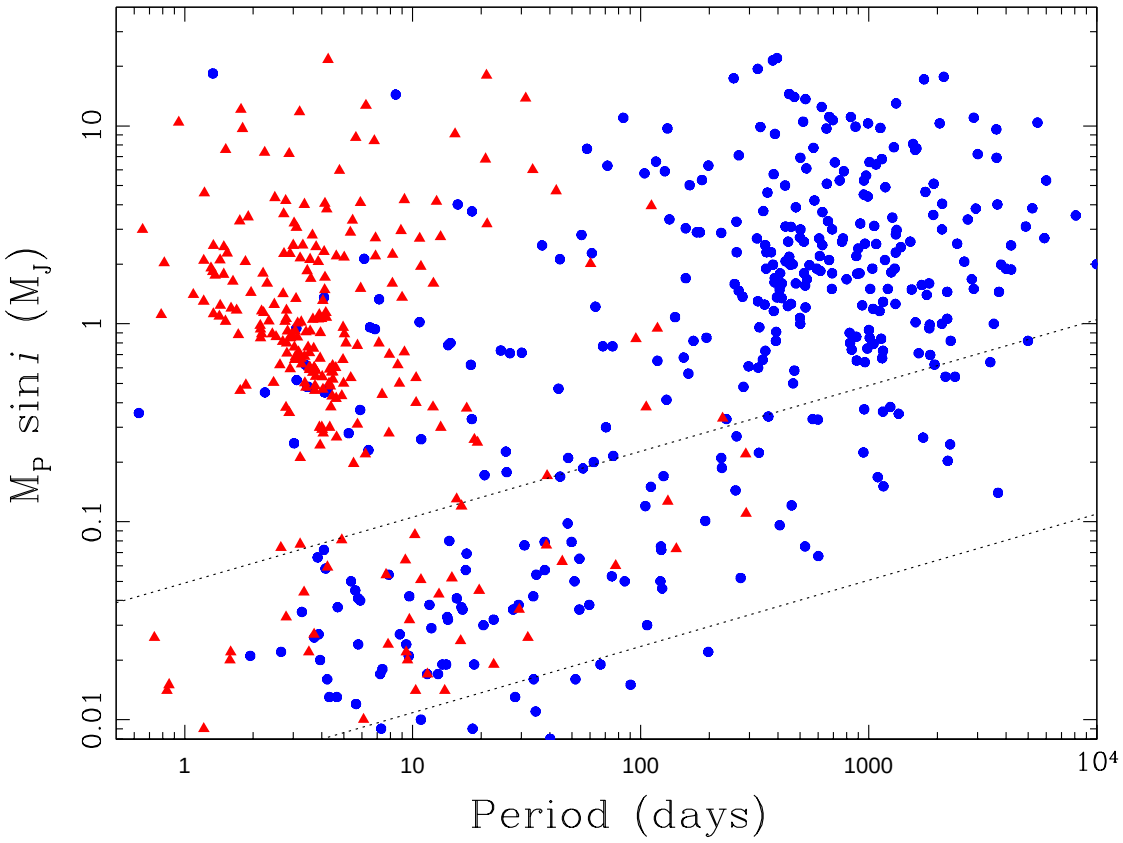

Figure 1.9: Planetary mass ditribution as a function of the orbital period, for planets detected by the RV technique (blue dots) and the planet transit method (red triangles). The two lines from bottom to top, correspond to RV amplitudes of 1 $\mathrm{m\,s^{-1}}$ and 10 $\mathrm{m\,s^{-1}}$, respectively.

Figure 1.9 shows the position of exoplanets in the Mp - P plane [6]. The blue dots correspond to the exoplanets detected by the RV method while the red triangles are those detected by transit surveys. The two dotted lines correspond to radial velocity amplitudes of K=1 $\mathrm{m\,s^{-1}}$ (lower line) and K=10 $\mathrm{m\,s^{-1}}$ (upper line) for a 1.0 $\mathrm{M_\odot}$ star. Some interesting features are worth highlighting from Figure 1.9. First, there is a large population of *Hot Jupiters* ($\mathrm{M_p}$ $\gtrsim$ 0.3 $\mathrm{M_J}$; P $\lesssim$ 10 days), most of them detected by the transit method. In fact, around $\sim$ 35 % of the known exoplanets have orbital periods below 10 days. This is in part due to the strong decrease in the transit probability with the orbital distance ($p \propto a^{-1}$), restricting this

[6]The orbital parameters of the exoplanets were retrieved from http://exoplanet.eu/

technique mainly to P $\lesssim$ 10-20 days. In the core-accretion model, this rich population of gas giants orbiting in close-in orbits can be explained by including a migration mechanism, where the giant planets are formed beyond the snow line [7] and then they move inward due to the interaction with the disk (e.g. Ida & Lin 2004). Also it can be noticed that there is a paucity of giant planets orbiting between $\sim$ 10 - 100 days, which is known as the "period valley". However, when we only include giant planets detected by the RV method (in order to avoid the strong bias toward close-in systems in the transit method), this apparent "desert" is less pronounced than what was previously claimed, based on smaller samples (Jones et al. 2003; Udry et al. 2003; Cumming et al. 2008). It is also evident that there is an overpopulation of planets having orbital periods around $\sim$ 400 days. This feature cannot be attributed to an observational bias, since the RV detectability increases toward shorter period orbits. Finally, there is a paucity of very short period (P $\lesssim$ 3 days) giant planets with $M_P \lesssim 0.6\ M_J$. Once again, this cannot be explained by an observational bias, since these systems should be easily detected by both, the RV technique and the transit method. This observational result might be interpreted to be due to the total evaporation of relatively small giant planets by the strong stellar radiation field or that the outer part of the planet is evaporated, thus losing a significant fraction of its gaseous envelope. This scenario would also explain the presence of low mass planets ($M_P \lesssim 0.03\ M_J$) with orbital peridos $\lesssim$ 3 days, which would be the remaining solid cores of gas giants after losing their envelopes. In fact, according to the core-accretion model, the size of these solid cores that form giant planets (after accreting gas from the protoplanetary disk) is $\sim 0.01 - 0.03\ M_J$ (Ida & Lin 2004).

In Figure 1.10 the eccentricities of exoplanets as a function of their orbital distance are plotted, for planets detected by the RV technique[8]. For comparison, the position of the inner planets in the Solar System are labelled (red triangles). The first thing to notice in Figure 1.10 is the existence of highly eccentric planets, in contrast to what is observed in the

[7] The snow line is the point beyond which condensation of ices occurs, thus increasing considerably the surface density of the disk ($\sim$ 3 AU in the Solar System).

[8] The planet's eccentricity cannot be directly measured by the tranist method.

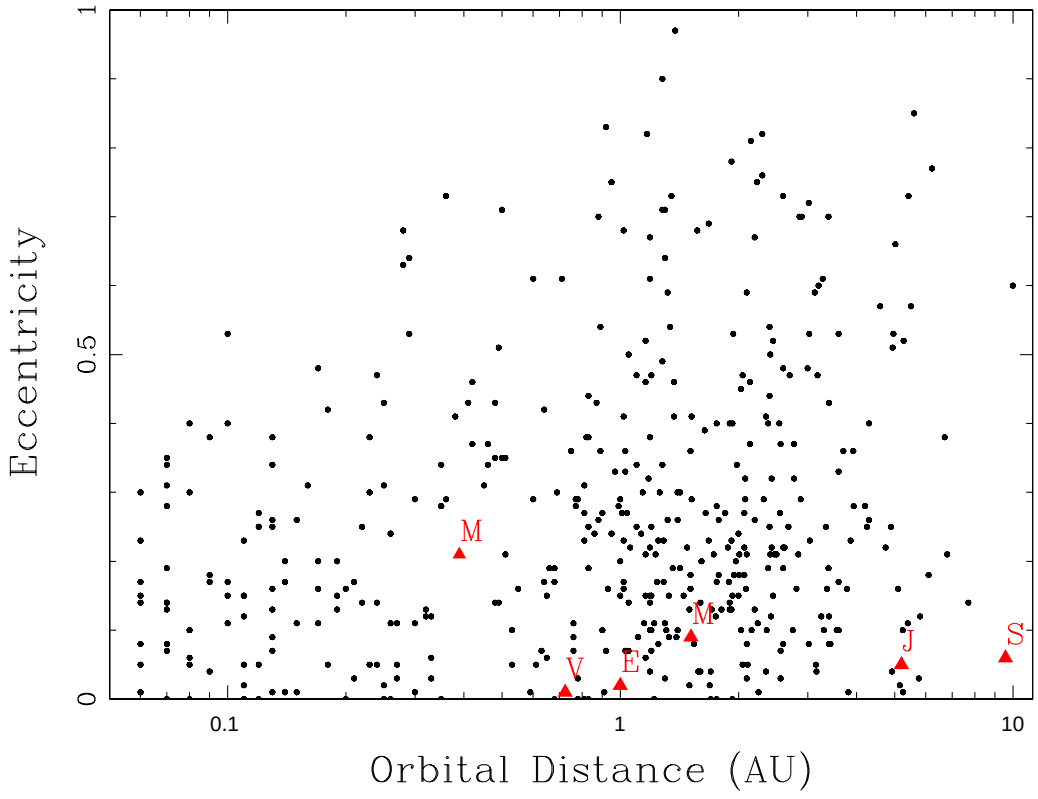

Figure 1.10: Eccentricity distribution as a function of the planet's orbital distance (black dots). The position of the inner planets in the Solar Systems are also shown (red triangles).

Solar System. It has been argued that the reason causing the high eccentricity observed in extrasolar planets is due to to planet-planet (e.g. Lin & Ida, 1997) and planet-planetesimals interactions (Levison et al. 1998) or as the result of the gravitational influence of a stellar companion (e.g. Holman et al. 1997) or a passing star (e.g. Zakamska & Tremaine, 2004). Also, it can be noticed that close-in planets ($a \lesssim 0.2$ AU) have lower eccentricities ($e < 0.3$ - 0.4). This has been interpreted as the result of tidal circularisation (Goldreich & Soter 1966). However, it is also possible that the afore mentioned mechanisms (planet-planet and planet-star interactions) are less efficient in pumping the eccentricities in the inner region of planetary systems, which might explain the low values of e observed among close-in planets.

Finally, Figure 1.11 shows a histogram of the metallicity of known exoplanets host stars.

The distribution has a sharp peak at [Fe/H] $\sim$ 0.1 dex, suggesting that planets are formed preferentially around metal-rich stars. In addition, it has been found that the occurrence of gas giants increases with increasing metallicity of the host star (Gonzalez 1997; Fischer & Valenti, 2005) and that the mean metallicity of planet hosting stars is significantly higher than non-planet hosting stars (Santos et al. 2001). These observational facts has been used in favor of the core acrretion model, where the content of metals in the protoplanetary disk is a crucial ingredient for the formation of the cores and planetesimal, prior to the formation of planets.

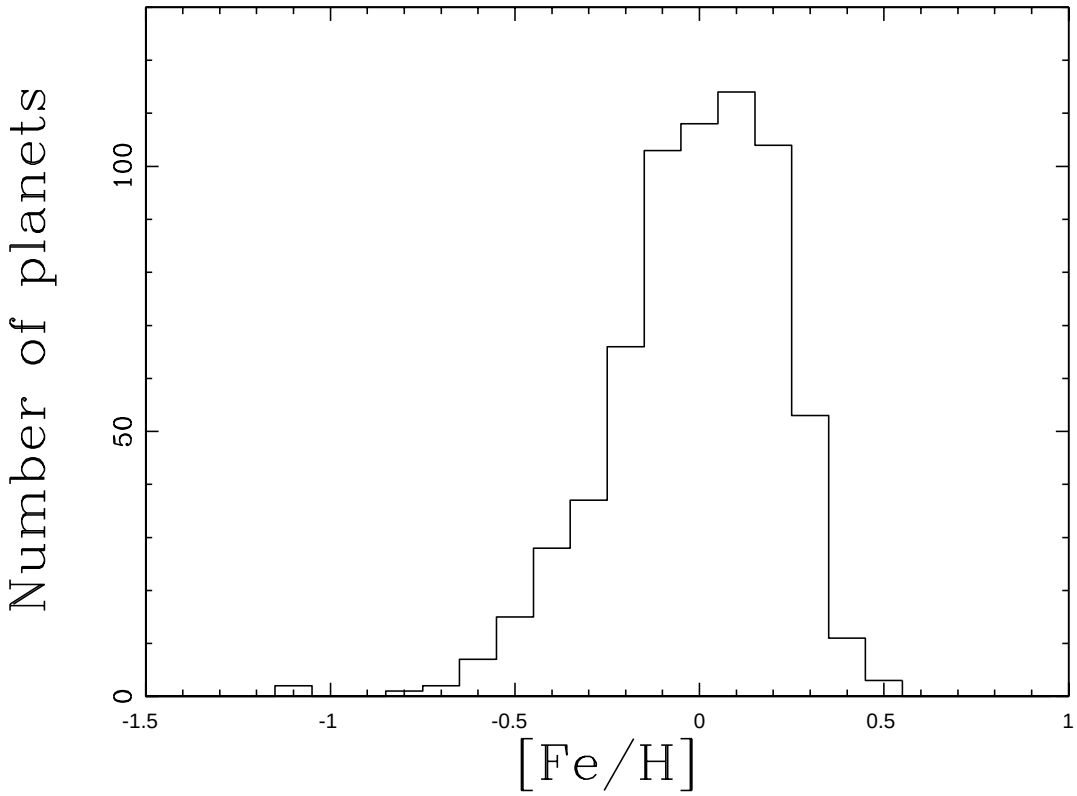

Figure 1.11: Histogram of the metallicity of stars hosting exoplanets.

1.3 Giant Stars

1.3.1 Naming convention

During the rest of this thesis the following naming convention is used:

- **Evolved or post-MS star.** Stellar object that has exhausted the hydrogen in its core, thus H fusion is not taking place in the core. This category includes SGB, RGB, HB and AGB stars.
- **Sub-giant star (SGB).** Stellar object that is fusing hydrogen in a thick shell around an inert core.
- **Giant star.** Evolutionary states after the sub-giant phase. This category includes RGB, HB, and AGB stars.
- **Red Giant Branch star (RGB).** Star that is fusing hydrogen in a thin shell around an inert core.
- **Horizontal Branch star (HB).** Stellar object after the end of the RGB phase. It is either a core helium burning star or an early phase double shell burning object (asymptotic giant star).

1.3.2 Stellar evolution after the main-sequence.

During the main sequence, a star converts hydrogen into helium in its core, in stable conditions. During this process, the stellar core increases slowly its mean molecular weight, leading to a gradual contraction and hence a slight increase in the gas pressure and temperature. The increase in the core temperature (T_C) leads to a slight increase in the core size, where particles in the outer edge of the core also reach temperatures high enough to fuse H into He. In addition, when the star has a convective core ($M\star \gtrsim 1.2\ M_\odot$) then H-rich material from the outer layers will be transported into the core, replenishing it with extra nuclear fuel. This process also increases the energy generation in the star's center which is

transported into the stellar surface, increasing its luminosity and radius. Figure 1.12 shows the evolution of a 1.0 $M_{\odot}$ star (and solar metallicity) in the HR diagram (upper panel), from the zero age main sequence (ZAMS) up to the tip of the red giant branch (RGB) phase. In the lower panel it is shown the fractional mass of the inner (blue dashed line) and outer (red solid line) edge of the H-burning region. It can be noticed that during the MS the nuclear reactions occur in the stellar core, which reaches a maximum size (in mass coordinate) of 0.4 $M_{\odot}$. After the exhaustion of H in the star's center, the nuclear fusion starts to occur in a shell around the nearly isothermal He-enriched core. The thickness the shell rapidly shrinks (the blue line approaches the red line during the sub-giant phase) becoming narrower during the RGB phase. A similar plot is shown in Figure 1.13 but for a 3.0 $M_{\odot}$ and solar metallicity.

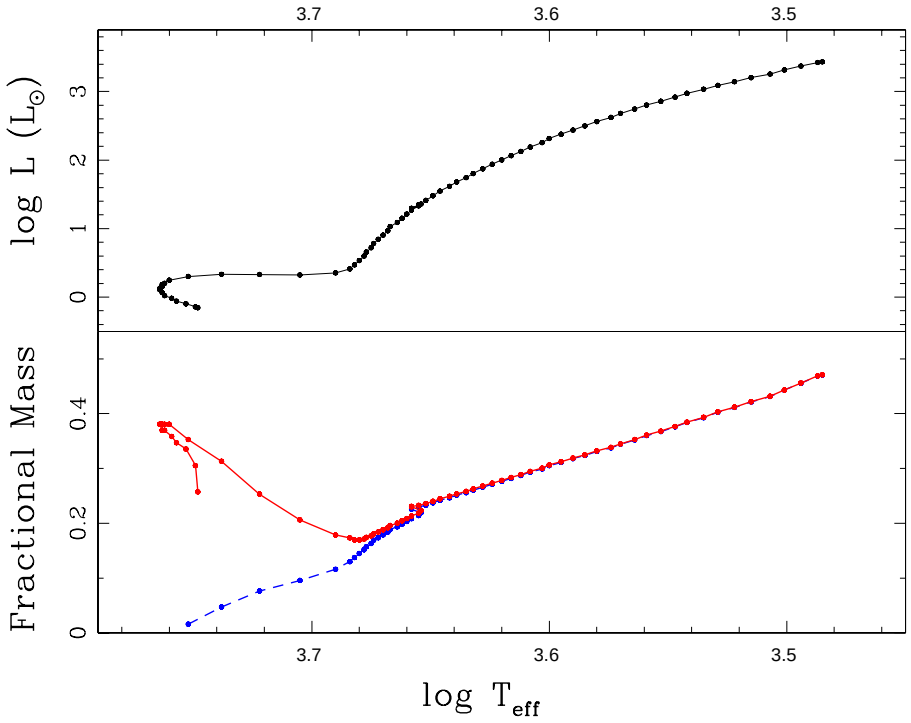

Figure 1.12: Upper panel: Evolutionary track for $M_{\star}$ = 1.0 $M_{\odot}$ and Z=0.019 (solar metallicity). Lower panel: The corresponding fractional mass of the inner (dashed blue line) and outer (solid red line) H-burning region. Data from Salasnich et al. (2000).

The subsequent evolution after the star reaches the tip of the RGB depends on the stel-

lar mass, although the physical processes are similar. For star with $M_\star \lesssim 2.0\ M_\odot$, since the gas in its core is in degenerate conditions, an increase in the temperature does not lead to an expansion of the gas (because the gravitational force is balance by degenerate pressure instead of thermal pressure). Because of this, the rich-He core increases its temperature while its size and pressure remain nearly constant. At some point, the local temperature reaches a value high enough ($\sim 10^8$ K) so that He fusion sets in, thereby releasing suddenly a huge amount of energy, known as *Helium Flash* (see e.g. Dearborn et al. 2006; Mocak et al. 2008). Most of the energy produced during this process is used in breaking the core degeneracy and to heat it up, hence this effect is not expected to be observed in the stellar surface. As a consequence of the *Helium Flash* all of the structure of the star is modified, decreasing its radius (since the energy production by Hydrogen fusion at the edge of the core falls; see e.g. Dearborn et al. 2006) and increasing its surface temperature. The star has now reached a new stable equilibrium, fusing He in the core. This stage in the stellar evolution is the beginning of the Horizontal Branch (HB) phase. On the other hand, for a star more massive than $\gtrsim 2.0\ M_\odot$, an increase in its central temperature is accompanied with a a slight expansion of the gas, cooling down the stellar core. This is because these stars reach high temperatures at lower densities, therefore the gas in the core is not degenerate (see Figure 1.14). In Figure 1.14 the core temperature as a function of the central density from the ZAMS to the tip of the RGB is plotted. Four stellar models from Charbonnel et al. (1993) are presented ($M_\star$ = 1.0, 1,5, 2.0, 3.0 $M_\odot$; black, green, red and blue lines, respectively). The dots correspond to each point in the grid of stellar models. It can be seen that higher mass star reach the He ignition temperature at lower central densities, while lower mass stars develop degenerate cores ($\rho \sim$ 10^5-10^6 gr cm^{-3}) at T $\sim$ 10^7-10^8 K. At some point, the mass of the inert core reaches a critical value, hence thermal pressure can no longer compensate the gravitational force, leading to a further contraction. The value of T_C increases dramatically until He fusion takes place. As a consequence, energy released by He fusion expands the stellar core, and the star's radius and luminosity strongly decrease. As for the lower mass range, at this point the star reaches a new equilibrium, burning steadily He in its core.

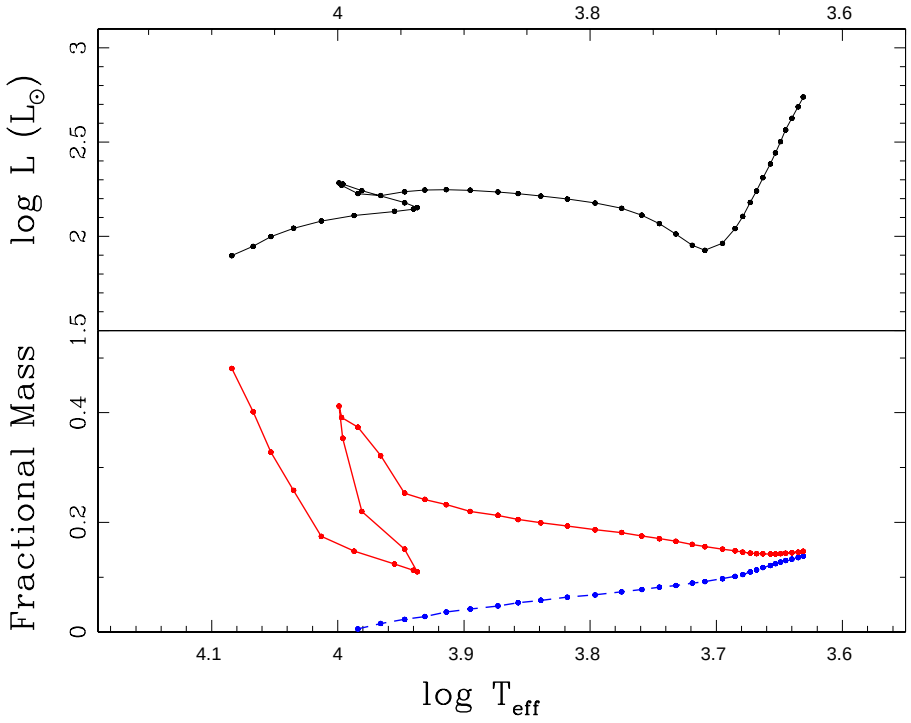

Figure 1.13: Same as Figure 1.12 but for $M_\star = 3.0\ M_\odot$.

During this stage of the stellar evolution, the star is converting He into heavier elements in the core (mainly carbon and oxygen) via the triple-α process. Additionally the star is also fusing hydrogen into helium in a thin layer surrounding the stellar core. Even though the star is in a stable situation, the fuel supply is exhausted in a much shorter timescale than the main-sequence timescale (core hydrogen fusion), leaving behind an inert C-O core, while still burning hydrogen in a thin shell. Once again, the core contracts, increasing its temperature, until He fusion is possible around the core. At this point the star is burning He in the layer inmediately above the inert C-O core and in a shell above that one, fusing hydrogen. The star has now reached the so called asymptotic giant branch (AGB) phase, and its evolution is even faster than during the HB phase. During this evolutionary stage, the star losses a large fraction of its envelope via strong stellar winds, and its late fate will depend on its initial mass. In Table 1.1 the timescales for the MS, sub-giant branch (SGB), RGB, HB and AGB phases, for $M_\star = 1.5\ M_\odot$ and $3.0\ M_\odot$ are listed. For comparison the positions of the starting

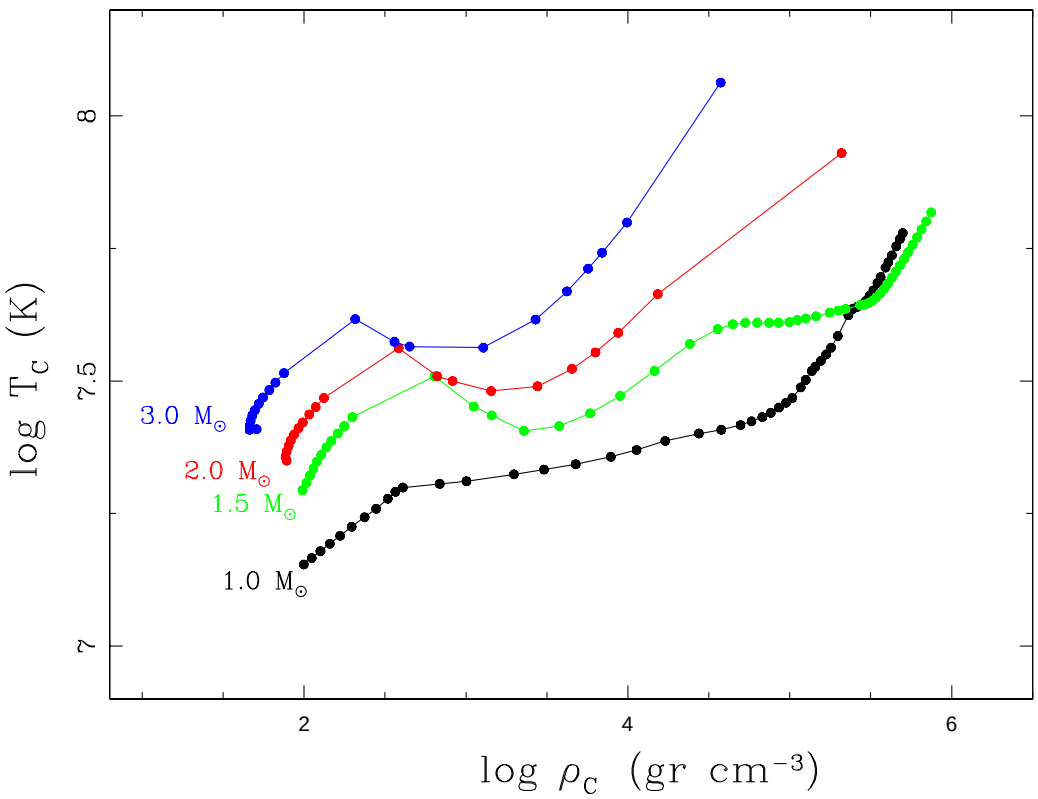

Figure 1.14: Central Temperature as a function of the the density in the stellar core. Four different models are presented ($M_\star$ = 1.0, 1,5, 2.0, 3.0 $M_\odot$; black, green, red and blue lines, respectively). Data from Charbonnel et al. (1993)

points of different evolutionary states are shown in Figure 1.15.

Besides the fact that massive stars live shorter than lower mass stars, it is important to notice from Table 1.1 that there are large differences in the timescales for different evolutionary states, after the main-sequence. For instance, the evolution of the star through the subgiant phase is very fast, compared to the MS and HB phases (also to the RGB for a 1.5 $M_\odot$ star). As a consequence, the subgiant stars are rare, simply because a star spends just a small fraction of its life in this stage. It can be also noticed that the HB timescale is comparable to the time in the RGB, for a 1.5 $M_\odot$ star, and much longer for a 3.0 $M_\odot$ star. For this reason, most of the stars that lie in the red clump [9] (see Chapter 2 for further

[9]The red clump is the region in the HR diagram restricted to 0.8 $\lesssim$ B-V $\lesssim$ 1.2 and -0.5 $\lesssim$ M_V $\lesssim$ 2.0

Table 1.1: Timescales for different evolutionary states, for a 1.5 $M_\odot$ star and 3.0 $M_\odot$ star. The corresponding locations in the HR diagram are plotted in Figure 1.15. Data from Salasnich et al. (2000).

Points in Figure 1.15	τ (Myr)	Stage
	$M_\star = 1.5\ M_\odot$	
1 - 2	2755	Core H-burning (main-sequence)
2 - 3	42	H fusion in a thick shell (sub-giant phase)
3 - 4	151	H fusion in a thin shell (RGB)
4 - 5	...	Post He-flash transition
5 - 6	112	Core He-burning (HB)
6 - 7	12	Double shell (He and H) burning (AGB)
	$M_\star = 3.0\ M_\odot$	
1 - 2	379	Core H-burning (main-sequence)
2 - 3	2.0	H fusion in a thick shell (sub-giant phase)
3 - 4	2.3	H fusion in a thin shell (RGB)
4 - 5	7.3	Transition from RGB to HB
5 - 6	85	Core He-burning (HB)
6 - 7	6.5	Double shell (He and H) burning (AGB)

details) are HB stars, instead of first ascending RGB stars. Finally, it is clear that the stellar evolution speeds up after the exhaustion of helium in the core, thus the AGB phase is also very short. Once again, the observational consequence, is a that only a small percentage of the field stars are in the AGB phase. Figure 1.16 shows the color-magnitude diagram of the globular cluster M3. The different post-MS evolutionary phases can be clearly distinguished, since the cluster members have roughly the same age and metallicity.

1.3.3 Surface abundances

Due to the stellar evolution, the surface abundances of stars are strongly affected. After the MS, the stars develop deep convective envelopes, where material from the surface and from

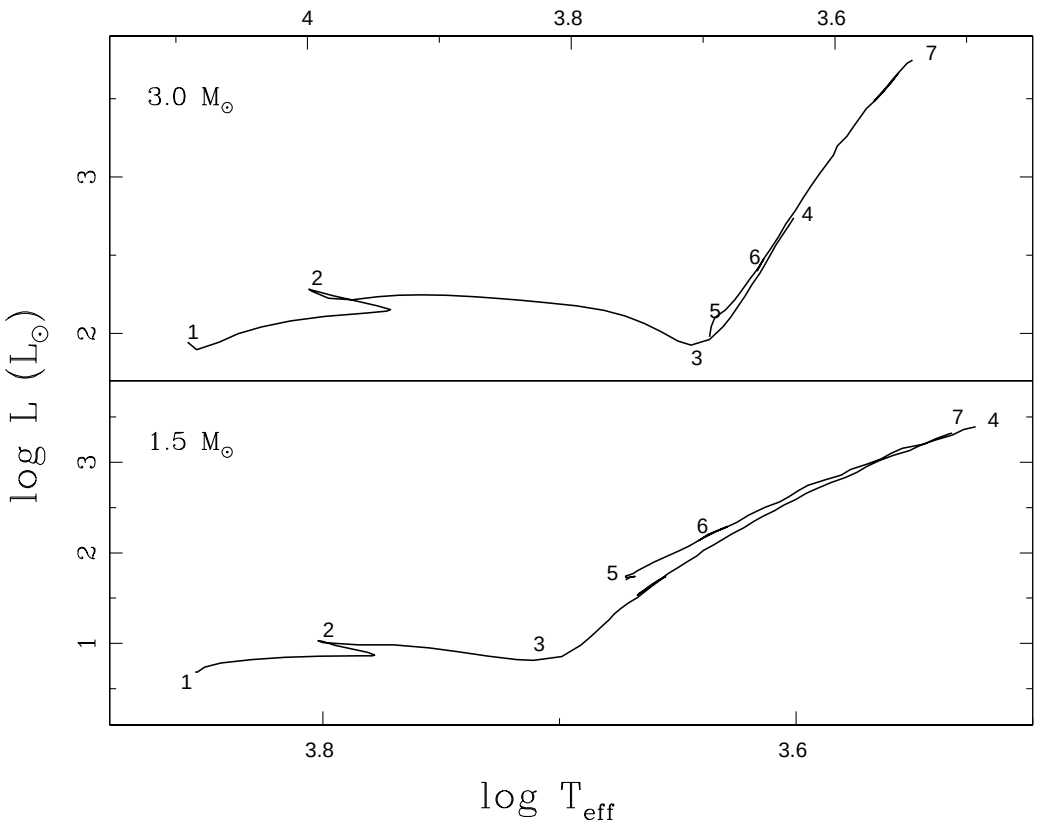

Figure 1.15: Stellar evolutionary tracks for a 3.0 $M_\odot$ star (upper panel) and a 1.5 $M_\odot$ star (lower panel), both having solar metallicity. Different evolutionary stages are labelled which are explained in table 1.1. Data from Salasnich et al. (2000).

the interior are mixed together. During the post-MS evolution, there are three main mixing episodes, known as *dredge-up*. The first dredge-up occurs when the star reaches the base of the RGB. During this period, the convective zone reaches the inner part of the star, bringing to the surface material produced by fusion processes. As a result, the atmospheric abundances of nuclear processed elements, such as ^{3}He and ^{4}He, are enhanced and the isotopic ratios of some elements such as ^{12}C/^{13}C decrease. In addition, the surface lithium is depleted since it is completely destroyed in the stellar interior at temperatures greater than $\sim 2.7 \times 10^6$ K. A second dredge-up occur for stars with $\sim$ 4-7 $M_\odot$, at the end of the HB phase (i.e., soon after the exhaustion of He in the core). In this mixing episode the surface abundance of ^{4}He and ^{14}N increases, while the amount of ^{12}C, ^{13}C and ^{16}O decreases. Finally, a third dredge-up is predicted to occur during the AGB phase. As a result recently synthesized carbon is carried

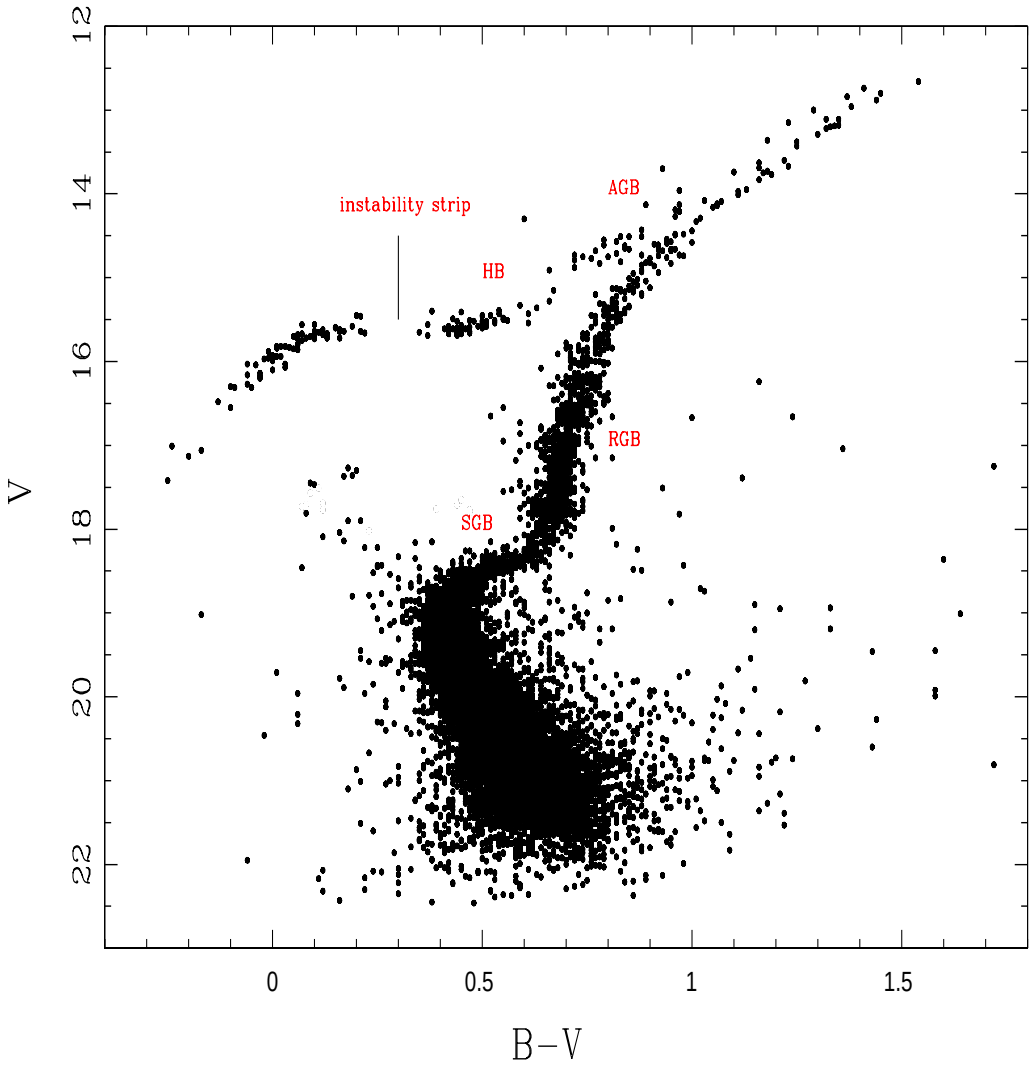

Figure 1.16: HR diagram of the globular cluster M3. Different post-MS evolutionary states are labelled. Data taken from Buonanno et al. (1994).

to the surface. In Figure 1.17 the surface abundance relative to the original composition after the first dredge-up is shown, for star with mass up to 5 $M_{\odot}$. The abundances of five species are plotted. Their corresponding symbols are also labelled. It is worth to notice that the mixing process is nearly constant with the stellar mass, except for ^{14}N (since it is produced in intermediate-mass stars via the CNO cycle). The observed abundances and isotopic ratios in giant stars provide an excellent test for stellar evolution models, aswell as a determination

of the age of the star based on the amount of enhancement or depletion of different species.

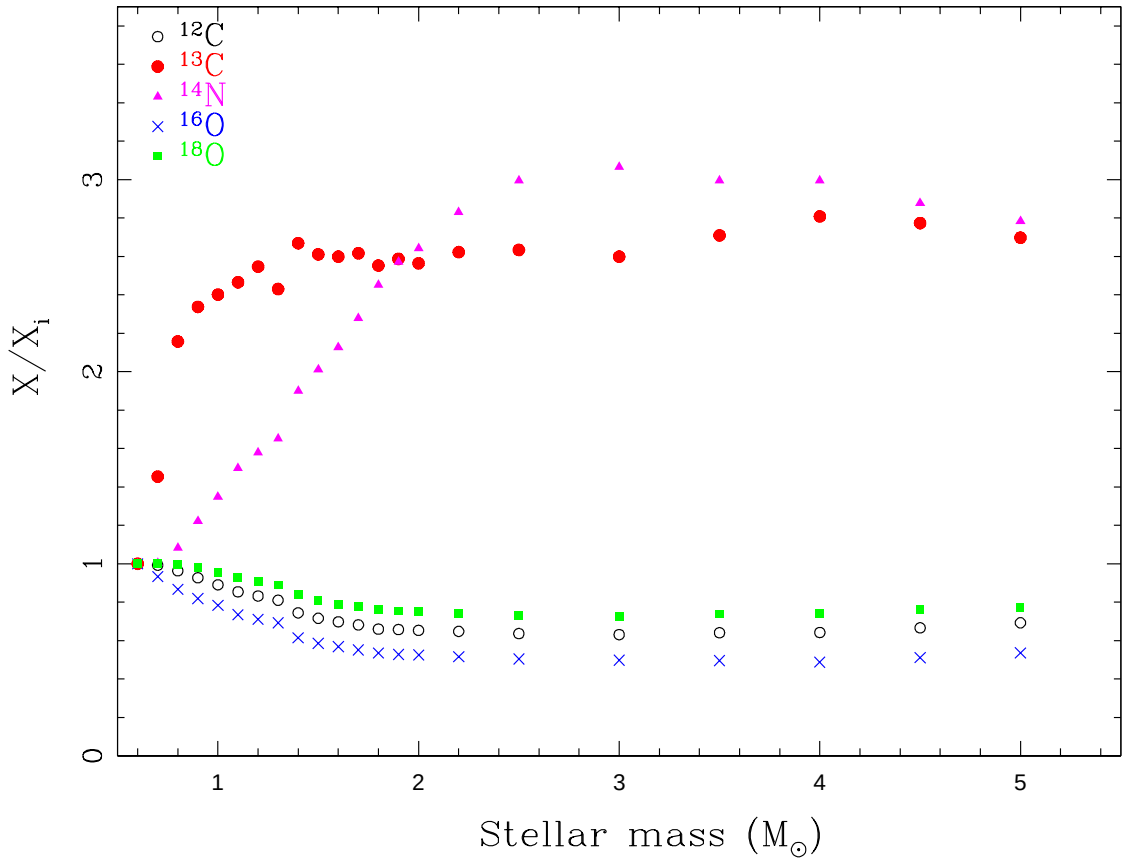

Figure 1.17: Surface abundances relative to the original composition for different elements, after completition of the first dredge-up. Data from Salasnich et al. (2000)

1.4 Planets Around Giant Stars

As already mentioned in the previous section, the RV detection of planets is mainly biased to solar-like stars, having a low rotational velocity and low level of stellar activity. Fast rotators present a broad lines spectrum, preventing us to compute precise RV's, and active stars induce a high level of RV noise, which might also mimic the doppler shift induced by a planet. On one hand, very low mass stars are too cool and present strong molecular bands in their spectra, which makes difficult the precise determination of the doppler shift induced

by a companion. On the other hand, main-sequence (MS) stars more massive than ~ 1.3 $M_{\odot}$ (corresponding to spectral types earlier than $\sim$ F5) are too hot and rotate fast, which produces a spectrum dominated by few and broad absorption lines, making extremely challenging the computation of precise RV's. However, when these kind of stars evolve off the MS, they become cooler and rotate slower than their MS progenitors (Schrijver & Pols 1993), thus presenting a rich spectrum of narrow absorption lines, which, as discussed before, is ideal for the computation of precise RV's. Figure 1.18 shows a portion of the observed spectra of a

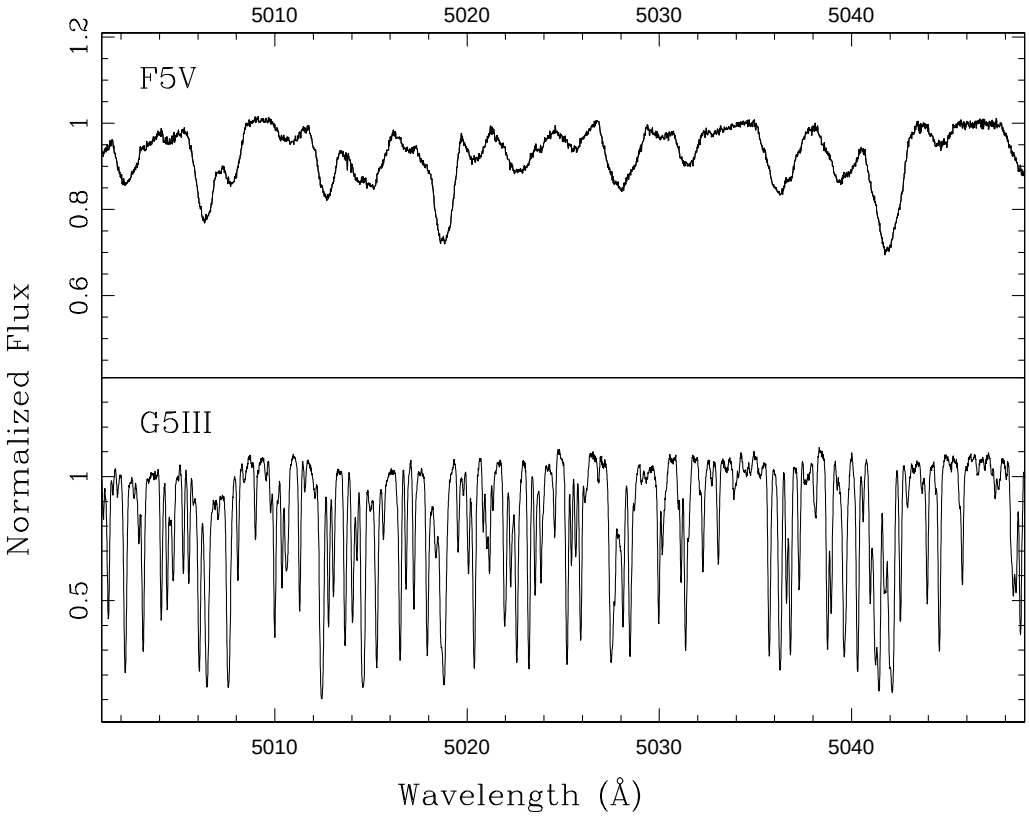

Figure 1.18: A portion of the optical spectrum of a F5 main-sequence star (upper panel) and a K1 giant star. Both stars have similar masses.

F5 main-sequence star (upper panel) and a K1 giant star. Both stars have a similar mass. It can be clearly noticed that in the former case the spectrum is dominated by few and broad lines, whereas in the latter case the spectrum exhibits many narrow absorption lines, which means that in principle it is possible to reach high RV precision and hence to detect substellar

companions. However, giant stars are known to be intrinsically more active than solar-type stars (see § 5.1 in chapter 3), difficulting the RV analysis. The first precise RV studies of giant stars (e.g. Smith et al. 1987; Belmonte et al. 1990) revealed that these objects present different oscillations modes having amplitudes up to hundreds $\mathrm{m\,s^{-1}}$ and timescales from hours to days. As a comparison, the typical oscillation amplitudes in the sun are $\sim 20\ \mathrm{c\,m\,s^{-1}}$ with timescales of ~ 5 minutes. Subsequent studies (e.g. Merline 1999; Frandsen et al. 2002; Kallinger 2008), also showed that these kind of stars present solar-like oscillations, i.e., oscillations excited by convection, with a frequency spectrum similar to the one observed in the sun.

Kjeldsen & Bedding (1995), using a linear theory and based on observational data, provided a set of scaling relationships that are usefull for deriving the typical amplitude and frequency of the radial velocity variations, which are given by:

$$v_{osc} = 0.23\,\frac{(L/L_{\odot})}{(M/M_{\odot})}\,\mathrm{ms^{-1}} \tag{1.9}$$

$$\nu_{max} = 3.05\,\frac{(M/M_{\odot})}{(R/R_{\odot})^2\sqrt{(T_{\mathrm{eff}}/5777\,K)}}\,\mathrm{mHz} \tag{1.10}$$

where v_{osc} is the maximum velocity amplitude observed at the frequency ν_{max}. Also, the expected change in the stellar luminosity can be computed by:

$$(\delta\,L/L)_{\lambda} = 20.1\,\frac{v_{osc}\,/\,\mathrm{m\,s^{-1}}}{(\lambda/550\,\mathrm{nm})\,(T_{\mathrm{eff}}/5777\,\mathrm{K})^2}\,\mathrm{ppm} \tag{1.11}$$

where λ is the wavelength and ppm denotes parts per million (1 ppm $\sim 1\ \mu\,$mag). Even though these relations were computed for MS and sub-giant stars, they agree reasonably well with the oscillation amplitudes and timescales observed in giant stars. Additionally, Cox (1980) derived the following relation:

$$\Delta\,\nu = 134.9 \left(\frac{M}{M_{\odot}}\right)^{1/2} \left(\frac{R}{R_{\odot}}\right)^{-3/2} \mu Hz \tag{1.12}$$

where $\Delta\,\nu$ is the so-called *large frequency separation*, corresponding to the frequency separation of two consecutive peaks for which the radial mode[10] differs by $n = 1$. It can be seen that if ν_{max} and $\Delta\,\nu$ are known, equations 1.10 and 1.12 can be used to derive the physical properties of the star (e.g. Kallinger et al. 2009). Also, equations 1.9 and 1.11 can used to derive the RV amplitudes and timescales of the main oscillation modes in the giant stars. For instance, let's consider a clump giant star having the following physical parameters: $\mathrm{M} = 2\,\mathrm{M}_{\odot}$, $\mathrm{L} = 50\,\mathrm{L}_{\odot}$, $\mathrm{R} = 10\,\mathrm{R}_{\odot}$ and $\mathrm{T_{eff}} = 5000\,\mathrm{K}$. Using these values in equations 1.9 and 1.10 we obtain a radial velocity amplitude of $\sim$ 6 $\mathrm{m\,s^{-1}}$ at a frequency of $\sim$ 66 μHz, corresponding to a timescale of 4.2 hours.

Extensive recent studies have also shown that the random sampling of the stellar pulsations result in a RV noise at the 10 - 100 $\mathrm{m\,s^{-1}}$ level (e.g. Setiawan et al. 2004). In particular, Sato et al. (2005) showed that giant stars bluer than B - V = 1.0 present a variability at the 10 $\mathrm{m\,s^{-1}}$ level (with the most stable stars showing a 6-8 $\mathrm{m\,s^{-1}}$ scatter) and Hekker et al. (2006) also showed that a significant fraction the bluer giant stars (B - V color < 1.2) present a RV noise below 20 $\mathrm{m\,s^{-1}}$. From these results, it is possible to conclude two main things. Firstly, even though giant stars are intrinsically more active than solar-type stars, it is possible to use the RV technique to detect substellar companion in the blue part of the red giant branch and the horizontal branch. For instance, let's consider a Jupiter-mass planet in a circular orbit at a distance of 0.6 AU around a 2.0 $\mathrm{M}_{\odot}$ star. According to equation 1.6, (assuming $\sin i$ close to 1) the RV amplitude induced by the planet is $\sim$ 26 $\mathrm{m\,s^{-1}}$, which is $\sim$ 3 times the stellar jitter for the bluer giant stars ($\sim$ 6-10 $\mathrm{m\,s^{-1}}$). Secondly, since the oscillation main modes have timescales of hours to days, it is not possible to average them by, for instance, increasing the observing time (as is usually done for solar-type star), meaning that the RV errors are

[10]The n mode correspond to the radial modes in spherical coordinates. Since the pulsation of the stars correspond to the eigenmodes of a vibrating sphere, also non-radial modes having different polar and azimuthal orders are observed.

dominated by stellar jitter when using a high precision spectrograph, such as HARPS.

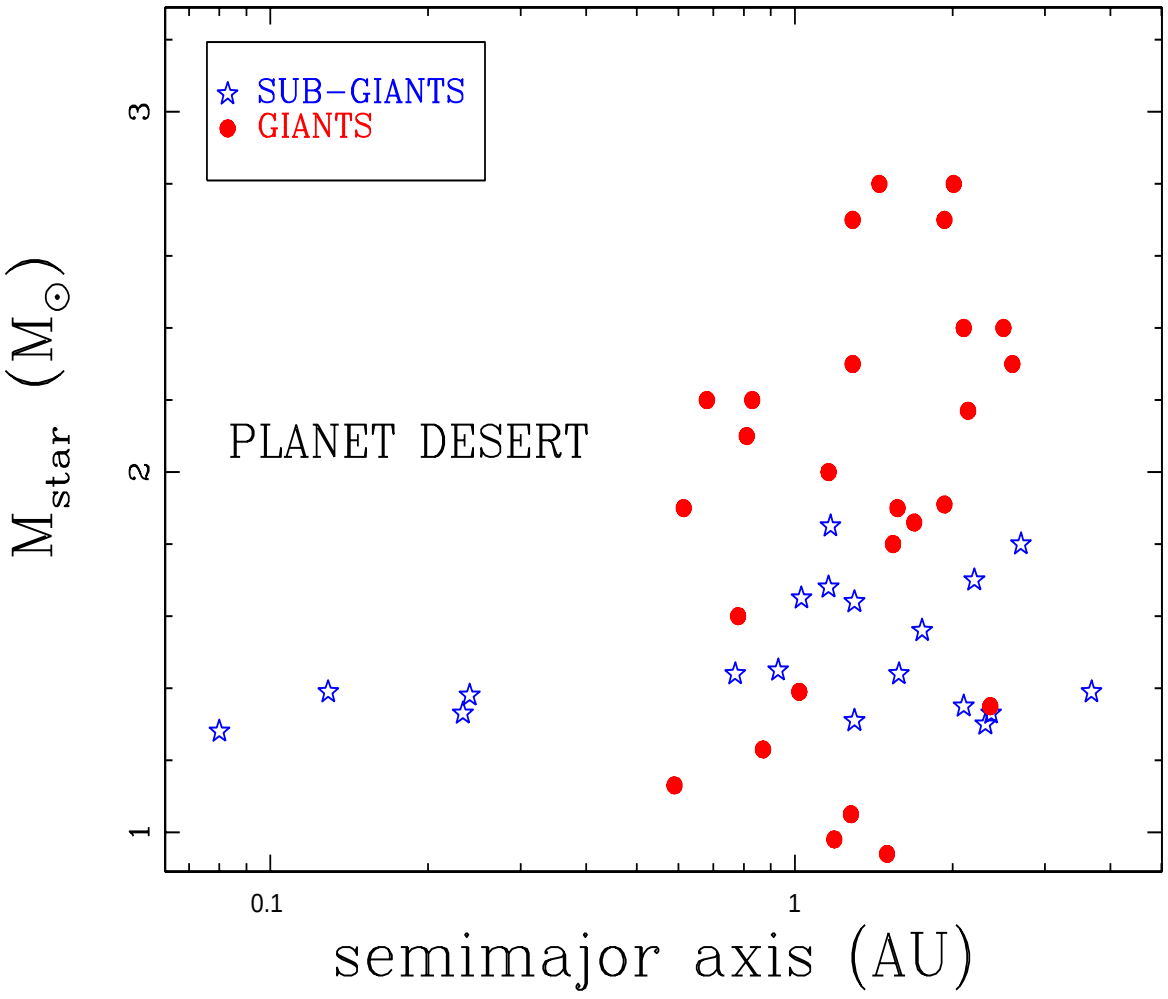

Figure 1.19: Semimajor-axis distribution for planets around evolved stars, discovered until 2009. The blue open stars and red filled circles correspond to sub-giant and giant host stars, respectively.

By the middle of 2009, (starting time of this PhD thesis) around 40 planets were already found orbiting evolved stars, revealing different properties than the planetary population around solar-type stars. In Figure 1.19 the semimajor-axis distribution of planets orbiting post-MS stars (discovered until 2009) as a function of the host stellar mass is plotted. It can be noticed that there is an absence of planets around giant stars within 0.6 AU, which suggests that the stellar evolution of the host stars is playing a role on the orbital evolution

of the planets around them. Theoretically, this observational fact was predicted to be due to tidal interactions that lead to the engulfment of close-in planets during the ascent of the host star through the red giant branch (e.g. Siess & Livio 1999; Sato et al. 2008; Villaver & Livio 2009). Also, in the presence of a significant mass loss, the gravitational field produced by the host star is weakened, thus increasing the orbital distance of the planet. Hence the orbital evolution of the planet can be described by:

$$\frac{\dot{a}}{a} = -\frac{\dot{M}_\star}{M_\star} - F_t \tag{1.13}$$

where a is the orbital distance of the planet (assumed to be in a circular orbit), $M_\star$ is the mass of the star, hence $-\dot{M}_\star$ corresponds to the mass loss rate. F_t is the tidal friction contribution, given by (see Villaver & Livio 2009, and references therein):

$$F_t = q\,(1+q)\,\frac{f}{\tau_d}\,\frac{M_{env}}{M_\star}\,\left(\frac{R_\star}{a}\right)^8 \tag{1.14}$$

where q is the ratio between the mass of the planet and the mass of the star and M_{env} is the mass of the convective envelope of the giant star. $M_\star$ and $R_\star$ are the total mass and radius of the star and f is a numerical constant obtained by integrating the viscous dissipation of the tidal energy through the convective zone. Finally, τ_d is the eddy turnover timescale, which is given by (Rasio et al. 1996):

$$\tau_d = \left(\frac{M_{env}\,R_{env}\,\Delta R}{3\,L_\star}\right)^{1/3} \tag{1.15}$$

where R_{env} is the radius of convective envelope and ΔR corresponds to the size of the convective region ($R_\star$ - R_{env}). Also, according to Reimers' Law, during the red giant branch phase the stellar wind is not strong enough to significantly affect the stellar mass, thus the orbital evolution is mainly dictated by the angular momentum exchange between the planet

and the convective envelope of the giant host star [11]. Since the tidal dissipation term is strongly dependent on the relative size of the stellar radius and the orbital distance (see equation 1.14), close-in planets are expected to be engulfed mainly during the late phase of the RGB evolution of the parent star, when the radius of the star becomes larger. Furthermore, since during the RGB phase the radius of the star strongly depends on its mass (the lower the mass, the larger the radius), the survival distance (minimum orbital distance to avoid being engulfed by the host star) of planets decreases dramatically with the mass of the host star. For instance, according to Kunitomo et al (2011), the survival distance for a planet around a 1.8 $M_\odot$ star is 1.1 AU, while for a 2.0 $M_\odot$ star is only 0.36 AU. This fact is certainly very important when studying the effect of planets engulfment in the observed population of them around horizontal branch stars.

In addition, from Figure 1.19 it can be noticed that there is no close-in planet orbiting subgiant stars more massive than $\sim 1.4\,M_\odot$. Since subgiants have not evolved enough (small radii) to efficiently exchange angular momentum with the orbiting planets, the tidal decay scenario cannot be solely responsible for the lack of close-in planets around them. In fact, this result suggests that the properties of planetary systems are stongly affected by the mass of the host star and the protoplanetary disk from where they are formed. In particular, the formation scenarios and/or migration mechanisms, including the protoplanetary disk dissipation timescale, are probably significantly different for intermediate-mass stars ($M \gtrsim 1.5$ $M_\odot$) when compared to lower mass stars. In fact, in the core-accretion model the formation of gas giant planets in close-in orbits ($\lesssim 0.6$ AU) around stars more massive than $\sim 1.2 M\odot$ is less efficient compared to lower mass stars (Burkert & Ida 2007).

[11] An enhanced mass loss rate will produced a decrease in the stellar mass and then a lower surface gravity. The star will then reach a larger radius at the end of the RGB phase, hence a stronger tidal force. See e.g. Schroder & Smith (2008)

1.5 This Thesis

In this PhD thesis it will studied the population of planets in close-in orbits ($a \lesssim 0.6$ AU) around giant stars. The main goals of this project are:

- To measure the fraction of giant stars that host a giant planet ($M \gtrsim 1$ M_J) in close-in orbits ($a \lesssim 0.6$ AU). This information will be used to either confirm or discard the lack of short period planets around giant stars that has been claimed by different groups, as discussed in the previous section. In particular, it is expectec to determine whether an observational bias, as the sampling rate, might be in part responsible for this result.

- To compare the fraction of close-in planets around RGB and HB stars, in order to determine whether there is an evolutionary effect that is significantly affecting their orbits.

- To increase the poor statistics of planets around intermediate-mass stars, in order to investigate how the mass of the host star affects the properties of planetary systems.

In order to achieve these goals, a radial velocity survey has been conducted during the last three years, aimed at detecting giant planets around giant stars. A sample of 166 post-MS stars have been monitored using three different high-resolution spectrographs, namely, FECH and CHIRON (1.5m telescope at CTIO) and FEROS (2.2m telescope at La Silla), leading to a large set of precise radial velocities, having a nearly homogeneous sampling.

The organization of this thesis is as follows. In chapter 2 is described the sample selection along with the determination of the atmospheric and physical parameters of the giant stars. In particular, the evolutionary status for all of the targets is derived, relying on the post-MS timescales provided by the stellar evolution models. In chapter 3, an extensive description of the I_2 cell technique is presented and a detailed analysis of all of the radial velocities computed from the CTIO sample, compounded by 66 clump stars. In chapter 4, the preliminary results from the FEROS sample are presented, highlighted by the discovery

of several binary systems and the detection of four new planets orbiting three different stars. Finally, the summary and conclusions of this thesis are discussed in chapter 5.

Chapter 2

Sample Definition and Physical Properties

*(Jones, M. I.; Jenkins, J. S.; Rojo, P. and Melo, C. H. F. 2011, A&A, 536, 71 *)*

2.1 Introduction

The determination of fundamental parameters (mass, radius, temperature, age, etc) of stars hosting exoplanets is very important, since it allows us to study how the physical properties of the host stars and the orbital parameters of the planets are related, when compared with non-planet host stars. This information can be used to test different planet formation models and to study the dynamical evolution of planetary systems. For instance, the study of the chemical abundances of stars harbouring planets led to the discovery of the planet-metallicity correlation for main-sequence stars (Gonzalez 1997; Santos et al. 2001; Fischer & Valenti 2005), which has been used as an argument in favor of the core-accretion model (Ida & Lin 2004; Alibert et al. 2005; Kennedy & Kenyon 2008).

During the main-sequence and the subgiant phase, the physical parameters of stars can be derived accurately from photometric data, since different evolutionary tracks are well separated in the color magnitude diagram for a given metallicity. However, during the red giant phase, red giant branch (RGB) and horizontal branch (HB) stars with different ages, masses

*We added two new targets to the original sample of 164 stars presented in this paper.

and metallicities occupy a similar position in the HR diagram, making the determination of their physical parameters more difficult. In order to partially break this degeneracy, high-resolution spectra can be used to derive effective temperature ($T_{\rm eff}$), surface gravity ($\log g$), and iron abundance ([Fe/H]).

We are conducting a precision radial velocity survey of 166 bright G and K giant stars in the southern hemisphere. The main goal of this project is to determine the fraction of close-in planets (orbital periods $\lesssim$150 days) orbiting RGB and HB stars, and compare them in order to study how the evolution of the host star affects the inner part of planetary systems. Furthermore, these results will be used to test the theoretical prediction that tidal interaction leads to the engulfment of close-in planets during the post-MS evolution of the host star (Villaver & Livio 2009; Nordhaus et al. 2010; Kunitomo et al. 2011). A more detailed description of the project, along with the first results will be presented in a forthcoming paper (Jones et al. 2012, in prep.).

In this work we present the spectroscopic atmospheric parameters ($T_{\rm eff}$, $\log g$, microturbulent velocity and [Fe/H]), which are used to derive the mass, radius and evolutionary phase of the program stars. In addition, rotational velocities are measured for our targets, so can select against rapid rotators that would preclude the measurement of precise radial velocities.

This chapter is organized as follows. In sections 2 and 3 we describe the targets selection, the observations and data reduction. In section 4 we present the method used to derive the atmospheric parameters. In section 5, stellar evolution models are used to derive the mass, radii and evolutionary status of the stars in our sample. In section 6 we study the dependence of macroturbulence broadening with $\log g$, which is used to derive projected rotational velocities. Finally, the summary and the discussion is presented in section 7.

2.2 Targets

We selected a total of 166 giant stars in the Southern Hemisphere from the *Hipparcos* catalog (Perryman el al. 1997) according to their position in the HR diagram ($0.8 \leq \mathrm{B\,V} \leq 1.2$; $-0.5 \leq \mathrm{M}_V \leq 4.0$). We included stars brighter than $\mathrm{V} = 8$ magnitudes, parallaxes with a precision better than 14%, and uncertainty in the Johnson B-V color less than 0.02 mags. We also removed binary systems from the sample and we add the restriction of including only those stars with a *Hipparcos* (H_p) photometric variability less than 0.015 mags. The *Hipparcos* ID, B-V color and V magnitudes are listed in the first three columns of Table 2.2 (placed at the end of this chapter). The improved *Hipparcos* parallaxes (Van Leeuwen 2007) are listed in column 4, and the uncertainties are given within brackets. We corrected the visual magnitudes using the 3D extinction maps of Arenou et al. (1992) in order to compute absolute magnitudes and luminosities (see § 5). The visual extinction values (A_V) are listed in column 5 of Table 2.2.

Figure 2.1 shows the position of our targets in the HR diagram and their resultant evolutionary status (see § 5). Evolutionary tracks from Salasnich et al. (2000) are overplotted for different stellar masses and metallicities. In summary, our sample consists of 122 RGB stars and 42 HB stars, with a range of masses between $\sim$1.0 $\mathrm{M}_\odot$ and 3.5 $\mathrm{M}_\odot$.

2.3 Observations and Data Reduction.

High resolution and high S/N spectra were taken for each of the stars in our sample. The targets were observed using the Fiber-fed Extended Range Optical Spectrograph (FEROS; Kaufer et al. 1999) mounted on the MPG/ESO 2.2 m telescope at La Silla and the Echelle Spectrograph mounted on the 1.5 m telescope at CTIO, which has now been replaced by CHIRON (Schwab et al. 2010). FEROS has a resolving power of R $\sim$ 48000, an efficiency of $\sim$ 20 % and provides an almost complete optical spectral coverage ($\sim$ 3500 - 9200Å), which allows us to study many absorption lines in the optical range (used in the chemical analisys

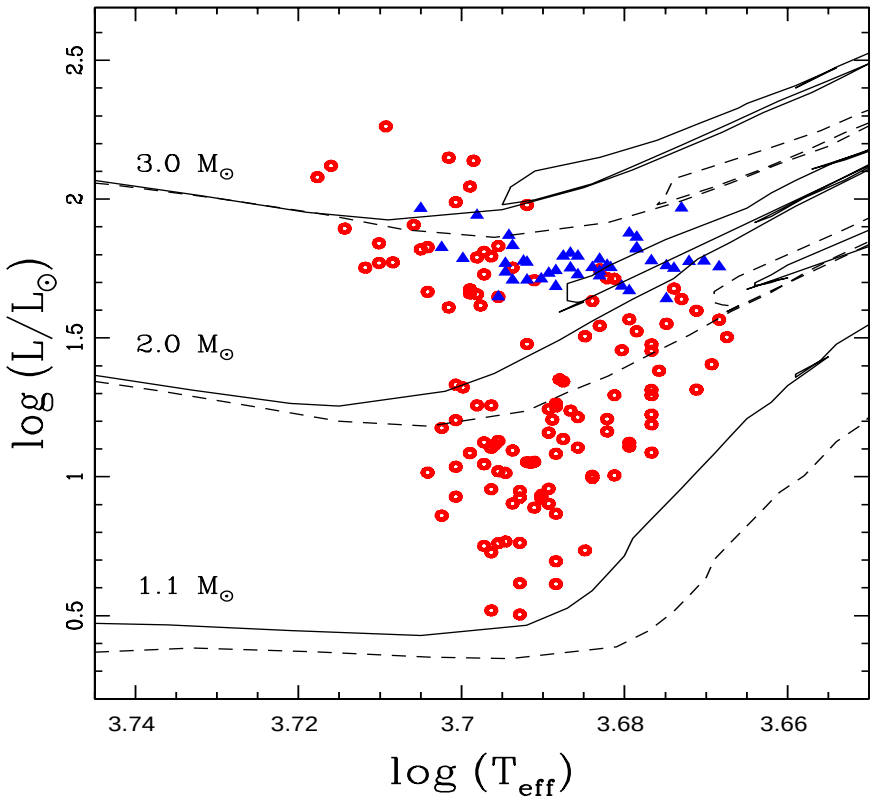

Figure 2.1: HR diagram including all of our targets. The red open circles correspond to RGB stars, while the blue filled triangles to HB stars. Different evolutionary tracks (Salasnich et al. 2000) are overplotted for stars with 1.1 $M_{\odot}$, 2.0 $M_{\odot}$ and 3.0 $M_{\odot}$ (line pairs from bottom to top). The solid lines correspond to models with [Fe/H]=0.0 and the dashed lines to [Fe/H]=0.32

and in our radial velocity computations) and also to study the emission in the core of the Ca II HK lines (3933 and 3968 Å), which are used as chromospheric activity indicators (e.g. Jenkins et al. 2008 and references therein). The echelle spectrograph mounted on the 1.5 m telescope, can reach a maximum resolution of R $\sim$ 45000 with an efficiency of $\sim$ 1% and covers a spectral region between 4020 Å and 7100 Å. The exposure time of the FEROS targets (V $\leq$ 8) ranges between 60 and 480 seconds, which leads to a S/N ratio between 200-300 at 5500 Å and $\sim$ 80 at 3950 Å. The CTIO targets (V $\leq$ 6) were observed with exposure times between 180 and 300 seconds, giving rise to S/N ratios of $\sim$ 200 at 5500 Å.

The FEROS spectra were reduced in a standard fashion using the FEROS Data Reduc-

tion Software. All the calibrations (flat-fields, bias and lamps) were obtained during the afternoon, according to the standard ESO calibration plan. The reduction of CTIO spectra was performed in a similar way, using an IDL-based pipeline available for all users. As in the case of FEROS data, the calibrations were taken during the afternoon, before the nightly stellar observations.

2.4 Atmospheric Parameters

We derived spectroscopic atmospheric parameters (T_{eff}, log$g$, [Fe/H] and microturbulent velocity) using the equivalent widths (EWs) of a set of neutral and singly-ionized iron lines. We used the 2002 version of the MOOG[1] code (Sneden 1973), which solves the radiative transfer equation through a multi-layer atmospheric model by imposing excitation and ionization equilibrium (Saha-Boltzmann equation; see Appendix A) and using the atomic parameters for each electronic transition (excitation potential (χ), oscillator strength (loggf) and damping constant; see § 4.1). The atmosphere models were obtained from the Kurucz (1993) grid. We linearly interpolated this grid in metallicity (fixing T_{eff} and log g), then in T_{eff} (fixing the metallicity and log g) and finally in log g to obtain the desired atmosphere model. For a detailed description of this method see Gray (2005).

2.4.1 Line List and Atomic Constants

We adopted the line list used in Sestito et al. (2006), which consists of a total of 159 Fe I lines and 18 Fe II lines, covering the spectral range between 5500Å and 6800Å. Features bluer than 5500Å were excluded in order to discard strongly blended lines and to avoid complications in the continuum tracing. Lines redder than 6800 Å were excluded due to the presence of many telluric features in the red part of the optical spectrum. The loggf and χ for each transition were also taken from Sestito et al. (2006; see also references therein). The collisional damping constants were computed using the Unsöld (1955) approximation, multiplied by an enhacement factor E given by: log$E = a\,\chi$ - b, where $a = 0.381 \pm 0.017$ and

[1] http://www.as.utexas.edu/ chris/moog.html

b =0.88 ± 0.33. χ corresponds to the excitation potential of the transition. This factor was derived from several Fe I features with available accurate collisional damping parameters, for stars with $T_{eff} \sim$ 5000 K (Gratton et al. 2003). Finally, we removed from the line list seven Fe I lines ($\lambda\lambda$ 5521.28, 5547.00, 5852.23, 6290.55, 6400.32, 6411.11, 6625.04 Å) and four Fe II lines ($\lambda\lambda$ 5136.80, 5525.14, 5534.85, 6383.72 Å) which were found to be the most deviant points in the abundance analysis. We examined all of these lines by eye, and we found that all of them are heavily blended leading to an inaccurate measurement of the EW, with the exception of the feature at 5852.23 Å , where the discrepant behavior is probably due to an error in its atomic parameters (loggf and/or χ).

2.4.2 Equivalent Widths

Since it is very time consuming to measure EWs manually, we used the code ARES[2] (Sousa et al. 2007), which computes them automatically, by applying a gaussian fit to the spectral lines. In order to test the realibility of this code we also computed some EWs manually, using the routine splot in IRAF[3]. We found differences $< 10\%$ between our EW measurements and those derived using ARES, which are mainly due to the continuum fit. In the abundance analysis we included only those lines with EW between 10 mÅ and 150 mÅ . Lines weaker than 10 mÅ were discarded because the measured equivalent width is strongly dependent on the continuum fitting. Also, lines stronger than 150 mÅ were removed from the analysis, since the gaussian fitting profile is not always appropiate to determine the EW and also because these lines are more affected by collisional broadening.

2.4.3 Results and Uncertainties

The effective temperatures, spectroscopic surface gravities, microturbulent velocities and iron abundances for our targets are presented in columns 6 - 9 of Table 2.2. We compared our resulting effective temperatures with those derived by three other independent studies that have

[2]http://www.astro.up.pt/ sousasag/ares/

[3]IRAF is distributed by by the National Optical Astronomy Observatories, which are operated by the Association of Universities for Research in Astronomy, Inc., under cooperative agreement with the National Science Foundation.

a few stars in common with our sample. These are shown in Figure 2.2 where we found mean differences of $\langle \Delta T_{eff}(\text{This study - McWilliam 1990}) \rangle = 156 \pm 86\,K$ for 14 stars in common, $\langle \Delta T_{eff}(\text{This study - Randich et al. 1999}) \rangle = 108 \pm 70\,K$ for 6 stars in common and $\langle \Delta T_{eff}(\text{This study - Luck \& Heiter 2007} \rangle = 24 \pm 50\,K$ for 12 stars in common. Considering all of the stars

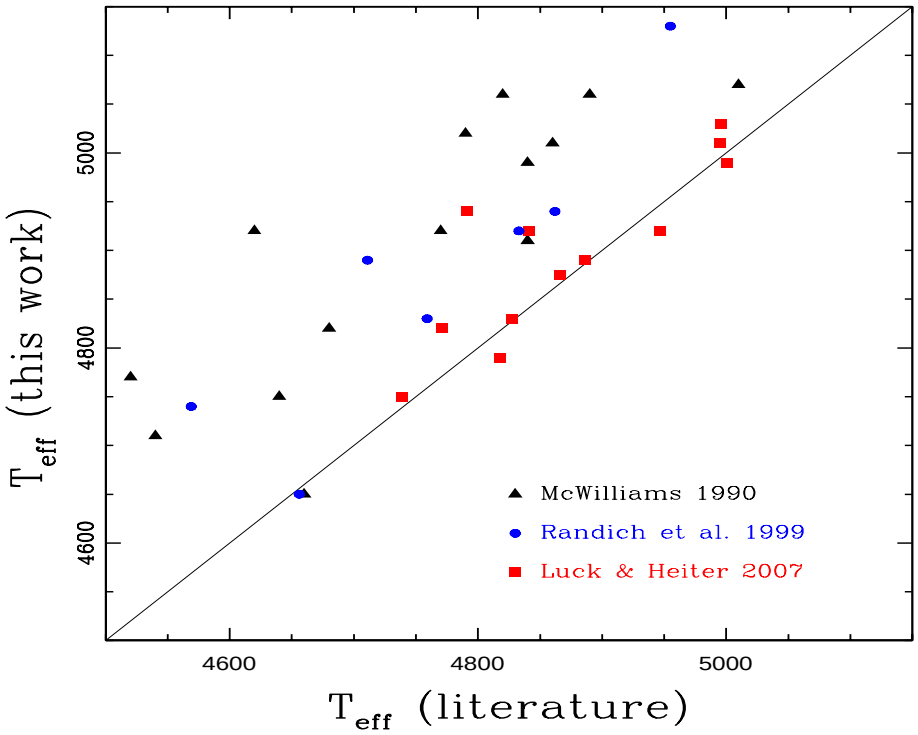

Figure 2.2: Comparison between our derived effective temperatures with those derived by three independent works. The filled black triangles, filled red squares and filled blue circles correspond to T_{eff}'s derived by McWilliam (1990), Luck & Heiter (2007) and Randich et al. (1999), respectively. The solid line is the 1:1 correlation.

in common with these three studies we obtain $\langle \Delta T_{eff}(\text{This study - literature}) \rangle = 98 \pm 90\,K$. Based on this result, we adopted an uncertainty of $\sim 100\,K$ in our derived T_{eff}'s, which is consistent with the estimated uncertainties in similar studies (see e.g. Sestito et al. 2006, Hekker & Melendez 2007, Ghezzi et al. 2010).

Figure 2.3 shows a histogram of the metallicity distribution of our targets. It can be seen that most of the giant stars in our sample are metal rich, with $\sim 50\%$ having [Fe/H] between 0.0 and 0.2 dex. Also, there is no significant difference in the metallicity distribution between

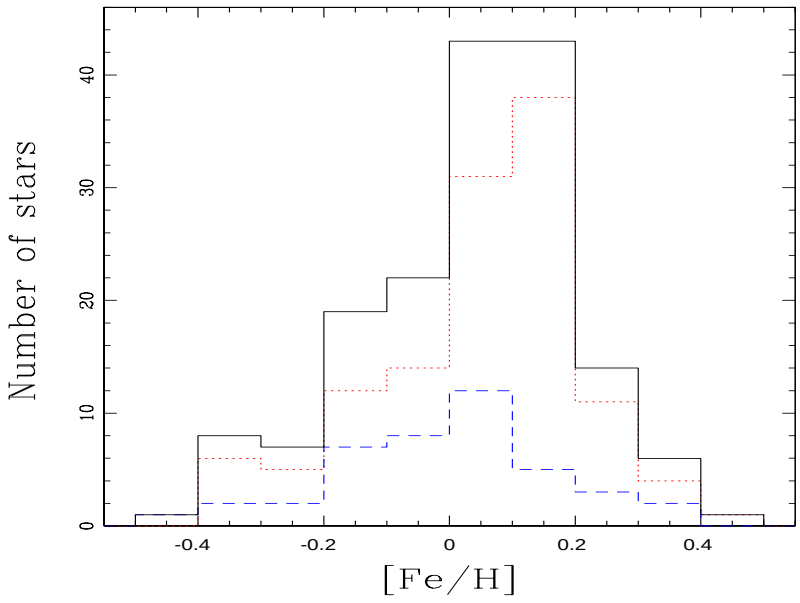

Figure 2.3: Metallicity distribution of our targets. The red dotted line corresponds to RGB stars, while the blue dashed line to HB stars. The sum of both samples is shown with the solid black line.

RGB and HB stars. The uncertainties in the metallicities were estimated from the standard deviation of individual Fe I lines in the abundance analysis, and are listed in brackets in column 9 of Table 2.2. These values are larger than the uncertainties in the mean, but are more realistic.

Concerning the surface gravities, several studies have revealed systematic differences between spectroscopic and photometric $\log g$'s. In the former approach, the surface gravity is varied in order to obtain the same abundance for Fe I and Fe II lines, while in the latter case the gravity of the star is derived by comparing its position in the HR diagram with theoretical evolutionary tracks. In Figure 2.4 we plot the difference between photometric (see § 5) and spectroscopic $\log g$'s, as a function of the effective temperature (left panel) and the mass (right panel) for our program stars. It is evident that our derived spectroscopic $\log g$'s are systematically lower (by $\sim$0.14 dex) than photometric gravities for RGB stars cooler than $\sim$5000 K (or less massive than $\sim$ 2.0 $M_{\odot}$). A similar discrepancy between photometric and spectroscopic $\log g$'s was also found by Gratton et al. (1996) and Sestito et al. (2006).

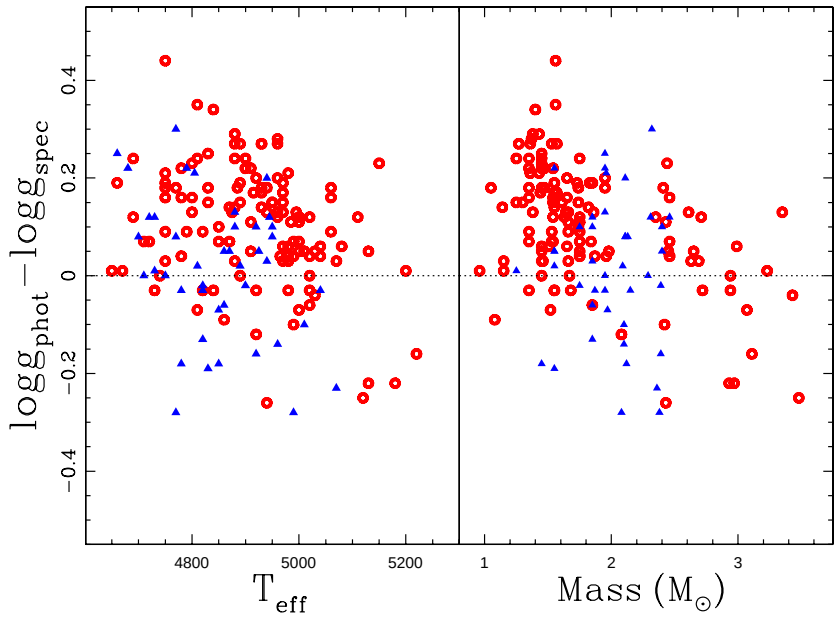

Figure 2.4: Difference between photometric and spectroscopic $\log g$'s as a function of the effective temperature (left panel) and the mass (right panel) of our targets. The open red circles and filled blue triangles represent RGB and HB stars, respectively. The black dotted line shows the $\Delta \log g = 0.0$ boundary.

However, some authors have found the oppsosite result, i.e., that the spectroscopic $\log g$'s are systematically higher than the photometric ones (e.g. Valenti & Fischer 2005, da Silva et al. 2006). This suggests that these inconsistencies in the derived surface gravities are due to systematic errors inherent to the method used for deriving iron abundances, mainly from Fe II lines, which strongly affect the final $\log g$'s (Fe I lines are quite insentive to a change in $\log g$). For instance, an overestimation/underestimation of the position of the continuum, will translate into higher/lower measured EWs, which are matched by a higher/lower metallicity in the curve of growth. Since the Fe II lines are on average weaker than Fe I lines, they will be more affected, hence deriving lower/higher $\log g$'s. However, we cannot discard a priori other effects like departures from LTE that might be playing a role on this (see e.g. Gratton et al. 1999).

Finally, Figure 2.5 shows the microturbulent velocities as a function of the photometric $\log g$'s, which are apparently more reliable than the spectroscopic ones, as discussed above.

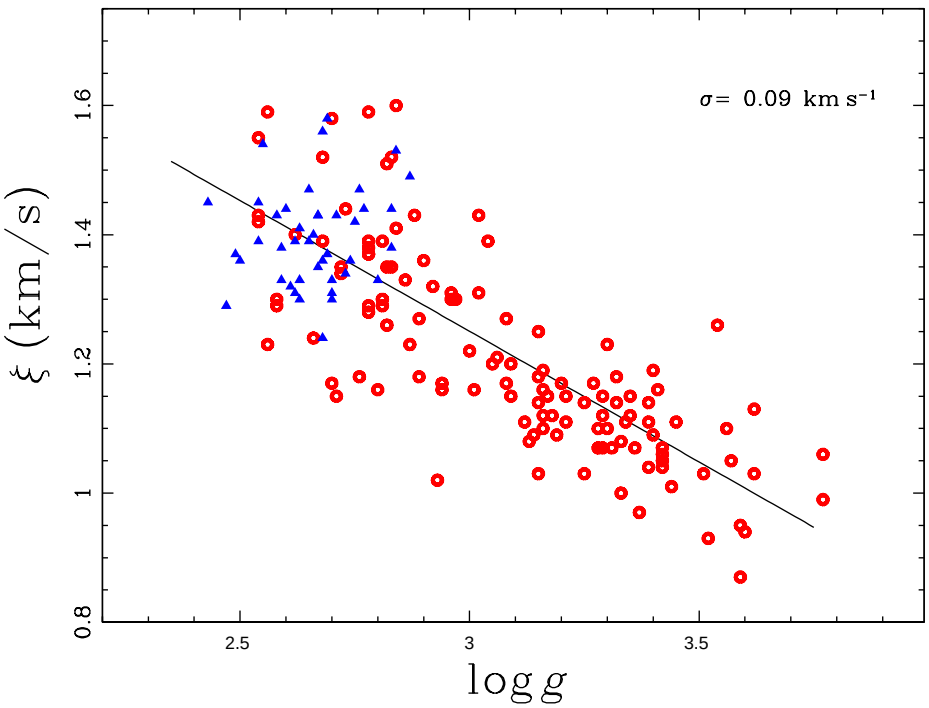

Figure 2.5: Microturbulent velocity as a function of photometric $\log g$. The red open circles correspond to RGB stars and the blue filled triangles correspond to HB stars. A linear regression yields a fit of $\xi = 2.55 - 0.45 \log g$, with a scatter of 0.09 km s^{-1}.

There is a clear correlation between these two parameters, where the microturbulent velocity decreases linearly with $\log g$. Applying a linear regression yields a fit of $\xi = 2.55 - 0.45 \log g$. A similar trend was also found by other authors, who obtained: $\xi = 2.22 - 0.322 \log g$ (Gratton et al. 1996), $\xi = 1.5 - 0.13 \log g$ (Carretta et al. 2004), $\xi = 2.29 - 0.35 \log g$ (Monaco et al. 2005) and $\xi = 1.93 - 0.254 \log g$ (Marino et al. 2008).

2.5 Masses and Evolutionary Status

We used the evolutionary tracks from Salasnich et al. (2000) to derive the mass of each star, in a similar manner to that performed in Jenkins et al. (2009) and according to the method described the Appendix B. We choose to use these models because they cover a wider range in metallicity compared to similar evolutionary tracks (for instance Girardi et al. 2002). In addition we restricted the minimum mass of the models to 1 $M_\odot$. This is due to the fact that less massive stars spend more than $\sim$10 Gyr on the main-sequence, therefore nearby (d $\lesssim$ 200

pc), low-mass stars ($\lesssim 1\,M_{\odot}$) are not expected to have reached the RGB phase yet. This method allows us to derive the mass of a giant star given its spectroscopic ($T_{eff}$and [Fe/H]) and photometric ($\log L$) parameters when the evolutionary status of the star is also known. For instance, stars cooler than $\sim$ 5000 K and less luminous than ~ 1.5 $L_{\odot}$ are ascending the RGB, and therefore their masses can be derived solely by comparing their position in the HR diagram with stellar evolution models. However, more luminous RGB stars occupy a similar position in the HR diagram as HB stars and therefore the mass and evolutionary status cannot be determined simply by comparing their effective temperature and luminosity with isomass tracks. This is the so called mass-age-metallicity degeneracy, which can be partially broken when the metallicity of the star is known (which is the case for this work).

Figure 2.6 shows two examples where the determination of the metallicity of the star is not enough to derive unambiguously its evolutionary status. In the upper panel we plot two models with the same metallicity (Z=0.008) but different masses and evolutionary status that cover a similar region in the HR diagram. The position of HIP 21743 (Z=0.008) is also shown. It can be seen that this star could either be ascending the RGB (somewhere in between A and B) or in the HB phase (between C and D). However, the time scale between points C and D is ~ 5 times longer than between A and B, therefore this star is most likely to be a HB star. The lower panel shows a similar situation for HIP 68333 (Z=0.009), but this time the two models correspond to a $1.9M_{\odot}$ RGB star and a $1.5M_{\odot}$ HB giant. Both models have the same metallicity (Z=0.008). As in the previous case, HIP 68333 could be either somewhere in between A-B or C-D, considering the error bars in $\log T_{eff}$and LogL, but in this case the timescale between points C and D is $\sim$ 45 times longer than between A and B. Once again, based on the timescales, this giant star is most likely to be on the horizontal branch. Finally, when the position of the star in the HR diagram is very close to the zero age horizontal branch, the determination of the evolutionary status is even more complicated, since the star is as likely to be in the red giant branch as in the He-burning phase, mainly due to the uncertainty in $\log T_{eff.}$ The resulting masses, radii and evolutionary status of our

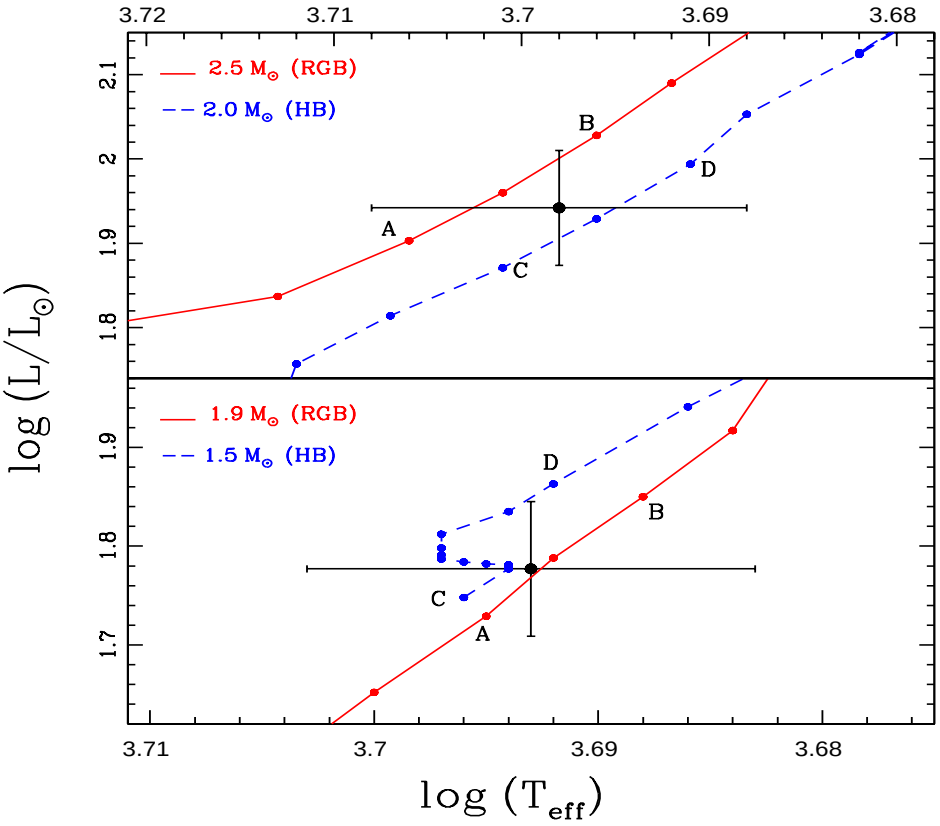

Figure 2.6: Upper panel: Position of HIP 21743 on the HR diagram (black dot). The two closest evolutionary models from Salasnich et al. (2000) are overplotted. The red solid line corresponds to a 2.5 $M_{\odot}$ RGB model, while the blue dashed line to a 2.0 $M_{\odot}$ HB model. Both tracks have a metallicity of Z=0.008. Lower panel: same as the upper plot, but this time the masses of the models are 1.9 $M_{\odot}$ for an RGB star and 1.5$M_{\odot}$ for a HB giant. The position of HIP 68333 is also shown.

targets are listed in columns 11, 12 and 13 of Table 2.2, respectively.

2.6 Rotational Velocities

Projected rotational velocities ($v \sin i$) were computed for the stars in our sample, according to the following procedure. First, we measured the FWHM for all of the Fe I lines used in the abundance analysis (see § 4.1 and § 4.2) between 6000 and 6100 Å and we averaged them to obtain the total FWHM of each star (σ_{tot}). The instrumental width (σ_{inst}) was measured from several ThAr lines present in the same spectral region, which is then substracted from σ_{tot} in order to obtain the intrinsic broadening (σ_{int}) of the star by applying: $\sigma_{int}=\sqrt{\sigma_{tot}^2 - \sigma_{inst}^2}$.

The second step consists of separating the contribution of the rotation and macroturbulence (non-thermal velocities), which are the two main line broadening mechanisms in giant stars.

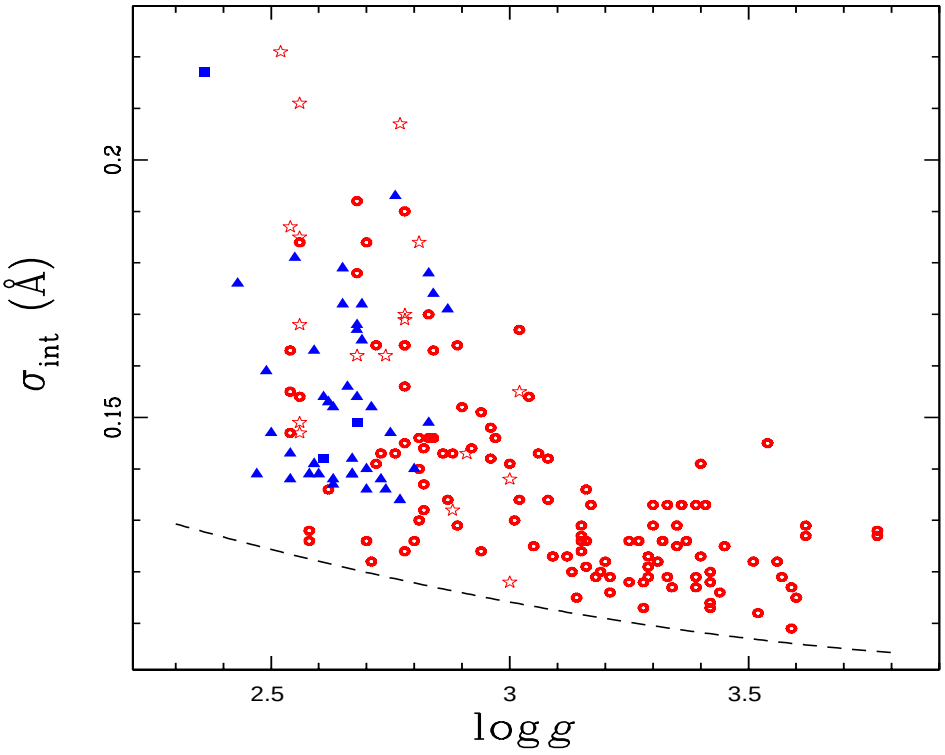

Figure 2.7: Intrinsic broadening as a function of the photometric surface gravity. The red open circles correspond to RGB stars and the blue filled triangles to HB stars. The red open stars and blue filled squares correspond to RGB and HB stars from the literature (listed in Table 2). The macroturbulence broadening is shown by the dashed black line.

Since we have a large dataset, it can be expected that many of our stars show projected rotational velocities close to zero (due to a low inclination, i.e., $\sin i \sim 0$) and therefore their intrinsic broadening is mainly due to macroturbulence broadening (σ_{mac}). These stars can be used to determine empirically σ_{mac} as a function of some intrinsic property of the star (e.g. Melo et al. 2001; Jenkins et al. 2011).

In order to do this, we plotted σ_{int} as a function of $\log g$, which is shown in Figure 2.7.

The lower envelope (dashed black line) corresponds to σ_{mac}, therefore stars lying close to this line are expected to be those with null projected rotational velocity. It can be seen that σ_{mac} increases smoothly with decreasing $\log g$, and also seems to be systematically higher for HB stars. We fit a second order polynomial of the form: $\sigma_{mac} = 0.2223 - 0.0548 \log g + 0.0063 \ \log g^2$, valid for RGB stars, while we just assumed a constant value for HB stars of $\sigma_{mac} = 0.134$ Å. It is worth mentioning that since the macroturbulence is as depth-dependent phenomenon (e.g. Takeda 1995), our derived σ_{mac} is an average of the macroturbulence broadening for different lines, which are formed at different depths in the stellar atmosphere. Using the correlations derived above, we computed the rotational broadening (σ_{rot}) by applying $\sigma_{rot} = \sigma_{int} - \sigma_{mac}$.

Table 2.1: Calibrators stars

Star	σ_{rot} (Å)	$v \sin i$ (kms^{-1})
HR 97	0.0507	3.9 [b]
HR 188	0.0636	3.0 [b]
HR 373	0.0663	4.5 [b]
HR 510	0.0240	2.9 [b]
HR 1030	0.0830	4.8 [b]
HR 1346	0.0429	2.4 [b]
HR 1373	0.0517	2.5 [b]
HR 1409	0.0417	2.5 [b]
HR 5516	0.0620	5.6 [b]
HR 5997	0.0450	3.5 [b]
HR 6770	0.0260	3.9 [b]
HR 7754	0.0412	3.2 [b]
HR 8093	0.0238	2.8 [b]
HR 8167	0.0885	5.6 [b]
HR 8213	0.0272	1.1 [b]
Pollux	0.0157	2.5 [b]
β Crv	0.0880	3.8 [a]
β Lep	0.0971	5.1 [a]
β Oph	0.0080	1.6 [c]
α Ser	0.0620	5.6 [c]
η Ser	0.0038	1.0 [c]

(a) Gray 1982 (b) Gray 1989 (c) Carney et al. 2008

Finally, in order to convert from σ_{rot} to rotational velocities, we used 21 calibrators with published $v \sin i$'s derived by the Fourier transform method, which are listed in Table 2.1. We fit a straight line obtaining: $v \sin i = 1.18 + 42.9\,\sigma_{rot}$, where σ_{rot} is in Å and $v \sin i$ in $\mathrm{km\,s^{-1}}$. The RMS of the fit is 0.89 $\mathrm{km\,s^{-1}}$. We note that $v \sin i$ doesn't approach zero at $\sigma_{rot} = 0$, which produces a small systematic shift in our derived projected rotational velocities at low σ_{rot}. We applied this conversion to all of our targets to finally obtain projected rotational velocities, which are listed in the last column of Table 2.2.

We investigated the dependence of rotation with the luminosity and the mass of the star. Figure 2.8 shows our derived $v \sin i$ versus $\log \mathrm{L}$ for all of our targets. In the lower panel the data are binned in $\Delta \log \mathrm{L} = 0.2$ dex bins, which helps to remove the dispersion due to random inclination angles. It is clear that for RGB giants, the average rotational velocity increases smoothly with the luminosity. Also, it can be noticed in Figure 2.8 that even though HB stars rotate slightly slower than RGB giants having the same luminosity, the difference is not statistically significant because of the low number of HB stars in the sample (~ 20 per bin). We also plotted $v \sin i$ against the mass of our targets in Figure 2.9. The symbols are the same as in Figure 2.8, and this time we binned the data in steps of Δ mass = 0.4 $\mathrm{M_\odot}$ bins (lower panel). It can be seen that for both, RGB and HB stars, the average rotational velocity increases with the mass of the star, and no significant difference between them is observed. Also, this plot explains the similar trend in Figure 2.8, since the most luminous stars in the sample are also the most massive ones.

2.7 Conclusions

High resolution and high S/N spectra were used to measure the atmospheric parameters ($\mathrm{T_{eff}}$, $\log g$, $\mathrm{v_t}$ and [Fe/H]) of 166 giant stars, which are the targets of our precise radial velocity program, aimed at studying the impact of the host star evolution on the inner structure of planetary systems.

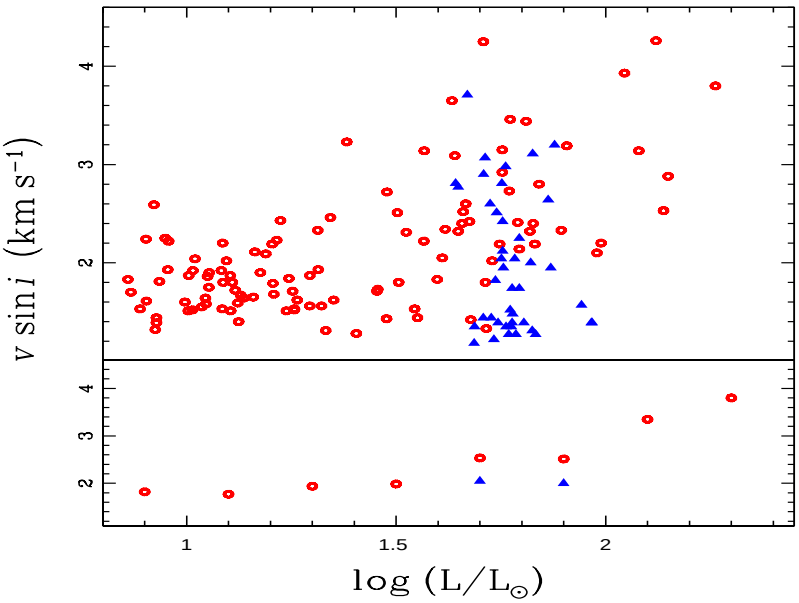

Figure 2.8: Upper panel: Projected rotational velocities against luminosity for all of our targets. The red open circles correspond to RGB stars while the blue filled triangles to HB stars. Lower panel: Same as the upper panel, but this time the data are binned in Δ log L = 0.2 dex.

We compared the resulting position in the HR diagram with evolutionary tracks in order to derive the physical properties of each star (mass, radius) and its evolutionary status. We showed the difficulties in the determination of the age and mass of stars that populate the so called "clump" in the HR diagram, since many evolutionary tracks for different masses and ages converge into this region. From the masses and radii we derived photometric gravities, which are systematically higher than the photometric values. We have also shown that the microturbulent velocity decreases linearly with $\log g$, as found previously in other works.

Finally we computed projected rotational velocities for all of our targets. We found that the rotational velocities increase with the mass and the luminosity of the stars, and no significant difference is observed between RGB and HB stars.

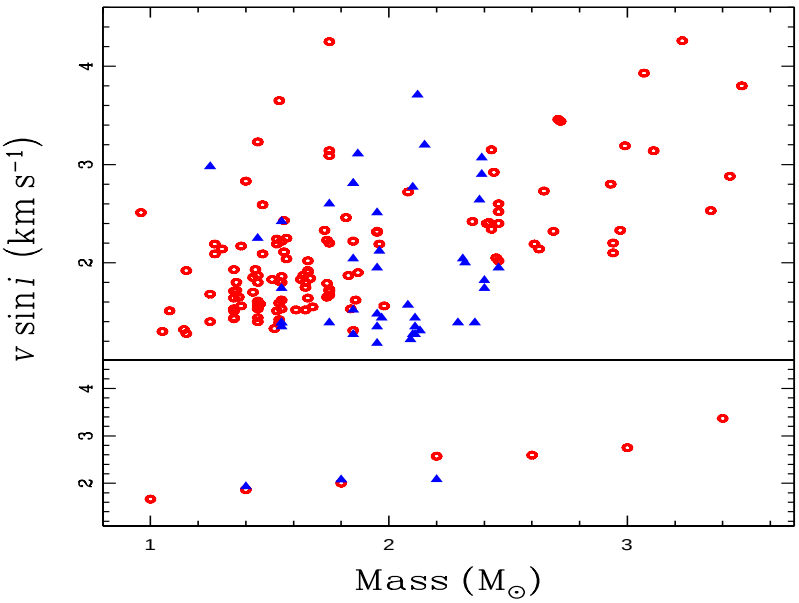

Figure 2.9: Upper panel: Projected rotational velocities against mass for all of our targets. The red open circles correspond to RGB stars while the blue filled triangles to HB stars. Lower panel: Same as the upper panel, but this time the data are binned in Δ log L = 0.2 dex.

Table 2.2: Stellar parameter of the program stars

HIP	B-V	V	π (mas)	A_V	$T_{\rm eff}$ (K)	$\log g$ (cm/s^2)	ξ (km/s)	[Fe/H]	$\log L$ ($L_\odot$)	Mass ($M_\odot$)	Radius ($R_\odot$)	Ev. St.	$v \sin i$ (km/s)
242	0.97	7.76	7.02 (0.73)	0.100	4990	3.14	1.11	-0.04 (0.06)	1.257	1.84	5.59	RGB	1.53
343	1.08	5.78	11.03 (0.45)	0.100	4790	2.51	1.34	0.14 (0.10)	1.687	1.95	10.00	HB	1.35
655	1.12	5.67	10.53 (0.38)	0.100	4750	2.59	1.33	0.12 (0.10)	1.778	1.95	11.75	HB	1.48
671	1.03	5.99	10.16 (0.42)	0.100	4960	3.01	1.49	-0.08 (0.16)	1.648	2.10	8.83	HB	2.77
873	1.00	5.84	13.33 (0.35)	0.100	4920	3.06	1.17	0.07 (0.12)	1.478	2.08	8.11	RGB	2.72
1230	1.02	7.75	7.12 (0.92)	0.100	4880	2.95	1.20	-0.09 (0.07)	1.264	1.55	5.89	RGB	1.62
1684	1.04	6.92	12.36 (0.58)	0.100	4970	3.16	1.15	0.28 (0.11)	1.104	1.83	4.74	RGB	1.87
1708	1.01	5.18	9.87 (0.41)	0.100	5020	2.73	1.44	0.16 (0.12)	1.989	2.94	12.28	RGB	2.20
3137	1.14	6.00	10.62 (0.43)	0.100	4730	2.57	1.58	0.05 (0.22)	1.642	1.85	10.20	HB	2.81
3436	1.11	6.01	17.73 (0.44)	0.100	4750	2.90	1.17	0.17 (0.09)	1.189	1.47	5.80	RGB	2.09
4293	1.10	5.45	14.70 (0.27)	0.090	4780	2.74	1.38	-0.07 (0.14)	1.567	1.75	8.94	RGB	3.14
4587	0.95	5.62	10.20 (0.53)	0.100	5010	2.80	1.33	-0.17 (0.09)	1.786	2.10	10.74	HB	1.27
4618	1.09	7.78	7.03 (0.57)	0.123	4750	2.91	1.16	0.01 (0.09)	1.294	1.45	6.77	RGB	1.56
5364	1.16	3.46	26.32 (0.14)	0.100	4770	2.96	1.36	0.24 (0.19)	1.863	2.38	11.70	HB	2.64
6116	1.03	7.89	8.06 (0.76)	0.100	4850	3.11	1.12	0.04 (0.08)	1.105	1.53	5.28	RGB	1.51
6537	1.07	3.60	28.66 (0.19)	0.100	4820	2.70	1.56	-0.13 (0.15)	1.724	1.75	10.04	HB	2.60
7118	1.07	5.79	9.77 (0.41)	0.100	4820	2.74	1.32	-0.06 (0.16)	1.783	1.85	11.18	HB	2.04
8541	1.08	7.88	5.93 (0.61)	0.100	4670	2.70	1.15	-0.15 (0.08)	1.405	1.15	7.86	RGB	1.28
9313	1.05	5.57	11.12 (0.34)	0.100	4860	2.71	1.47	-0.03 (0.14)	1.752	1.85	10.68	HB	2.81
9406	0.96	6.92	18.29 (0.51)	0.100	4950	3.37	0.93	-0.04 (0.06)	0.767	1.25	3.22	RGB	1.40
9572	0.97	5.87	9.10 (0.37)	0.100	5130	2.85	1.36	0.15 (0.10)	1.770	2.65	9.59	RGB	2.73
10164	1.00	7.06	17.30 (0.56)	0.100	4930	3.30	1.05	0.14 (0.09)	0.762	1.36	3.18	RGB	1.72
10234	0.97	5.94	8.40 (0.46)	0.092	4940	2.59	1.39	-0.17 (0.06)	1.833	1.85	11.06	HB	1.27
10326	1.01	5.86	9.40 (0.36)	0.100	4950	2.66	1.36	-0.09 (0.09)	1.769	2.11	10.28	HB	1.27
10548	0.98	7.30	11.57 (0.51)	0.193	4980	3.36	1.04	0.11 (0.07)	1.045	1.66	4.32	RGB	1.64
11600	1.05	7.34	19.98 (0.76)	0.100	4970	3.62	1.06	0.33 (0.11)	0.519	1.30	2.47	RGB	2.14
11791	1.00	5.36	12.28 (0.45)	0.070	4890	2.68	1.31	0.01 (0.08)	1.733	2.09	10.72	HB	1.22
11867	1.06	5.91	8.94 (0.35)	0.100	4770	2.32	1.31	0.18 (0.14)	1.821	2.32	12.38	HB	2.00
13147	0.98	4.45	18.89 (0.26)	0.100	4820	2.45	1.42	-0.37 (0.08)	1.747	1.53	11.02	RGB	2.19
16142	1.10	5.74	10.24 (0.47)	0.124	4940	3.10	1.60	0.21 (0.21)	1.753	2.43	9.84	RGB	3.15
16780	0.92	5.56	8.63 (0.41)	0.144	5070	2.90	1.35	-0.23 (0.07)	1.966	2.36	11.79	HB	1.39
16989	0.98	5.86	8.90 (0.43)	0.140	4960	2.59	1.35	0.00 (0.08)	1.831	2.61	11.70	RGB	2.19
17183	0.95	6.96	20.82 (0.59)	0.041	4930	3.41	0.87	-0.07 (0.07)	0.617	1.05	2.72	RGB	1.30
17351	1.19	4.59	17.70 (0.22)	0.117	4700	2.55	1.33	0.29 (0.11)	1.775	2.11	11.67	HB	1.35
17534	0.96	5.72	9.66 (0.32)	0.186	5070	2.85	1.43	0.11 (0.11)	1.819	2.69	9.88	RGB	2.32
17738	0.97	5.52	12.13 (0.30)	0.146	4910	2.63	1.39	-0.33 (0.11)	1.708	1.75	10.04	RGB	4.25
18056	1.04	7.71	5.58 (0.78)	0.207	4820	2.83	1.16	-0.17 (0.05)	1.544	1.55	8.23	RGB	1.53
18606	1.00	5.85	21.53 (0.41)	0.004	4950	3.19	1.11	0.07 (0.08)	1.014	1.61	4.50	RGB	1.52
19483	0.94	5.44	9.28 (0.37)	0.042	5080	2.72	1.37	0.13 (0.10)	1.907	2.99	11.70	RGB	3.19

19511	1.06	5.70	11.40 (0.51)	0.199	4900	2.85	1.38	0.11 (0.14)	1.712	2.39	9.87	HB	3.07
21154	1.09	7.42	10.46 (0.66)	0.209	4780	3.00	1.12	0.18 (0.09)	1.122	1.54	5.42	RGB	1.59
21685	1.05	5.46	16.63 (0.37)	0.154	4650	2.55	1.23	-0.31 (0.14)	1.503	0.96	8.53	RGB	2.51
21743	0.93	5.56	9.31 (0.33)	0.222	4990	2.82	1.39	-0.36 (0.09)	1.942	2.08	12.85	HB	1.57
22479	0.99	5.03	13.83 (0.30)	0.176	4990	2.93	1.35	0.11 (0.10)	1.790	2.42	9.93	RGB	2.41
22491	0.96	7.91	8.47 (0.71)	0.230	5000	3.23	1.07	-0.16 (0.06)	1.085	1.45	4.58	RGB	1.53
22860	0.95	5.71	6.89 (0.39)	0.242	5200	2.77	1.59	0.12 (0.07)	2.120	3.23	12.15	RGB	4.26
23067	0.96	7.67	6.80 (0.95)	0.138	5020	3.20	1.09	-0.13 (0.06)	1.332	1.85	6.08	RGB	1.31
24130	0.98	6.24	21.37 (0.45)	0.049	4910	3.22	1.01	-0.02 (0.07)	0.889	1.35	3.67	RGB	1.53
24275	1.04	7.29	9.91 (0.64)	0.099	4890	3.05	1.17	0.17 (0.10)	1.159	1.74	5.50	RGB	1.65
24426	1.01	5.75	6.56 (0.30)	0.187	5030	2.58	1.43	0.10 (0.10)	2.149	3.43	16.51	RGB	2.88
24679	0.93	5.48	20.40 (0.39)	0.051	4860	3.02	1.02	-0.36 (0.07)	1.238	1.08	5.91	RGB	1.51
26019	1.09	5.75	12.67 (0.31)	0.124	4690	2.54	1.24	0.00 (0.10)	1.598	1.63	9.91	RGB	1.83
26649	0.91	5.44	7.73 (0.27)	0.114	5220	2.94	1.39	0.08 (0.10)	2.079	3.11	11.92	RGB	3.14
27243	1.04	5.31	6.95 (0.19)	0.183	5120	2.81	1.59	0.23 (0.12)	2.262	3.48	16.25	RGB	3.80
27434	1.06	7.85	9.57 (0.51)	0.152	4830	3.08	1.08	0.13 (0.09)	0.996	1.45	4.32	RGB	1.60
33139	0.99	6.24	18.48 (0.37)	0.100	5060	3.36	1.11	0.15 (0.09)	1.015	1.66	4.03	RGB	1.92
35154	1.06	7.69	17.45 (0.45)	0.104	4930	3.50	0.99	0.35 (0.12)	0.504	1.27	2.44	RGB	2.19
39738	0.95	6.69	14.42 (0.37)	0.062	4980	3.26	1.07	-0.06 (0.07)	1.046	1.46	4.54	RGB	1.58
41683	1.02	7.14	16.82 (0.61)	0.110	4980	3.35	1.10	0.20 (0.09)	0.751	1.43	3.29	RGB	1.85
41856	1.05	7.59	11.16 (0.52)	0.100	4900	3.18	1.09	0.17 (0.09)	0.935	1.54	4.11	RGB	1.81
56260	1.05	6.74	16.53 (0.68)	0.019	4890	3.12	1.14	0.23 (0.12)	0.903	1.53	4.14	RGB	2.24
56640	1.08	7.94	8.18 (0.66)	0.163	4780	2.94	1.10	0.09 (0.09)	1.109	1.45	5.26	RGB	1.80
58782	1.04	7.49	8.73 (0.79)	0.115	4810	2.81	1.20	-0.15 (0.08)	1.208	1.25	5.54	RGB	1.68
59016	1.07	7.03	9.75 (0.53)	0.104	4800	2.88	1.16	0.07 (0.10)	1.294	1.64	6.64	RGB	1.87
59367	1.00	7.50	10.06 (0.83)	0.019	4960	3.08	1.12	-0.01 (0.07)	1.020	1.57	4.39	RGB	2.04
60035	1.05	7.99	9.91 (0.60)	0.293	4890	3.17	1.07	0.23 (0.11)	0.957	1.55	4.32	RGB	2.22
60374	1.01	6.52	7.56 (0.59)	0.131	4940	2.60	1.33	-0.04 (0.08)	1.708	2.11	9.60	HB	1.44
60396	1.06	6.82	6.66 (0.40)	0.240	4810	2.52	1.45	-0.18 (0.08)	1.762	1.55	11.10	HB	1.35
62447	1.05	6.81	7.29 (0.46)	0.233	4990	2.88	1.32	0.13 (0.10)	1.657	2.46	9.025	RGB	2.40
63242	1.02	6.86	7.42 (0.49)	0.200	4830	2.53	1.52	-0.31 (0.09)	1.633	1.54	9.41	RGB	3.65
63243	1.07	6.31	8.41 (0.38)	0.218	4880	2.57	1.43	-0.08 (0.08)	1.743	1.75	10.15	HB	1.39
63583	1.04	6.65	7.50 (0.54)	0.203	4800	2.46	1.40	-0.22 (0.10)	1.713	1.65	10.44	RGB	1.80
63981	1.02	6.75	9.05 (0.52)	0.210	4840	2.85	1.26	-0.22 (0.08)	1.506	1.55	8.04	RGB	1.80
64580	1.08	5.91	9.16 (0.52)	0.163	4770	2.55	1.41	0.02 (0.11)	1.825	2.13	11.73	HB	1.31
64590	1.08	6.72	6.59 (0.55)	0.222	4870	2.70	1.42	0.18 (0.12)	1.794	2.40	10.84	HB	1.74
64647	1.09	7.83	6.70 (0.65)	0.240	4870	2.92	1.21	0.01 (0.14)	1.343	1.82	6.61	RGB	2.46
64803	0.96	5.10	12.66 (0.28)	0.168	5060	2.63	1.39	0.04 (0.09)	1.827	2.41	10.14	RGB	2.40
65238	1.08	7.96	7.28 (0.68)	0.076	4810	2.82	1.15	0.14 (0.09)	1.163	1.56	5.39	RGB	2.11
65373	1.03	6.77	5.17 (0.53)	0.227	4920	2.75	1.34	0.15 (0.09)	1.979	2.94	12.42	RGB	2.10
65891	1.00	6.75	7.35 (0.60)	0.202	5000	2.90	1.30	0.16 (0.10)	1.660	2.46	8.52	RGB	2.52
66427	0.94	5.96	7.86 (0.47)	0.197	5180	3.00	1.37	0.12 (0.08)	1.894	2.97	11.65	RGB	2.33
66711	0.99	7.55	9.64 (0.76)	0.155	5000	3.22	1.00	0.13 (0.12)	1.086	1.75	4.75	RGB	2.20

66924	1.02	5.96	9.06 (0.42)	0.177	4860	2.53	1.43	-0.18 (0.10)	1.805	1.55	10.60	HB	1.39
67537	0.99	6.43	8.88 (0.46)	0.179	4985	2.85	1.31	0.15 (0.08)	1.617	2.43	8.57	RGB	2.34
67851	1.01	6.17	15.16 (0.39)	0.115	4890	3.15	1.14	0.00 (0.10)	1.244	1.67	5.71	RGB	1.84
67890	1.13	6.05	15.42 (0.43)	0.145	4750	2.81	1.22	0.31 (0.14)	1.313	1.73	6.90	RGB	2.33
68054	0.97	6.83	6.27 (0.51)	0.251	5110	2.90	1.43	0.13 (0.08)	1.772	2.71	8.44	RGB	3.46
68099	0.96	6.83	5.95 (0.55)	0.317	5130	3.00	1.29	0.15 (0.08)	1.841	2.93	11.57	RGB	2.80
68263	0.98	7.03	11.91 (0.88)	0.172	4870	3.05	1.11	-0.11 (0.08)	1.136	1.35	5.31	RGB	1.64
68333	0.96	5.92	9.42 (0.48)	0.174	4925	2.55	1.44	-0.32 (0.09)	1.777	1.55	10.36	HB	1.39
69065	1.01	6.39	8.89 (0.53)	0.210	4960	2.62	1.51	-0.22 (0.09)	1.648	1.95	9.02	RGB	2.32
70261	1.03	6.80	7.24 (0.62)	0.284	4810	2.65	1.30	-0.38 (0.07)	1.715	1.52	10.49	RGB	1.33
70514	1.09	6.83	9.47 (0.56)	0.220	4750	2.65	1.29	-0.12 (0.09)	1.454	1.35	7.59	RGB	1.71
70987	1.06	5.99	10.35 (0.50)	0.206	4880	2.64	1.44	-0.03 (0.07)	1.686	1.95	9.55	HB	1.18
71778	0.96	7.87	10.51 (0.75)	0.110	5040	3.45	1.03	0.03 (0.12)	0.860	1.51	3.58	RGB	1.83
72097	1.01	6.10	9.71 (0.37)	0.193	5000	2.72	1.41	-0.03 (0.10)	1.675	2.35	9.67	RGB	2.42
72618	0.99	7.86	9.99 (1.17)	0.115	4930	3.14	1.10	-0.28 (0.11)	0.925	1.14	4.06	RGB	1.32
73758	1.12	7.92	12.17 (0.69)	0.095	4840	3.20	1.26	0.41 (0.15)	0.735	1.40	3.33	RGB	2.83
74188	1.06	7.12	12.45 (0.73)	0.185	4750	2.95	1.16	0.12 (0.12)	1.087	1.36	5.09	RGB	1.80
74239	1.05	5.75	7.67 (0.42)	0.256	5000	2.77	1.58	0.07 (0.15)	2.045	3.07	13.00	RGB	3.93
74890	1.05	7.05	10.93 (0.63)	0.195	4850	3.06	1.19	0.20 (0.13)	1.215	1.74	5.76	RGB	2.23
75092	1.03	7.11	12.98 (0.77)	0.364	4940	3.17	1.10	0.09 (0.11)	1.095	1.66	4.79	RGB	2.02
75101	1.06	6.34	28.53 (0.54)	0.079	4880	3.35	1.03	0.29 (0.13)	0.614	1.27	2.90	RGB	2.09
75331	1.08	7.59	15.09 (0.62)	0.152	4880	3.33	1.13	0.31 (0.14)	0.696	1.38	3.02	RGB	2.17
76532	1.07	5.79	11.87 (0.53)	0.394	4850	2.77	1.30	0.02 (0.08)	1.727	1.97	10.40	HB	1.44
76569	1.08	5.82	11.45 (0.61)	0.406	4830	2.78	1.38	-0.18 (0.15)	1.754	1.55	10.48	HB	2.42
77059	0.96	6.62	12.47 (0.47)	0.377	5010	3.14	1.09	0.01 (0.09)	1.322	1.98	5.93	RGB	1.56
77888	1.12	7.70	7.72 (0.65)	0.268	4690	2.63	1.23	0.02 (0.13)	1.314	1.35	7.08	RGB	1.93
78752	0.99	7.28	16.55 (0.92)	0.154	4970	3.47	0.94	0.09 (0.09)	0.728	1.38	3.09	RGB	1.56
78868	1.17	5.70	11.21 (0.36)	0.174	4660	2.38	1.30	0.30 (0.16)	1.756	1.95	11.22	HB	1.95
80672	1.10	5.79	9.06 (0.37)	0.349	4710	2.47	1.29	0.03 (0.08)	1.968	2.29	14.62	HB	1.39
80687	0.95	6.89	16.94 (0.60)	0.332	5020	3.30	1.07	0.03 (0.07)	0.928	1.54	4.02	RGB	1.39
82135	0.98	5.48	11.30 (0.39)	0.196	4970	2.78	1.30	0.06 (0.09)	1.794	2.63	10.59	RGB	2.14
82653	1.19	7.57	8.01 (0.83)	0.618	4790	2.80	1.18	0.04 (0.10)	1.456	1.75	7.88	RGB	1.73
83224	1.10	7.35	9.46 (0.77)	0.288	4880	2.91	1.25	0.07 (0.08)	1.253	1.75	5.84	RGB	1.71
83235	1.16	5.95	10.10 (0.38)	0.218	4720	2.56	1.24	0.35 (0.13)	1.751	2.31	11.53	HB	2.04
84056	1.03	6.81	13.31 (0.59)	0.209	4960	3.17	1.12	0.08 (0.07)	1.129	1.75	4.97	RGB	1.67
84248	1.07	5.87	10.00 (0.41)	0.137	4730	2.42	1.45	-0.12 (0.11)	1.761	1.25	11.31	HB	2.98
85250	0.96	6.79	13.14 (0.54)	0.154	4980	3.15	1.15	-0.17 (0.08)	1.124	1.45	4.96	RGB	1.40
86208	1.08	7.45	6.89 (0.59)	0.383	4730	2.73	1.17	-0.16 (0.07)	1.551	1.35	8.61	RGB	1.44
86248	1.11	5.89	9.82 (0.43)	0.133	4680	2.28	1.36	0.02 (0.11)	1.777	1.55	11.62	HB	1.74
86368	1.00	7.43	13.04 (1.00)	0.102	4880	3.13	1.05	0.12 (0.11)	0.867	1.43	3.87	RGB	1.70
86786	0.98	7.21	10.27 (0.62)	0.370	4970	3.07	1.08	-0.12 (0.07)	1.257	1.65	5.80	RGB	1.52
87273	1.11	7.02	11.32 (0.68)	0.223	4750	2.64	1.27	0.21 (0.13)	1.224	1.56	5.98	RGB	2.43
88684	0.97	5.74	27.20 (0.38)	0.122	4940	3.24	1.04	0.04 (0.07)	0.904	1.45	3.90	RGB	1.61

90124	1.02	5.52	11.38 (0.35)	0.096	4950	2.73	1.44	0.09 (0.09)	1.737	2.40	9.89	HB	1.82
90606	1.17	5.95	8.40 (0.28)	0.193	4420	2.09	1.02	0.15 (0.19)	1.973	1.35	17.18	HB	1.31
90988	1.04	7.75	9.17 (0.75)	0.136	4910	3.21	1.14	0.24 (0.14)	1.054	1.66	4.68	RGB	1.90
92367	0.89	5.80	9.10 (0.31)	0.137	5040	2.68	1.39	-0.43 (0.16)	1.826	1.87	10.74	HB	3.11
95124	1.02	7.55	9.04 (0.61)	0.254	5040	3.28	1.18	0.20 (0.08)	1.176	1.87	4.97	RGB	1.90
95532	0.95	6.66	16.41 (0.53)	0.082	4970	3.20	0.97	-0.04 (0.08)	0.955	1.44	4.11	RGB	1.93
96760	1.04	5.97	9.10 (0.84)	0.253	4980	2.86	1.52	0.12 (0.18)	1.810	2.72	10.53	RGB	3.44
97233	1.00	7.34	9.39 (0.70)	0.190	5020	3.26	1.23	0.29 (0.13)	1.204	1.96	5.20	RGB	2.19
98482	1.06	6.18	9.64 (0.38)	0.155	4720	2.51	1.29	-0.17 (0.10)	1.678	1.54	10.56	RGB	1.42
98575	0.98	6.01	9.29 (0.38)	0.249	5150	2.81	1.39	0.15 (0.10)	1.753	2.44	7.83	RGB	2.92
99171	1.02	5.97	21.30 (0.46)	0.029	4830	3.07	1.03	-0.01 (0.08)	1.004	1.35	4.57	RGB	1.51
100062	1.00	5.86	10.31 (0.48)	0.297	4920	2.57	1.43	-0.09 (0.10)	1.772	1.85	10.44	HB	1.52
101477	1.00	5.12	13.94 (0.34)	0.128	4980	2.78	1.35	0.05 (0.10)	1.729	2.46	10.13	RGB	2.02
101911	1.02	6.46	13.44 (0.50)	0.045	4885	2.97	1.18	0.03 (0.08)	1.206	1.74	5.82	RGB	1.79
102014	1.12	5.47	13.77 (0.32)	0.119	4710	2.65	1.34	-0.02 (0.18)	1.640	1.75	9.58	RGB	3.09
102773	1.12	5.41	10.80 (0.31)	0.158	4780	2.58	1.54	0.01 (0.16)	1.878	2.15	12.92	HB	3.20
103836	1.11	5.93	14.85 (0.49)	0.112	4740	2.89	1.27	-0.06 (0.16)	1.382	1.45	7.17	RGB	3.23
104148	1.05	5.69	10.82 (0.64)	0.142	4805	2.45	1.40	0.03 (0.11)	1.754	1.96	10.87	HB	2.12
104838	1.01	6.89	15.67 (0.50)	0.119	4900	3.18	1.06	0.04 (0.07)	0.928	1.45	3.80	RGB	1.44
105854	1.19	5.64	12.37 (0.31)	0.162	4780	2.94	1.47	0.31 (0.18)	1.670	2.12	10.07	HB	3.71
105856	1.02	6.70	14.59 (0.41)	0.085	4915	3.08	1.14	0.09 (0.10)	1.050	1.55	4.90	RGB	1.86
106055	1.11	7.16	7.19 (0.75)	0.136	4770	2.68	1.33	0.15 (0.14)	1.524	1.95	8.61	RGB	2.31
106922	1.07	7.25	8.22 (0.74)	0.127	4875	2.96	1.15	0.12 (0.10)	1.351	1.86	6.45	RGB	1.62
107122	0.97	7.18	10.98 (0.81)	0.132	4965	3.27	1.07	0.10 (0.08)	1.116	1.75	4.86	RGB	1.72
107773	1.02	5.62	9.65 (0.40)	0.167	4945	2.59	1.43	0.03 (0.10)	1.869	2.46	11.49	HB	1.95
108543	1.00	5.50	7.54 (0.32)	0.200	4995	2.41	1.55	0.05 (0.10)	2.138	3.35	16.31	RGB	2.53
109228	0.95	7.15	16.48 (0.69)	0.094	4960	3.31	0.95	0.02 (0.08)	0.761	1.37	3.11	RGB	1.65
110391	1.06	5.12	19.07 (0.29)	0.088	4750	2.69	1.28	-0.18 (0.08)	1.477	1.35	7.86	RGB	1.43
110529	0.98	5.53	12.45 (0.44)	0.161	5060	2.80	1.30	0.13 (0.11)	1.666	2.46	8.62	RGB	2.60
111515	0.98	5.97	10.76 (0.43)	0.134	5030	2.97	1.31	0.14 (0.07)	1.610	2.45	8.03	RGB	2.05
111909	1.03	7.37	12.18 (0.74)	0.118	4930	3.24	1.16	0.23 (0.11)	0.949	1.57	4.10	RGB	2.25
112862	0.91	5.99	10.11 (0.44)	0.100	5080	2.90	1.14	-0.05 (0.11)	1.637	2.36	8.16	RGB	3.20
113779	0.97	7.76	9.21 (1.03)	0.147	5020	3.42	1.11	0.11 (0.08)	1.036	1.68	4.34	RGB	1.55
114408	0.96	6.47	15.72 (0.46)	0.085	4880	3.12	1.03	-0.25 (0.09)	1.083	1.15	4.74	RGB	1.92
114775	1.16	5.77	13.06 (0.35)	0.100	4660	2.57	1.18	0.26 (0.13)	1.566	1.85	9.41	RGB	2.22
114933	1.03	7.25	11.35 (0.93)	0.100	4920	3.09	1.15	0.14 (0.08)	1.053	1.65	4.83	RGB	1.75
115620	1.06	5.60	11.23 (0.31)	0.106	4820	2.72	1.37	0.07 (0.18)	1.740	1.95	10.47	HB	2.51
115769	0.98	5.63	10.38 (0.27)	0.110	4850	2.67	1.37	-0.27 (0.13)	1.794	1.45	11.39	HB	2.25
116630	1.03	7.47	11.98 (0.59)	0.102	4900	3.18	1.19	0.16 (0.14)	0.922	1.47	4.01	RGB	2.59
117314	1.07	5.74	10.69 (0.39)	0.100	4920	3.00	1.53	0.07 (0.16)	1.709	2.39	9.75	HB	2.90
117411	1.08	7.60	10.44 (0.71)	0.100	4800	3.04	1.17	0.17 (0.11)	1.005	1.45	4.63	RGB	1.87

Chapter 3

Results from the CTIO Sample

3.1 Introduction

Around 500[1] exoplanets have been confirmed by the radial velocity (RV) technique, most of them orbiting late F, G and K dwarf stars. The RV detection of planets orbiting main-sequence (MS) stars with spectral types earlier than F0-F5 is very challenging because these stars are too hot and thus show very few absorption lines which are also broadened due to fast rotation. However, after the MS, early type stars become cooler and rotate slower than their former progenitors, showing a spectrum with many narrow absorption lines, which are neccessary to obtain a RV precision at the $\mathrm{m\,s^{-1}}$ level. Additionally, even though they are more active than solar-type stars, giant stars bluer than B-V $\sim$ 1.2 present a stellar jitter at the $\sim$20 $\mathrm{m\,s^{-1}}$ level (Hekker et al. 2006), meaning it is possible to detect giant planets ($\mathrm{M} \gtrsim 1.0\,\mathrm{M}_J$) orbiting them. Therefore, evolved stars are suitable RV targets for probing the planetary population around intermediate-mass stars ($\mathrm{M}_\star \gtrsim 1.5\,\mathrm{M}_\odot$) and studying the effect of the star-planet interactions, after the MS.

To date around 40 planets have been detected orbiting intermediate-mass giants, but none of them within 0.6 AU from the host star. This observational fact contrasts with the observed planetary population around solar-type stars, where a fraction of them host a giant planet in a close-in orbit (see e.g. Cumming et al. 2008), suggesting that these planets are destroyed

[1]As of September, 2012. Source: http://exoplanet.eu/

by the large envelope of the host star during its post-MS evolution. This idea was predicted theoretically to be due to tidal decay that leads to the engulfment of close-in planets during the RGB ascent of the host star (e.g. Siess & Livio 1999; Sato et al. 2008; Villaver & Livio 2009). On the other hand, the population of planets around subgiant stars has revealed a lack of giant planets orbiting between 0.1 and 0.6 AU from the host star (Johnson et al. 2011). Since subgiant stars have not evolved enough to the point of affecting the orbits of planets, this observational result suggests that the primordial distribution and/or migration efficiency of giant planets around intermediate-mass stars is different to the one observed in low-mass stars.

We are conducting a RV study of 166 giant stars in order to determine the fraction of close-in planets ($a \lesssim 0.6$ AU) orbiting Red Giant Branch (RGB) and Horizontal Branch (HB) stars. These results might give us some information about the effect of the star-planet tidal interactions during the RGB phase. In particular, if the inner planets are efficiently destroyed after spiral inward during the late phase of the RGB (when the radius of the star is larger and hence the tidal effect is stronger), then it can be expected that there is a lower fraction of close-in planets orbiting HB stars than around RGB stars.

In this paper, we present the first RV results of our program, including a sample of 66 giant stars, that were observed with the 1.5 m telescope at Cerro Tololo (CTIO sample). The results for the rest of the targets (observed with FEROS), along with the study of the RGB and HB planet populations will be presented in a forthcoming paper (Jones et al. 2013, in preparation).

This paper is organized as follows. In section 2 and 3 the targets selection, the observations and data reduction is briefly summarized. In section 4 we explained the technique used to compute the RV's. The results are presented in section 5 and finally the conclusions are summarized in section 6.

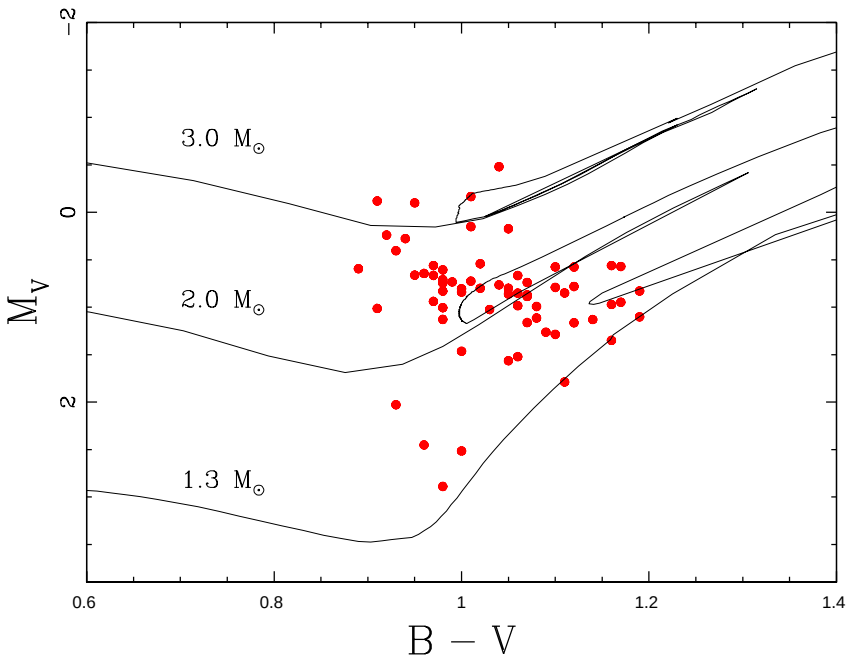

Figure 3.1: Position in the color-magnitude diagram of our CTIO sample (red filled dots). Different isomass tracks from Marigo et al. (2008) are overplotted, for stars with $M_\star = 1.3$, 2.0 and 3.0 $M_\odot$ (solid lines from bottom to top), and solar metallicity.

3.2 Targets

We have selected a total of 166 bright giant stars in the southern hemisphere, according to the criteria explained in Jones et al. (2011). The atmospheric parameters and physical properties, including the evolutionary status of 164 of them are also presented in that work. We added 2 more targets to the original sample. The atmospheric and physical parameters for both of them are also listed in Table 2.2. In this work we present the results for the CTIO sample, compounded by 66 clump giants. The position of our CTIO targets in the color-magnitude diagram is shown in Figure 3.1. Three isomass tracks from Marigo et al. (2008) are overplotted, for star with $M_\star = 1.3$, 2.0 and 3.0 $M_\odot$, and solar metallicity. As can be noticed, these stars fall in the clump region of the color-magnitude diagram, where there is an overlap between evolutionary tracks from the RGB and HB phases.

3.3 Observations and data reduction.

The sample of stars presented in this paper were observed from August 2009 until December 2010 using the Fiber Echelle Spectrograph (FECH) and then with CHIRON (Spronck et al. 2011; Tokovinin et al. 2012), starting on March of 2011 until September of 2012, both mounted at the 1.5m telescope, placed at CTIO. We collected a total of $\sim$ 15 spectra for each target, during a period of $\sim$ 2 years, assigning to all of them the same priority, resulting in a nearly homogeneous dataset.

The FECH spectra were taken using two different setups: with a 60 micron slit leading to a resolution of $\sim$48,000 and a very low total efficiency ($\sim$1%) and using a 90 microns slit, increasing significantly the S/N but at cost of a loss in resolution (R$\sim$42,000). In both cases a molecular iodine (I_2) cell was set in the light path to superimpose thousands of absorption lines on top of the stellar spectrum and these are used as a precise wavelength reference. The I_2 cell absorption spectrum removes more than 40% of the light between 5000-6000 Å, decreasing considerably the light collected. The typical exposure time for the targets (only two of them are fainter than V=6 mag) was 300 seconds, which leads to a signal to noise ratio over 100 at the center of the orders around 5500 Å, when observed in good atmospheric conditions.

The CHIRON data were also taken using two different setups. For the templates (I_2 free observations) the narrow slit (R$\sim$120,000) was used while for the normal observations (with the I_2 cell in the light beam) the normal slit (R$\sim$90,000) was used. The exposure time for the star + I_2 observations was between 300 and 800 seconds, while for the templates we increased the exposure time up to 1200 seconds in order to reach a higher S/N. Since the templates are I_2 free spectra, the loss in the efficiency of the narrow slit is compensated by the fact that no light is absorbed by the I_2 cell, and therefore the total efficiency of both modes (normal slit and the narrow slit + I_2) is very similar ($\sim$4%).

The reduction of the data was performed in the standard way (bias substraction, overscan trimming, flatfield normalization, order tracing, extraction and wavelength calibration)

using two different pipelines (for FECH data and for CHIRON data; the latter available for service mode observations) and in some cases using IRAF scripts (imred / echelle package). The calibartion data as usual were taken either in the afternoon, just before the observations, or in the morning after the end of the night.

3.4 Data Analysis

In this work we applied the iodine cell technique for computing the RV's of our targets. The main idea of this technique is to pass the starlight through a vapor I_2 cell, which superimpose thousands of absoprtion lines in the region between 5000 and 6000 Å. These lines are then used as a precise wavelength reference, against which we can measure the doppler shift of the stellar spectrum. The normalized observed spectrum (I_{obs}) is then modelled by:

$$I_{obs} = [I_{st}(\lambda + \Delta\lambda)\, I_{iod}(\lambda)] * IP \tag{3.1}$$

where I_{st} and I_{iod} are the normalized instrinsic spectrum of the star and the transmission spectrum of the I_2 cell. $\Delta\lambda$ corresponds to the stellar doppler shift and IP is the instrumental profile, which is a function of λ and the position in the CCD. In order to model equation 3.1 and derive $\Delta\lambda$ (which finally translates into a radial velocity) we mainly followed the procedure described in Butler et al. (1996), though with some slight modifications. First, in order to compute the IP, we passed the light from a quartz lamp through the I_2 cell, instead of using a rapidly rotating B star as a featureless background source. Since both, FECH and CHIRON are fed by a fiber, the light from the star and from the quartz lamp follow the same path before reaching the I_2 cell and the spectrograph, ensuring a nearly constant illumination. Secondly, the IP was modeled by a central gaussian and only two small flanking gaussians. The position and width of these 3 functions are fixed (but they change for different setups and instruments), while the amplitudes are left as free parameters. Finally, we solved equation 3.1 for chunks of $\sim$5 Å, corresponding to $\sim$ 80 pixels in the FECH spectra. We found that

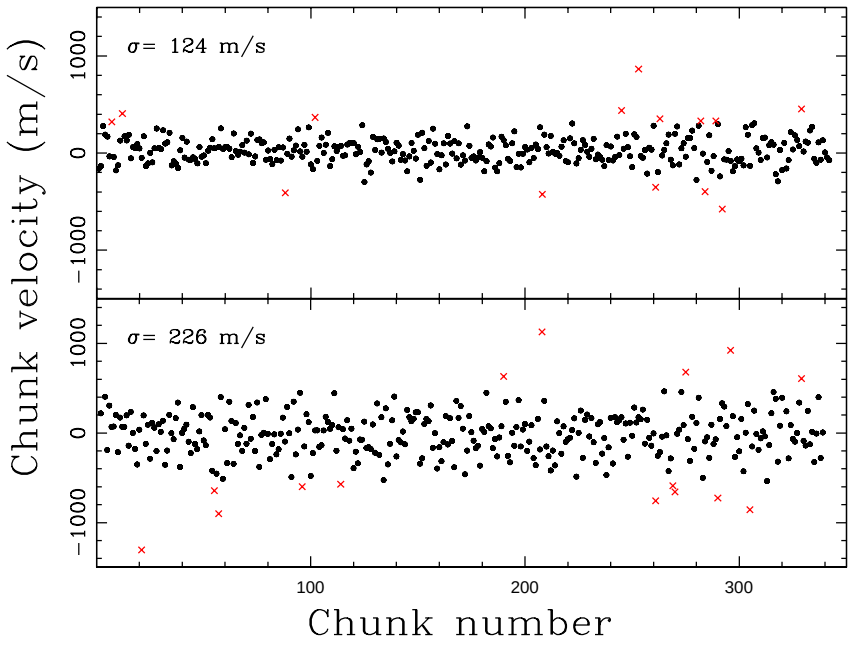

Figure 3.2: Radial velocities derived from 342 different chunks. The solid black dots correspond to the chunks velocities. The red crosses correspond to the rejected velocities. The upper and lower panel correspond a CHIRON and FECH spectrum, respectively. The standard deviation in each case is also labelled.

in our data this length leads to the lowest RV uncertainties. In order to simultaneously use both datasets, we rebinned the CHIRON data to the FECH resolution, at expense of losing information in the gradient of the lines but not in the width of the lines, and therefore the measured IP width in CHIRON data remains largely unchanged.

3.4.1 Radial velocity calculation

As already mentioned above, the doppler shift ($\Delta\lambda$) is computed for each 5 Å chunk. We included a total of 342 chunks (19 chunks on each of 18 different orders) in the wavelength region between 5000 and 6000 Å. This procedure is performed at each observational epoch, resulting in a large set of velocities for every star. The final RV curve is built as follows: firstly, for a given star, at each epoch we compute the mean velocity of the 342 chunks, rejecting every point that lies further away than 2.5 sigma (typically less than 10% of the chunks are rejected). An example of this is shown in Figure 3.2, where we plot the velocity

of every chunk from a single observation (black dots). The rejected velocities are shown with red crosses. The upper and lower panel correspond to CHIRON and FECH observations, respectively. After the outlier rejection, the next step consists of weighting every specific chunk based on how deviant are the velocities it produces with respect to the mean velocity at different epochs. The chunk weights are assign by:

$$\sigma_j^2 = \sum_{i=1}^{n} (v_j - \overline{v_i}) \tag{3.2}$$

where v_i is the j-th chunk velocity a the i-th epoch, $\overline{v_i}$ is the mean velocity from all of the chunks at that specific epoch and n correspond to the total number of spectra taken for the star under analysis. Then the weight for the j-th chunk (ω_j) is simply given by:

$$\omega_j = \frac{A}{\sigma_j^2} \tag{3.3}$$

where A is a normalization constant, so that $\sum \omega_j = 1$.

As can be noticed from the last two equations, a chunk that gives velocities that are consistent with the mean velocity at different epochs is assigned with a high weight, while chunks leading to deviant velocities have lower weights. Once the weights for every chunk are computed the final radial velocity at the i-th epoch is computed by:

$$v_i = \sum_{j=1}^{n_c} \omega_j \, v_j \tag{3.4}$$

where n_c is the number of non-rejected chunks. The final radial velocity is then obtained by subtracting the barycentric velocity computed at the mean time of the observation from v_i.

The weighting scheme described above takes into consideration several factors regarding the intrinsic information of the stellar spectrum contained in a specific chunk and differences inherent to the observation itself, like the S/N or the difference in the resolution across the orders. For instance, the doppler shifts computed from chunks having few or very shallow lines, are expected to depart from the mean radial velocity of the star. Also, the chunks close to the edges of the orders usually have a low S/N and therefore they lead to deviant velocities due to a poor IP modelling. The same is valid for the template, which has regions with lower S/N and/or chunks where the deconvolution process was poor. This whole procedure allows us to improve the RV precision, which is observed in the RV scatter of the most "stable" stars. An example of this is shown in Figure 3.3. In the upper panel we plot the RV curve of HIP1708. Each datapoint correspond to the mean chunk velocity, computed at each epoch. The error bars are computed from the error in the mean chunks velocities [2].

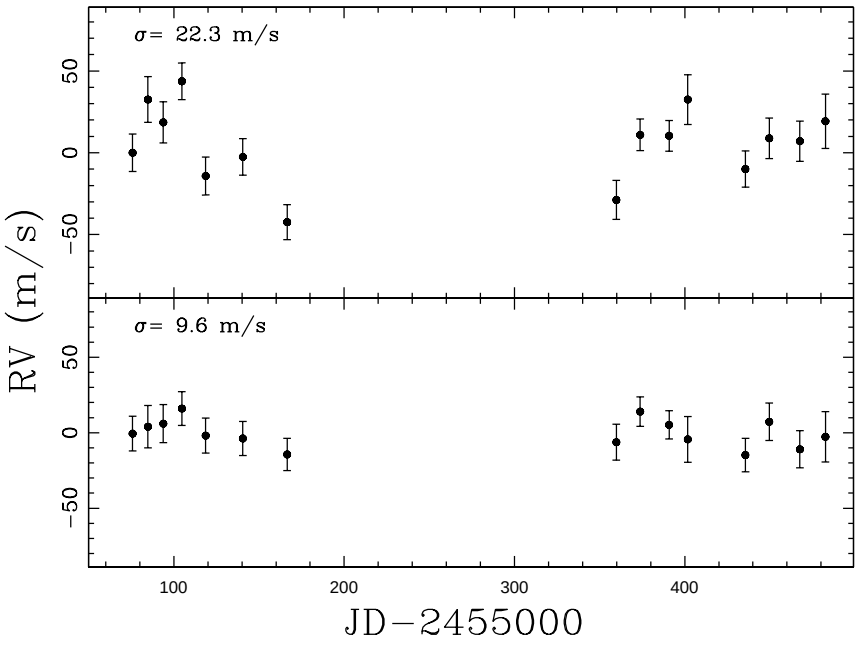

Figure 3.3: RV's computed for one of our targets. In the upper panel the RV at each epoch is computed from the mean velocity of the chunks. In the lower panel the final RV's are computed using the weighting method described in § 4.1.

The weighted standard deviation (defined in equation 3.5) of the data in this case is 22.3

[2]The error in the mean is given by: $\sigma/\sqrt{n_c}$, where σ is the standard deviation of the chunks velocities and n_c is the number of non-rejected chunks used in the analysis

$m\,s^{-1}$. In the lower panel we plotted the new result after applying the outlier rejection and the weighting method described above. Note that the dispersion drops down to 9.6 $m\,s^{-1}$, revealing the actual "stable" nature of this star. The same is observed in every flat star in our sample, showing the importance of this procedure in order to achieve RV precision better than 10 $m\,s^{-1}$. It is important to mention that since the error bars are computed from the dispersion in the individual chunk velocities and thus the weighting method just described is not taken into consideration, the actual value of the error bars (in the absence of systematic effects) should be slighlty lower than the given value. For FECH data the error bars are typically $\sim$10-15 $m\,s^{-1}$, while for CHIRON they are between 5-8 $m\,s^{-1}$. Since CHIRON data are rebinned to the FECH resolution and most of the stars were observed with the normal slit (R$\sim$ 90,000) and a S/N below 100, it is likely that CHIRON can reach a single shot precision of 2-3 $m\,s^{-1}$ when working with high S/N data taken with the narrow slit (R$\sim$ 120,000).

Finally it is worth mentioning that the CHIRON RV's are systematically higher than FECH ones. In order to find the RV shift between both datasets we used three "stable" stars that were observed several times with each spectrograph. We obtain a shift of 35 $m\,s^{-1}$, which was then substracted from all of the CHIRON velocities. The final RV's for all of our CTIO targets can be found at the end of this chapter, in Figures 3.6 - 3.14.

3.5 Results

3.5.1 Stellar Variability

As already known from extensive previous studies (e.g. Setiawan et al. 2004; Hekker et al. 2006) giant stars are intrisically RV variable at the $\sim$10-100 $m\,s^{-1}$ level, mainly due to solar-like oscillations, having typical timescales from hours up to a few days and RV amplitudes of several $m\,s^{-1}$ (see e.g. Barban et al. 2004; Zechmeister et al. 2008; Bedding et al. 2010). Even though this level of variability is exceedingly large to search for planetary signals, Hekker et al. (2006) showed that a significant fraction of clump giants having a B-V

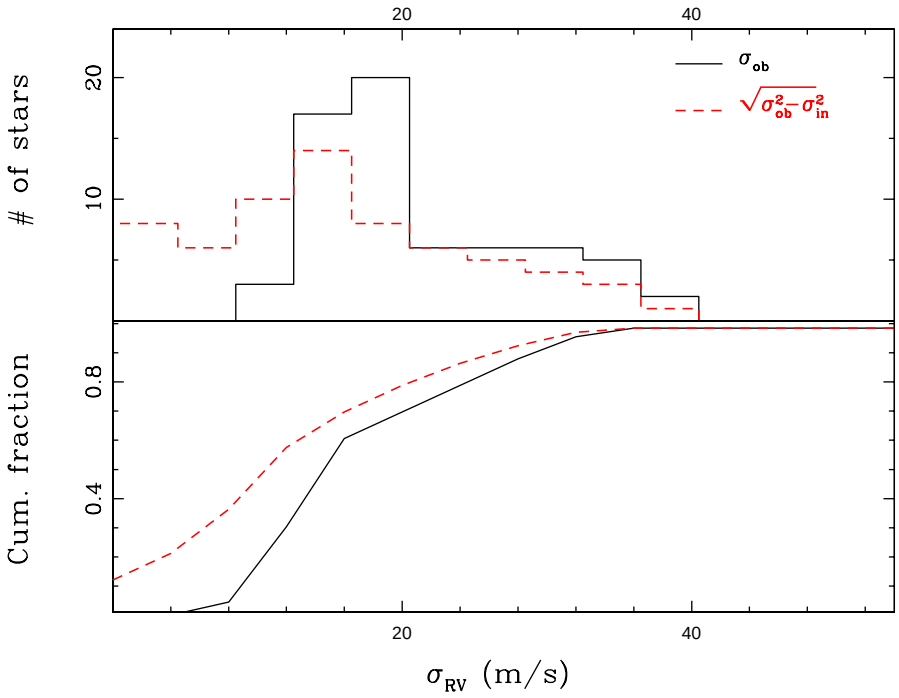

Figure 3.4: Upper panel: Histogram of the observed standard deviation in the RV variations computed for our CTIO sample (black solid line). The same is also shown but this time the intrumental error (mean error bar for each star dataset) is substracted in quadrature (red dashed line). Lower panel: Cumulative fraction for both distributions shown in the upper panel plot.

color less than 1.2 present a level of jitter below 20 $\mathrm{m\,s^{-1}}$ (in fact we used this cut in the color selection of our targets), which allows us to detect giant planets orbiting them as they produce RV amplitudes of several tens of $\mathrm{m\,s^{-1}}$. In order to investigate the level of variability of our CTIO targets we computed the RV standard deviation for all of them.

Since there are three binary stars in our sample (HIP76532, HIP75569 and HIP104148) we fit a keplerian orbit, and then we computed the standard deviation from the residuals of the fit. We applied an equivalent procedure for the three stars showing a long linear trend (HIP7118, HIP22479 and HIP103836). The results are plotted in Figure 3.4. In the upper panel we show a histogram of the observed standard deviation (black solid line). In addition, we computed the standard deviation of the data, but this time we substracted in quadrature the mean instrumental error for each star dataset (dashed red line), which is more representative of

the intrinsic stellar variability.

In the lower panel we show the corresponding cumulative distribution functions. As can be seen, the red dashed line shows that around half of the stars have an intrinsic variability below 10 $\mathrm{m\,s^{-1}}$ and $\sim 75\%$ of them below 20 $\mathrm{m\,s^{-1}}$. There is also one star that show a variability of $\sim$ 100 $\mathrm{m\,s^{-1}}$, which is out of the plot scale. This result is in agreement with Setiawan et al. (2004) and Hekker et al. (2006) even though we obtain a larger fraction of stable stars ($\sigma \lesssim 20\ \mathrm{m\,s^{-1}}$) in our sample. This difference can be explained by the fact that we put an upper cut in the luminosity for our stars (just a few of them are more luminous than $100\,L_{\odot}$) and since the more luminous stars have also larger radii, which are expected to present larger oscillation amplitudes, we don't observe RV variabilities exceeding $\sim 50\ \mathrm{m\,s^{-1}}$, except for HIP105854. We also put a cut in the photometric variability from Hippracos data, in order to include the most stable giant stars.

3.5.2 Are there any close-in planets?

In the presence of a massive enough companion, the RV curve of a star shows a large and periodic variation, from which the orbital parameters can be determined. On the other hand, in the presence of a lower mass companion, no clear periodic variation will be observed, especially when the stellar jitter and instrumental error are comparable to the induced velocity amplitude, making the analysis of the RV curve more complicated. However, in this case the dispersion of the RV datapoints provides important information, which can be used to discard the presence of a planet in a given region of the orbital parameter space. Let's then define the observed weighted standard deviation (σ_{obs}) by:

$$\sigma_{obs}^2 = \sum_{i=1}^{n} \omega_i \,(v_i - \bar{v})^2 \tag{3.5}$$

where v_i is the measured RV at the i-th epoch and $\bar{v}$ is the weighted mean velocity, given by $\sum \omega_i\, v_i$. The normalized statistical weight ω_i correspond simply to A/σ_i^2, where

σ_i is the measurement error derived from the velocity dispersion of all the chunks, at the i-th epoch. This weighting scheme helps to assign a low weight to RV points having a large instrumental error, which usually depart from the mean velocity. For the three binary stars and the three stars with a long period linear trend, we computed σ_{obs} from the residuals of the best keplerian fits. Additionally, in a few cases, we rejected one RV datapoint that significantly departs from the mean velocity. The measured σ_{obs} for a given star arises from three different sources, namely the instrumental error (σ_{ins}), the doppler shift induced by a substellar companion (σ_p) and the stellar jitter (σ_{st}). The first term is simply the dispersion in the individual chunk velocities, as mentioned above, and the second one (in the presence of a planet) depends on the stellar mass, planetary mass, eccentricity, orbital distance, and time coverage. The third term, which is related to intrisic stellar phenomena, is typically below 20 $\mathrm{m\,s^{-1}}$ (see § 5.1). For each stellar dataset we computed the time of the observations and the correponding instrumental errors in a Monte-Carlo fashion, employing a total of $\sim$1000 simulations and including the three terms just described. The instrumental errors and stellar jitter were assumed to follow a gaussian distribution, with mean value equal to σ_i (see equation 3.5) and 10 $\mathrm{m\,s^{-1}}$, respectively. Finally σ_p was computed varying the orbital distance between 0.05 and 0.6 AU, the eccentricity between 0 and 0.5 and ω (argument of periastron) between 0 and $\pi/2$. The mass of the planet was fixed to $1\,\mathrm{M}_J$ and the mass of the host star was retrieved from Jones et al. (2011). For each synthetic dataset we measured the weighted standard deviation, as defined in equation 3.5 (hereafter refered as σ_{sim}). We then computed the fraction of simulations leading to $\sigma_{obs} < \sigma_{sim}$ (f_{sim}).

Let us consider a star, for which f_{sim} is close to 1. In this case we can rule out the presence of a giant planet (at a confidence level given by the f_{sim}), because on the contrary the σ_p term would be large enough so that $\sigma_{obs} > \sigma_{sim}$. Let's now consider the opposite situation, i.e., that a significant fraction of the simulations lead to $\sigma_{obs} < \sigma_{sim}$ (i.e. f_{sim} close to zero). In this case the interpretation is more difficut since there are different possibilities that could explain the observed variability. The first possibility is that the stellar jitter is considerably

higher than 10 $\mathrm{m\,s^{-1}}$ and hence σ_{st} will be the most important contribution to σ_{obs}. The second possibility is that a massive enough planet (or a planetary system) is orbiting the star, inducing a doppler shift variability in time that will be the dominant term contributing to σ_{obs}. In this case, if a periodic variability is observed, a further follow up is needed to actually confirm (or discard) the presence of a companion. The third possibility is a combination of both stellar jitter plus an orbiting planet.

From the MC simulations we found that for half of the stars $f_{sim} > 0.97$ and for 75% of them $f_{sim} > 0.86$. This result is interpreted as the majority of the stars show a RV variability that is consistent with a stellar jitter at the 10 $\mathrm{m\,s^{-1}}$ level and no giant planet. However, as can be expected from Figure 3.4, there is a fraction of our targets that show a higher level of variability that might be due to either a planetary signal and/or enhanced stellar jitter. Since σ_{obs} cannot be used to discriminate between stellar activity and/or a planetary signal, for every target showing $f_{sim} < 0.97$ we computed a Lomb-Scargle periodogram, in order to search for periodical signals in the range between $\sim$25 days (corresponding to around 4 times the Nyquist frequency in our data) and periods corresponding to the orbital distance of 0.6 AU ($\sim$170 days for a planet orbiting in a circular orbit around a 1.0 $M_{\odot}$ star). We didn't find any significant peak in the periodograms, meaning that we can discard the presence of giant planets in close-in orbits in our CTIO sample. This result, reinforces the previous claims (e.g. Sato el at. 2008; Dollinger et al. 2009) of the absence of planets orbiting within 0,6 AU around clump giants.

3.5.3 Long period companions

As already mentioned in the previous sections, we found significant RV signals with periods exceeding several hundreds of days. Firstly, there are three stars (HIP76532, HIP75569 and HIP104148) that present a RV variation of a few $\mathrm{km\,s^{-1}}$, which are clearly due to the presence of a stellar companion (see Figures 3.10 and 3.12). HIP7118 and HIP22479 show a long linear trend with peak to peak variations of several hundreds $\mathrm{m\,s^{-1}}$. In the latter case, there are 9

HARPS observations that confirm the linear trend, which extends over $\sim$2000 days. In both cases the RV curves can be explained either by a brown dwarf orbiting at several AU's or by a stellar companion in a very wide orbit. A similar trend is also exhibited by HIP103836, but this time the peak to peak variation is $\sim$ 200 $\mathrm{m\,s^{-1}}$, in a timespan of over 800 days. Finally, there are several smaller amplitude signals that might be due to the presence of planets orbiting beyond 0.6 AU, but the peak in the periodograms are not that strong. More data are needed to confirm these lower signal amplitudes in the data.

3.5.4 Observations of 81 Cet

During the past few years, we have observed the giant star 81 Cet, which is known to host a giant planet (Sato et al. 2008). The RV curve of this object is shown in Figure 3.5. The red solid dots correspond to the publish data while the blue open circles are our data. The best keplerian fit, which is computed including both datasets, is overplotted with a solid black line. Our observations confirm the periodic RV signal published for this star, but we obtain a larger scatter, that is in part due to our larger uncertainties. However our data show a much steeper RV variation, and a keplerian fit to our data leads to a lower eccentricity and a longer orbital period. We speculate that this star might be experiencing a higher activity cicle, or even more, the periodic signal might be due to spots on the stellar surface. However, the latter hypothesis is unlikely, since the typical rotational period for these type of stars is a few hundreds of days, much shorter than the observed RV period ($\sim$1000 days), unless we are witnessing an unfortunate mixture of spot group rotation that is beating with our sampling epochs.

3.6 Summary and conclusions

In this paper we report the first results of our RV survey aimed at studying the population of giant planets orbiting within the inner 0.6 AU's from the host star. We have applied the I_2 cell technique in order to obtain precise RV's for a sample of 66 giant stars. We

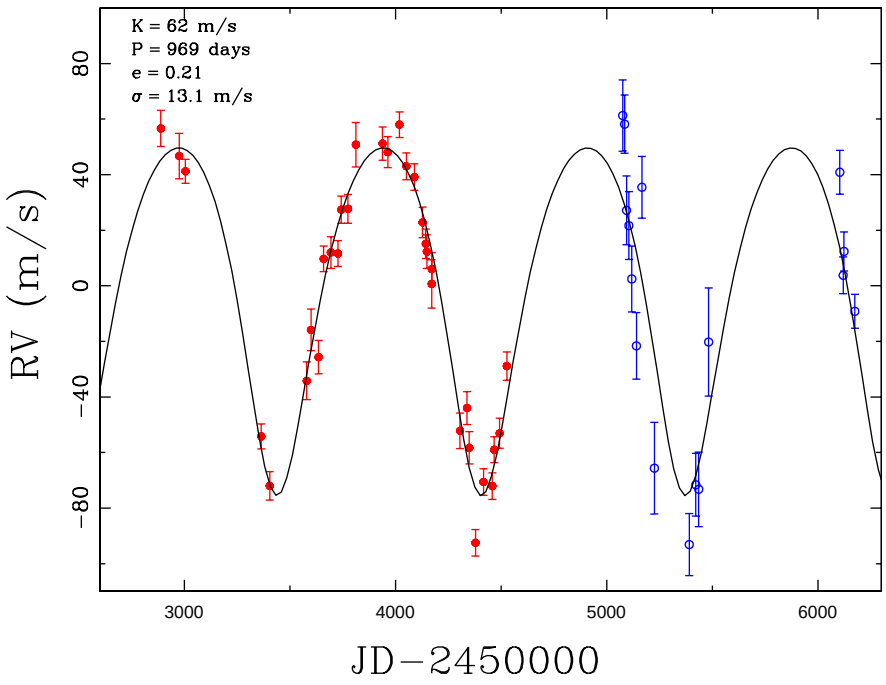

Figure 3.5: Radial velocity curve of 81 Cet. The red dots and blue open circles correspond to Sato et el. (2008) and our data, respectively. The black solid line correspond to the best keplerian fit using both datasets. The new derived orbital parameters are also labelled.

also used a strong statistical procedure in order to improve the precision of the radial velocities. We investigated the variability of our targets and we have shown that > 75 % of them are more stable than 20 m s^{-1} and around 50% have intrinsic variability below 10 m s^{-1} .

We performed a detailed analysis of the RV variability computed for each target and we searched for significant periodicities up to $\sim$ 160 days, in order to put some constraints on the population of giant planets in close-in orbits. We showed that based on the RV standard deviation, half of the targets show no indication of any giant planet orbiting within 0.6 AU's (at the 97 % confidence level). For the rest of the targets we also searched for significant periodic signals using a LS periodogram. We didn't obtain a significant peak for any of the targets, meaning that we can discard the presence of giant planets orbiting close to the host star, in our CTIO sample. This result confirms the lack of short period planets already claimed by other groups (e.g. Sato et al. 2005; Dollinger et al. 2009; Niedzielski et al. 2009).

In addition, we found 3 stars that exhibit RV variation of a few $\mathrm{km\,s^{-1}}$, and two other stars that exhibit RV variations of several hundreds of $\mathrm{m\,s^{-1}}$, which are likely to be in binary systems. This result confirms that there is a significant fraction of giant stars in binary systems, especially considering that we selected stars that were not identified to have a stellar companion (and therefore the actual fraction should be much larger).

Finally, we obtained 15 observations of 81 Cet, which is a clump giant known to host a substellar companion. We confirmed the periodic RV signal published by Sato et al. (2008), but we found a different slope in the RV curve, which cannot be explained solely by our larger error bars. This might be an indication that the star is experiencing a higher activity cicle, so that the RV curve is significantly affected. More data are needed to confirm this hypothesis.

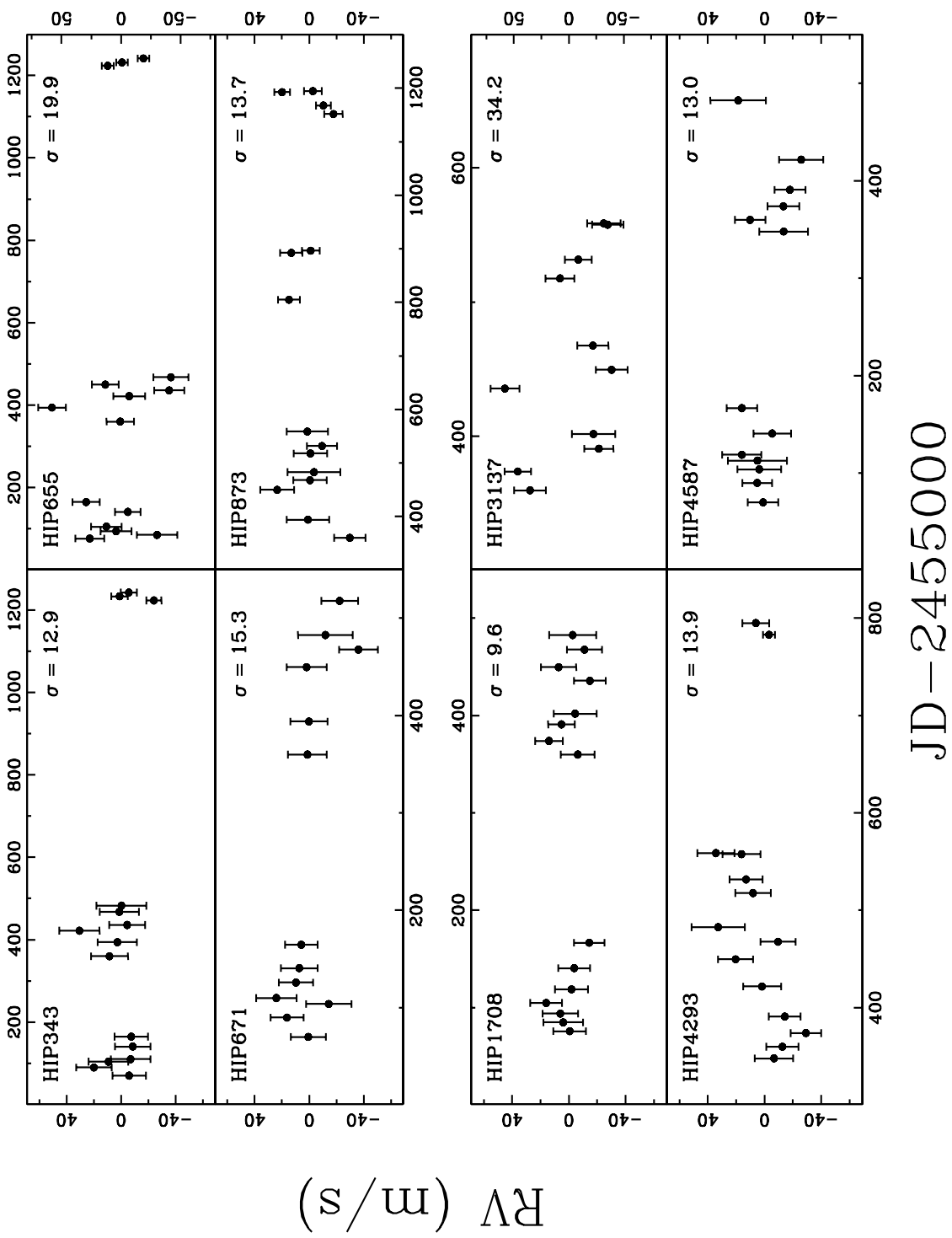

Figure 3.6: Radial velocity variations for 8 of our targets. The name of the star and the observed weighted standard deviations are labelled.

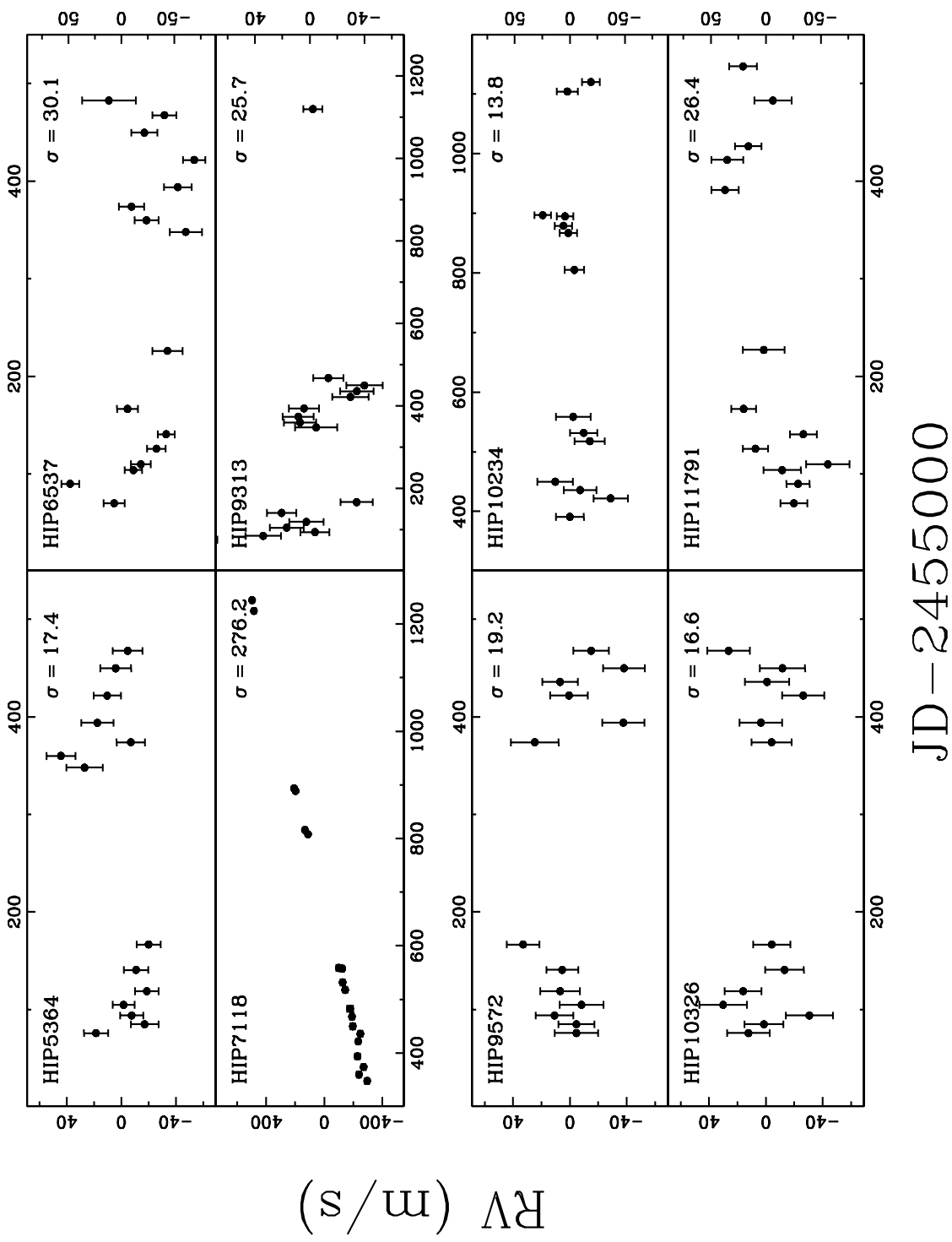

Figure 3.7: Same as Figure 3.6

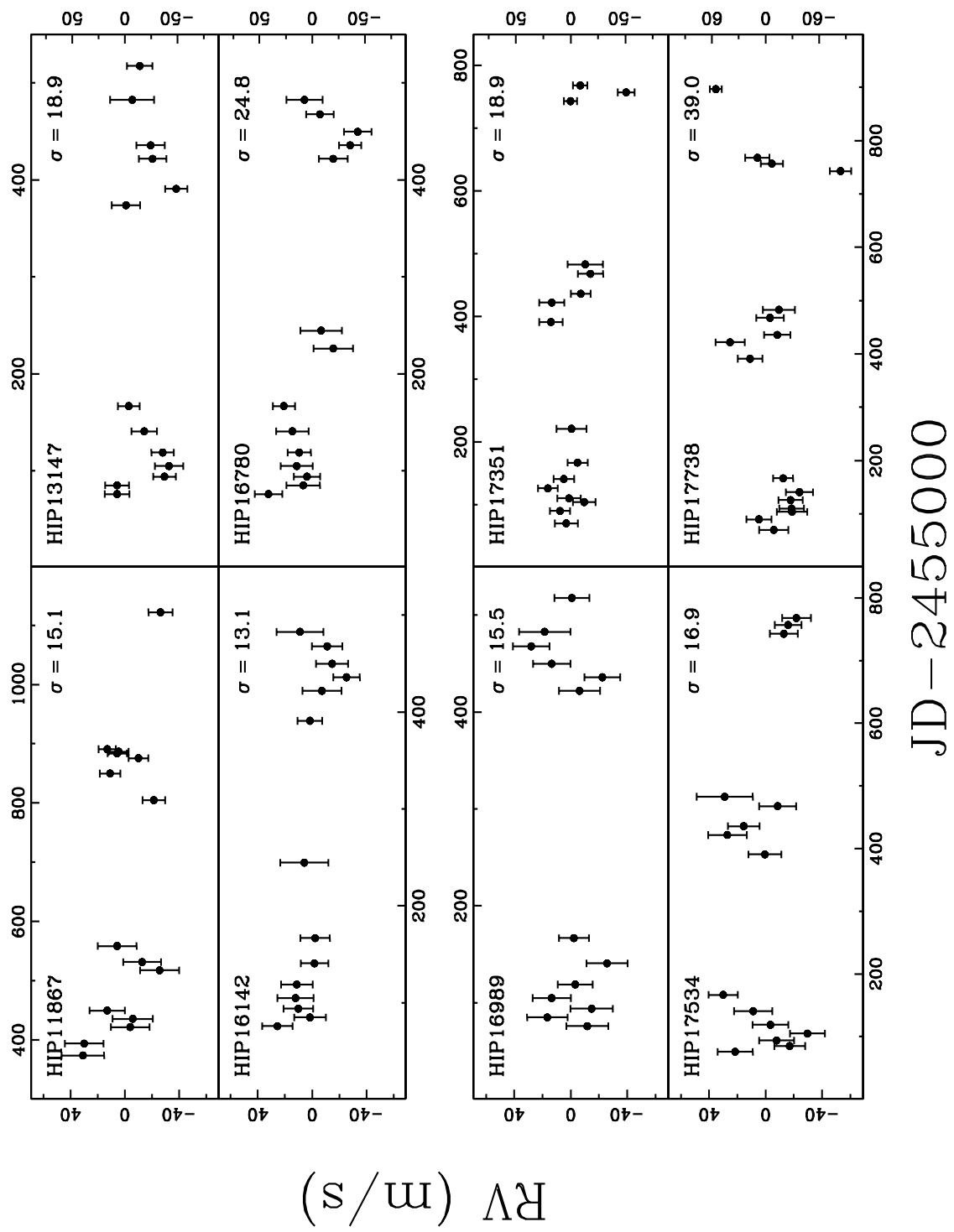

Figure 3.8: Same as Figure 3.6

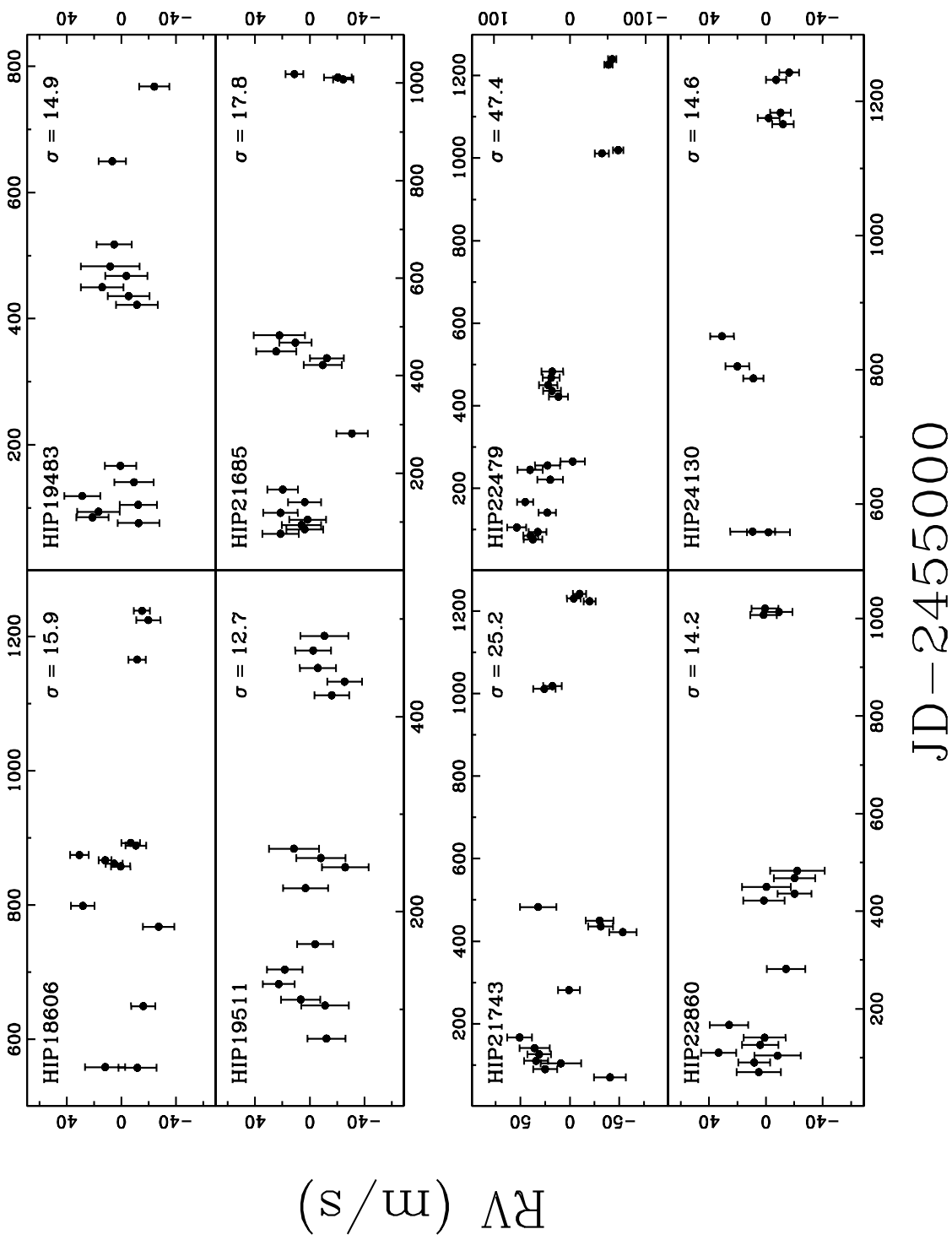

Figure 3.9: Same as Figure 3.6

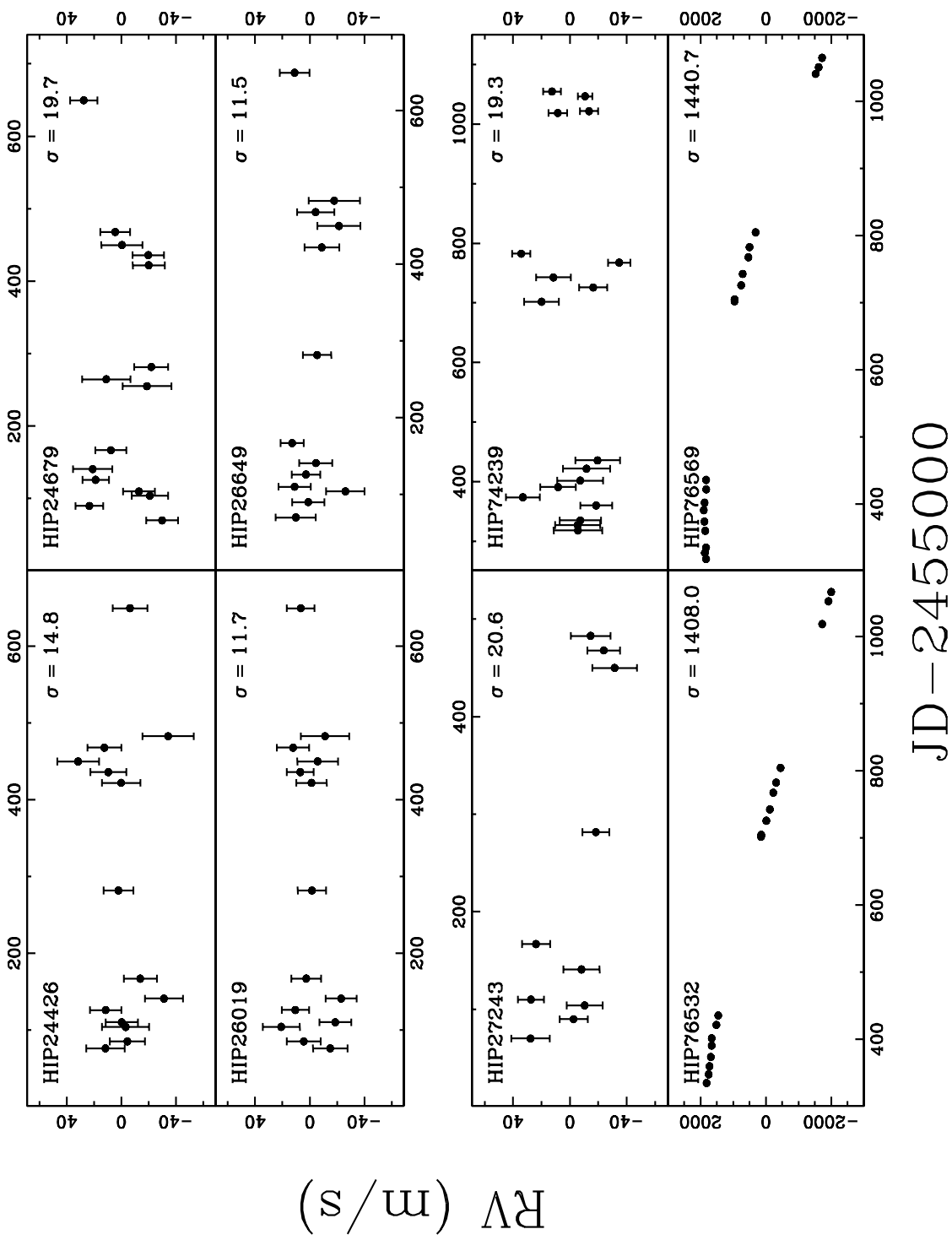

Figure 3.10: Same as Figure 3.6

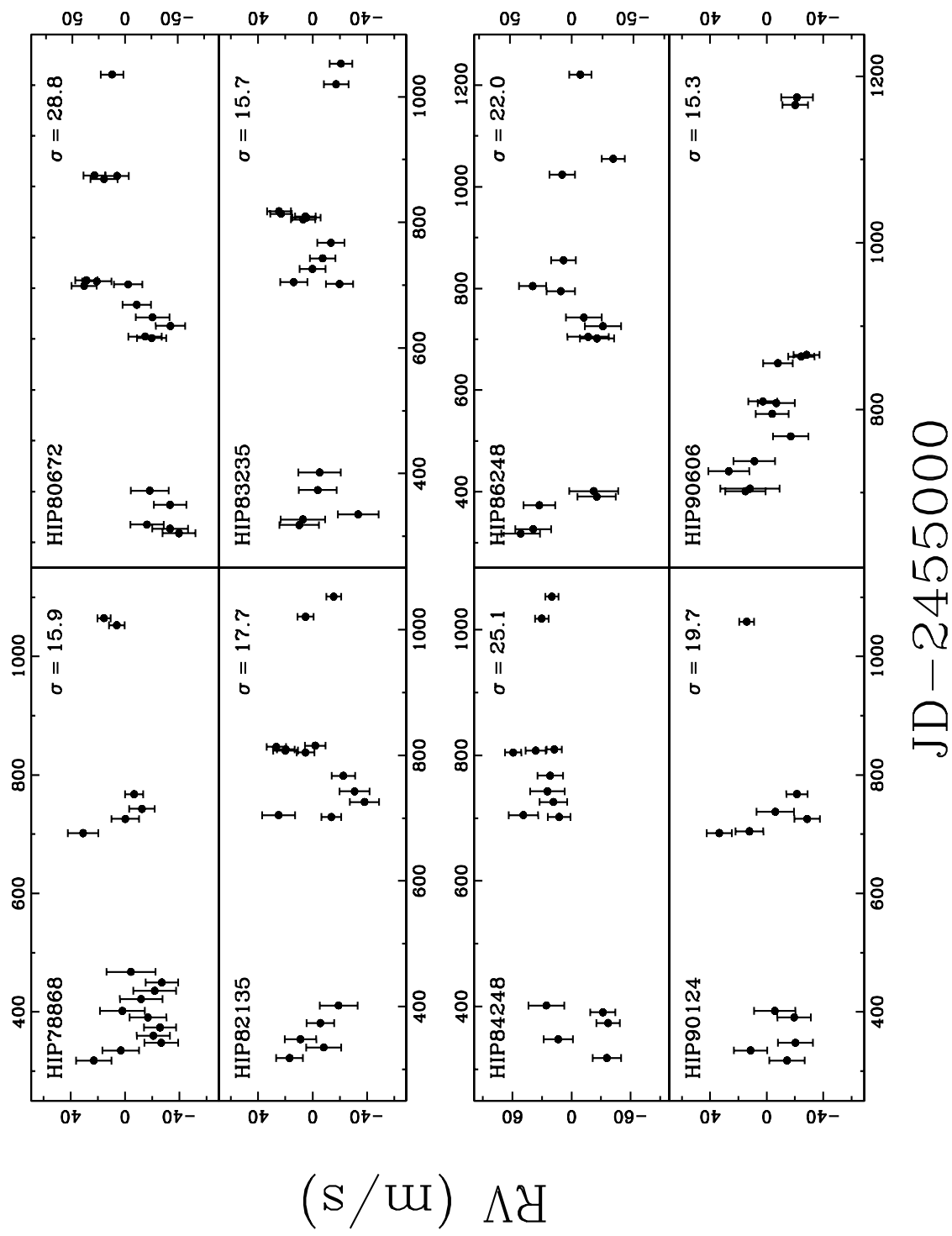

Figure 3.11: Same as Figure 3.6

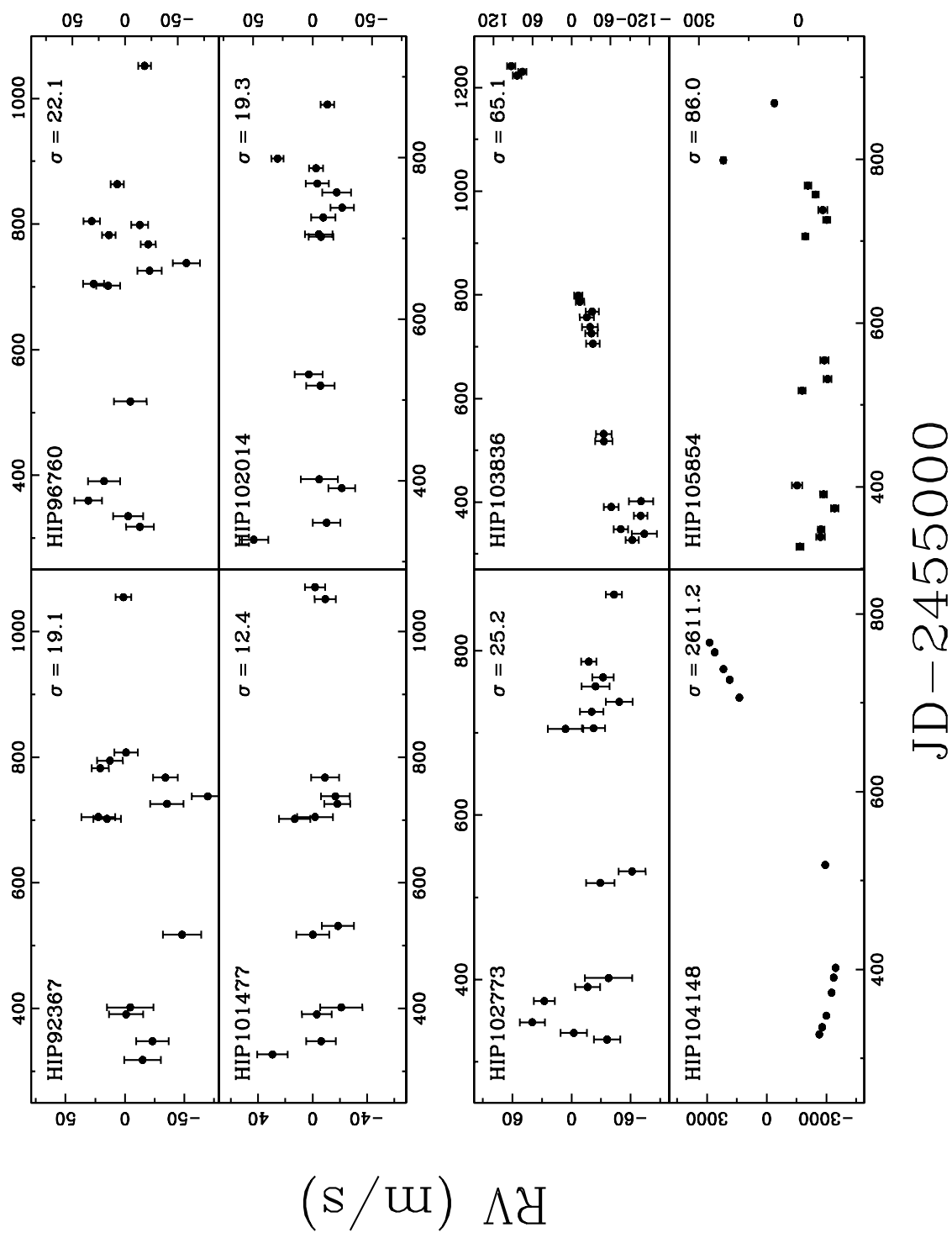

Figure 3.12: Same as Figure 3.6

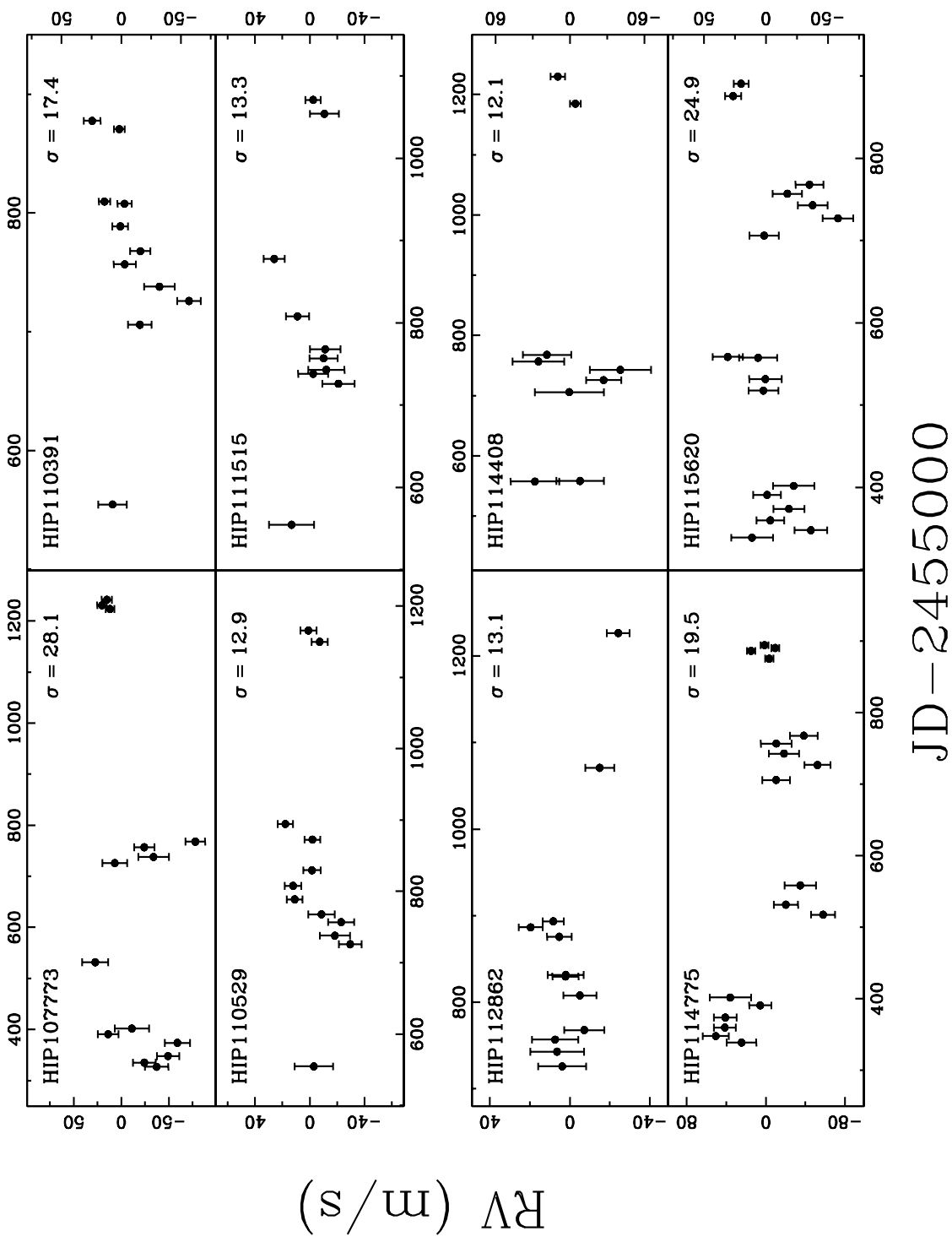

Figure 3.13: Same as Figure 3.6

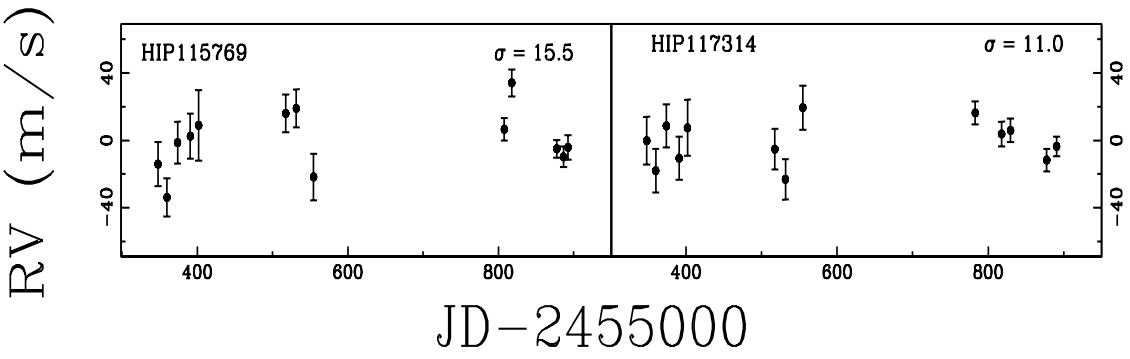

Figure 3.14: Same as Figure 3.6

Chapter 4

Radial Velocities From the FEROS Sample

4.1 Data Reduction

The data reduction of all of the spectra taken with FEROS was done with the ESO reduction pipeline, which is available for FEROS users. The reduction pipeline performs a bias substraction, flat fielding, orders tracing and extraction. In addition, the scattered light is substracted. Since FEROS uses a fiber slicer, the order extraction is done after adding up all of the light from the pixels along the width of the fiber instead of applying an optimum extraction (i.e. fitting a gaussian perpendicular to the dispersion direction). A wavelength calibration is computed using several Thorium-Argon calibration lamps having different exposure times and instensities, which allow to cover all of the spectral range ($\sim$ 3500-9200 Å). The typical rms in the wavelength solution is $\sim$ 0.005 Å. Finally, the wavelength calibration is applied to the observed spectra, which are extracted order by order. Additionally, the reduction pipeline applies a barycentric correction to the extracted spectra, but this option was disabled because it retrieves the coordinates of the star that are recorded in the header, which are not accurate enough. Instead, this correction was computed separately, and then is applied to the reduced data, as is discussed in the next section.

4.2 Radial Velocity Computation

The RV's for each individual spectrum were measured in the following manner. Firstly, the doppler shift was computed by applying a Cross Correlation (Tonry & Davis 1979) between the stellar spectrum and its corresponding template (high S/N spectrum of the same star). This method was repeated to $\sim$ 50 Å chunks (corresponding to $\sim$ 2000 pixels), leading to a total of $\sim$ 140 different RV's per observation. The IRAF task RV/fxcor (Fitzpatrick 1993) was used, applying a fourier filter to both, the observation and the stellar template. The fourier filter is used to cut every frequency below and above a given value, which help to improve in few $\mathrm{m\,s^{-1}}$ the error bars (especially for low S/N spectra). The low frequency cut is intended to remove periodic patterns that are correlated with the position in the CCD, whereas the high frequency cut allows to remove periodic signals that are related to noise in the data. Then, for each dataset, the mean velocity was derived, rejecting in an iterative way every point lying away from 2.5 sigma, which typically correspond to 20 % of them. It is worth mentioning that since all of the orders were included, cutting only 100 pixels at the edges, many chunks lead to very deviating velocities mainly either due to low S/N (especially toward the blue) or because of the presence of telluric lines (in the red part of the spectrum). Figure 4.1 shows the chunk velocities from one spectrum of Tau Ceti. The black dots are the non-deviant velocities and the red crosses are those rejected by the procedure just described (some of them are out of scale). The standard deviation of the chunk velocities is 60.7 $\mathrm{m\,s^{-1}}$, which correspond to an error in the mean[1] of just 5.1 $\mathrm{m\,s^{-1}}$.

The second step consists on a similar procedure, but this the cross correlation is computed between the simultaneous calibration lamp (sky fiber) and one of the lamps that was used for the wavelength calibration of that night (i.e., corresponding to the night zero point), having a similar exposure time of the simultaneous calibration lamp. This procedure is neccessary to substract the nighlty drift, produced mainly by small variations in the refraction index in

[1]The error in the mean is given by: $\sigma/\sqrt{n_c}$, where σ is the standard deviation of the chunks velocities and
n_c is the number of non-rejected chunks used in the analysis

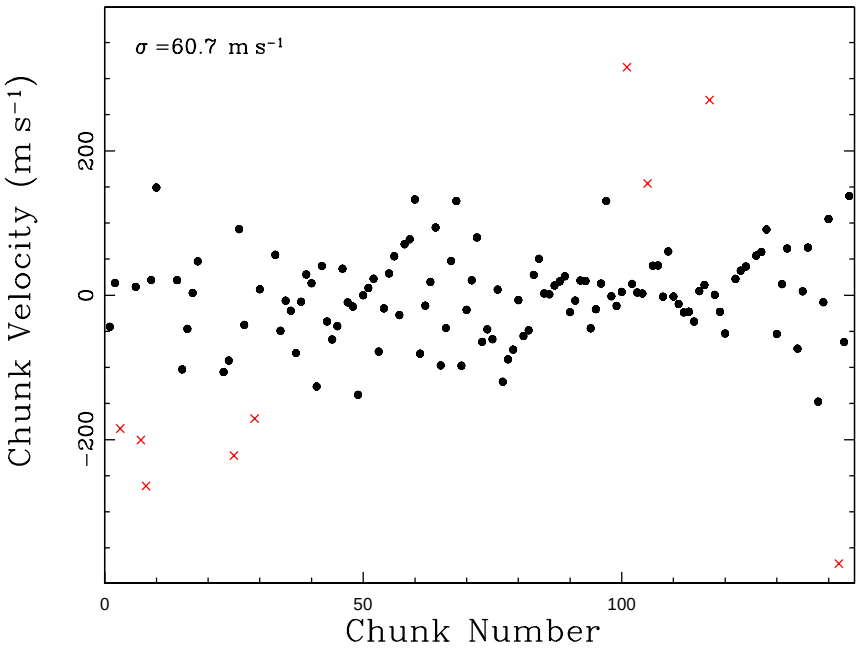

Figure 4.1: Radial velocities computed from $\sim$ 140 different chunks, from a single observation of Tau Ceti. The solid black dots are the chunks velocities, while the red crosses correspond to the rejected velocities. The standard deviation is 60.7 $\mathrm{m\,s^{-1}}$, corresponding to an error in the mean velocity of $\sim$ 5.1 $\mathrm{m\,s^{-1}}$.

the spectrograph during the night, which at first order translates into a linear RV shift as large as $\sim$ 150 $\mathrm{m\,s^{-1}}$. It is worth to mention that no second order correction was applied, like the RV shift between the two fibers, which is typically $\sim$ 2 $\mathrm{m\,s^{-1}}$ (Setiawan et al. 2000). Finally, the radial velocity for each epoch is computed by:

$$\mathrm{RV}\,(Obj\,,\,Temp) + \mathrm{RV}\,(SimCal\,,\,WavCal) + \mathrm{BC} \tag{4.1}$$

where the first and second terms correspond to the RV computed for the object with its corresponding template and to the nightly drift, as explained above. The third term corresponds to the barycentric correction, which is computed using the middle time of the observation and using the actual coordinates of the star at that time, which are slightly different to the ones recorded in the image header (typically up to $\sim$ 1-2 arcminutes). This

is quite important, since the error in the header coordinates translates into a RV uncertainty as big as $\sim$ 5-10 $\mathrm{m\,s^{-1}}$. Figure 4.2 shows the RV's computed from 25 spectra of Tau Ceti,

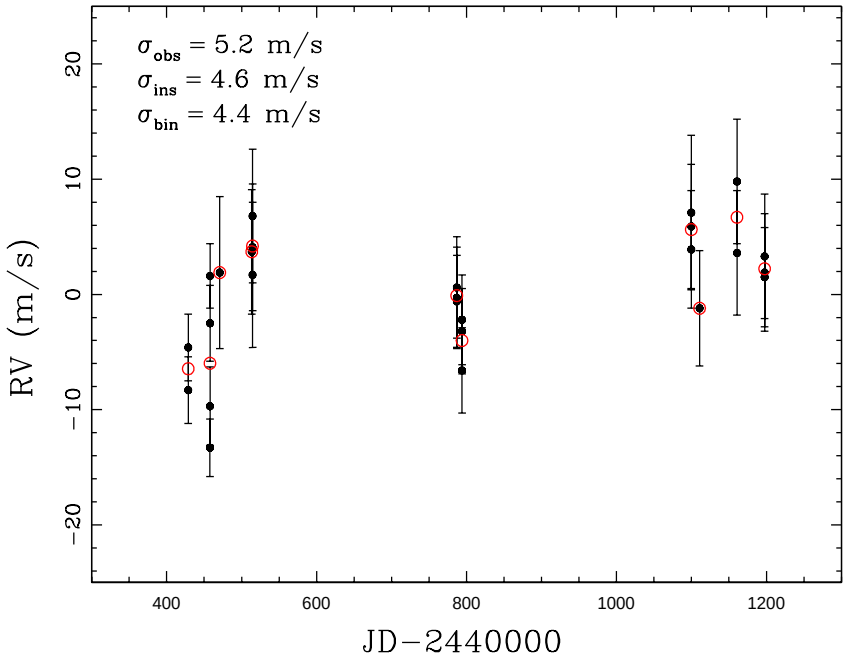

Figure 4.2: Three years observations of the RV standard star Tau Ceti. The mean instrumental error is 4.6 $\mathrm{m\,s^{-1}}$, and the standard deviation is 5.2 $\mathrm{m\,s^{-1}}$. The binned RV's lead to a dispersion of only 4.4 $\mathrm{m\,s^{-1}}$.

taken during the last three years. This star is known to be stable at the $\sim$1 $\mathrm{m\,s^{-1}}$ level (see Pepe et al. 2011) and therefore it is a very appropiate target to test the long-term precision of FEROS. The error bars are computed from the error in the mean of the chunk velocities. The measured standard deviation is only 5.2 $\mathrm{m\,s^{-1}}$ and the mean intrumental error is 4.6 $\mathrm{m\,s^{-1}}$. Additionally, since the typical exposure time of the observations is 20 seconds, the RV's from consecutives observations during the same night were binned in order to average the main stellar oscillation modes, having typical timescales of $\sim$ 5 minutes in these kind of stars. The binned RV's are overplotted in Figure 4.2 (open red circles). This time the standard deviation drops down to just 4.4 $\mathrm{m\,s^{-1}}$, which is consistent with the intrumental errors. Hence, it can be claimed that the long-term RV precision of FEROS is $\sim$ 4 $\mathrm{m\,s^{-1}}$. This result is important since puts FEROS well into the high precision instruments that

are suited for RV surveys aimed at detecting lower mass planets. Actually, this precision is comparable to the one that can be achieved by other instruments that have been developed mainly for planet searches (e.g. CORALIE at the Swiss telescope on La Silla).

4.3 Preliminary Results

During the last three years, multi-epoch FEROS observations for a sample of more than 100 stars were collected ($\sim$ 20 of them in common with the CTIO sample). Some interesting results have emerged from this rich dataset, which are highlighted in the following sections.

4.3.1 Binary Systems

From the FEROS sample, 20 stars show a RV variation of hundreds to thousands $\mathrm{m\,s^{-1}}$, which are likely explained by the presence of a stellar companion. Figures 4.3 and 4.4 show some examples. In most cases, the error bars are smaller than the symbol sizes. It can be

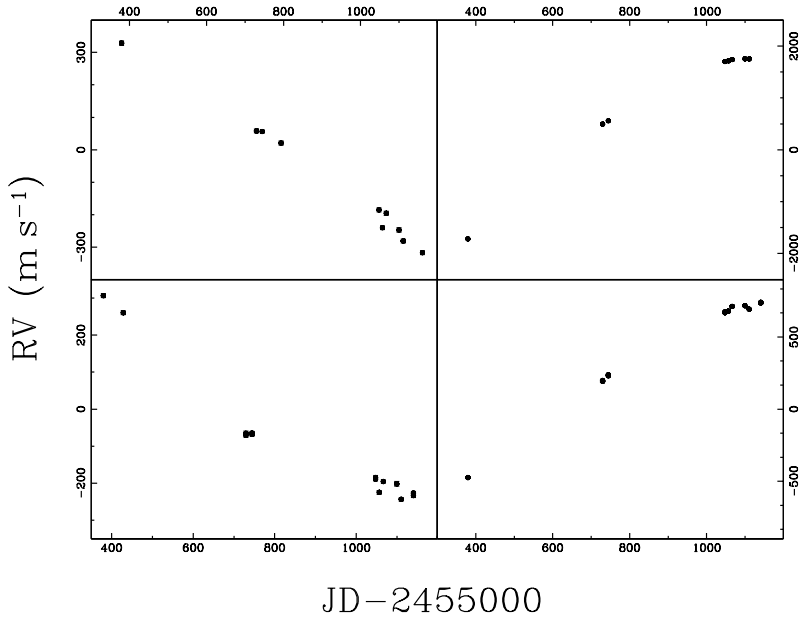

Figure 4.3: Four binary system discovered among the FEROS sample. The error bars are smaller than the symbol size.

be noticed that only in one case it is possible to constraint the orbital distance and hence the mass of the secondary (left upper panel in Figure 4.4). For the rest of them, the time coverage is not long enough to determine the orbital parameters. More observations for these objects will be taken in the future in order to fully derive the orbital parameters. In

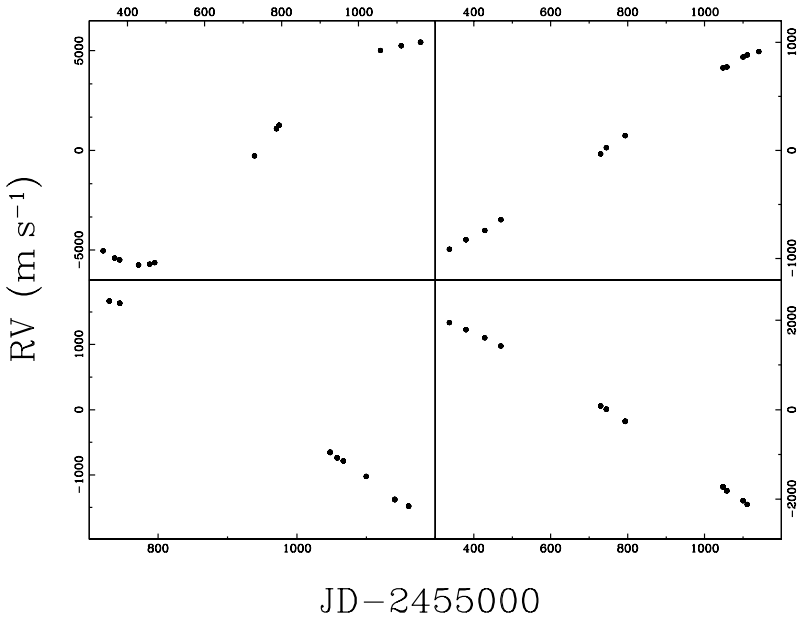

Figure 4.4: Same as Figure 4.3.

addition, there are two very interesting binary systems, both of them compounded by a first ascending red giant branch star and companion having a minimum mass corresponding to a M dwarf. In the first case, the primary star (HIP73758) has a mass of 1.4 $M_{\odot}$ and the best keplerian fit leads to an orbital distance of $a = 0.5$ AU (corresponding to P = 97 days) and an eccentricity of 0.44. This is a pre-common envelope system. In fact, according to single stellar evolution models, in $\sim 10^8$ yr, the radius of the primary star will be comparable in size to the separation between both stars. In the second case (HIP83224) the primary star is an intermediate-mass star (1.75 $M_{\odot}$) and the orbital period of the system is 173 days with an eccentricity of 0.31. The RV curves for them are plotted in Figure 4.5. The best keplerian fits are overplotted (solid black lines).

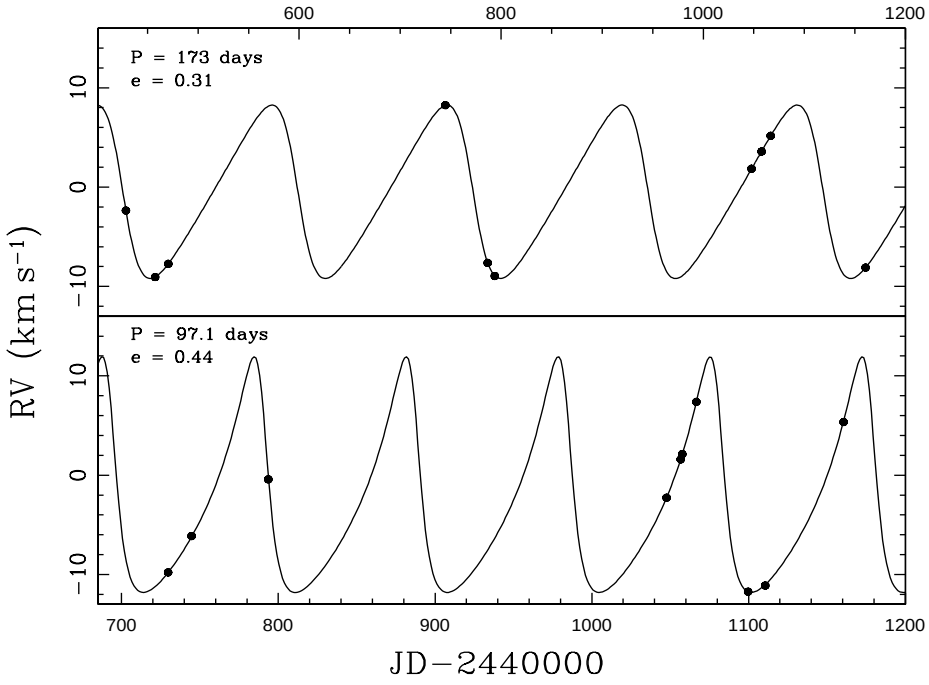

Figure 4.5: RV curves for HIP83224 (upper panel) and HIP73758 (lower panel). The best keplerian fits are overplotted (black solid line). The orbital periods and eccentricities are also labelled.

4.3.2 HIP63242b: the closest planet around and intermediate-mass giant star

According to the *Hipparcos* catalogue, HIP63242 is a G8III star with V=6.87, B-V=1.03 and a parallax of π=7.42 $\pm$ 0.49, which correspond to a distance of 135 pc. The atmospheric parameters for this star were computed in Jones et al. (2011) and are listed in Table 4.1. Comparing these parameters, with Salasnich et al. (2000) evolutionary models, they derived a mass of 1.54 $M_{\odot}$ for this object. In Figure 4.6 is also plotted the position of HIP63242 in the HR diagram and the closest evolutionary models from Salasnich et al. (2000). This star is clearly ascending the RGB, since no HB model cross its position in the HR diagram.

During the last three years, 12 spectra (including the template) for this object were obtained using FEROS. Its RV curve is shown in Figure 4.7. The typical error bars are $\sim$5 m s^{-1}, therefore are smaller than the symbol sizes. The best keplerian fit [2] is overplotted

[2]The keplerian solution was computed using the *Systemic Console* (Meschiari et al. 2009)

Table 4.1: Stellar properties of HIP63242

Parameter	Value
B-V (mag)	1.02 ± 0.02
V (mag)	6.86 ± 0.01
π (mas)	7.42 ± 0.49
T_{eff}(K)	4830 ± 100
$\log g$ (cm s^{-2})	2.53 ± 0.2
[Fe/H]	-0.31 ± 0.09
L ($L_{\odot}$)	42.7 ± 0.08
Mass ($M_{\odot}$)	1.54 ± 0.05
v sin$i$ (km s^{-1})	3.7 ± 0.1

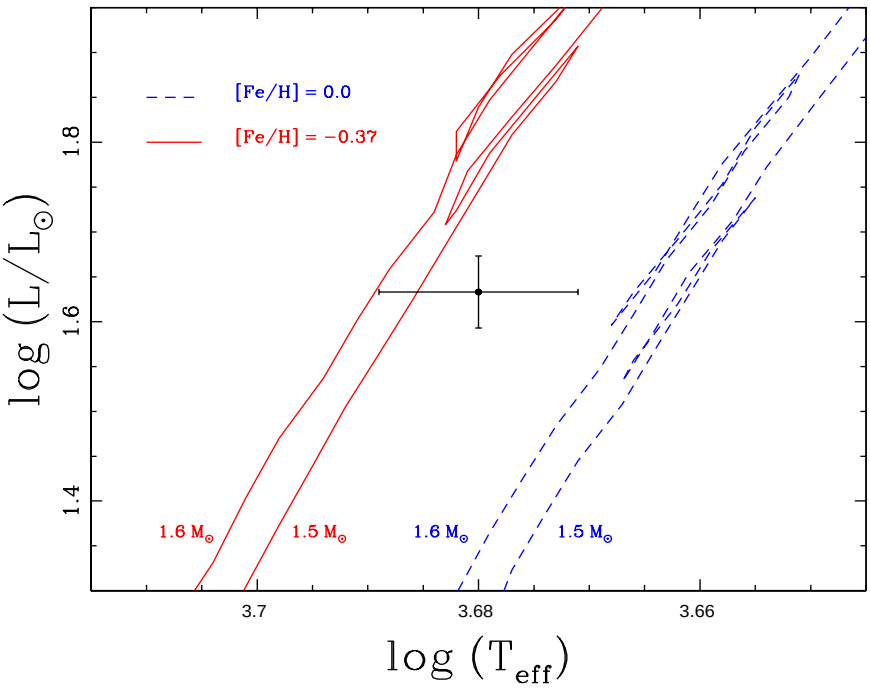

Figure 4.6: Position of HIP63242 in the HR diagram. The four closest evolutionary tracks from Salasnich et al. (2000) are overplotted.

Table 4.2: Orbital parameters for HIP63242 b

Parameter	Value
P (days)	125.2
K ($\mathrm{m\,s^{-1}}$)	304.2
a (AU)	0.57
e	0.23
ω (deg)	110.8
$\mathrm{T_0}$ (JD)	2455355.8
$\mathrm{M_p} \sin i$ ($\mathrm{M_J}$)	9.7

(solid black curve). It can be noticed that there is a strong RV signal present in the data. The orbital parameters of the planet are listed in Table 4.2.

4.3.2.1 Photometric and Line Profile Analysis

In order to determine the actual nature of the large periodic signal observed in the HIP63242 radial velocities, two standard tests were applied to detect stellar phenomena that might be afecting the RV curve, such as rotational modulation or stellar oscillations. The first test consists in a photometric analysis, aimed at detecting variations in the brightness of the star due to the presence of spots in its surface, that might be mimicing a doppler shift induced by a substellar companion (e.g. Figueira et al. 2010). For this purpose, the *Hipparcos* photometric data were analyzed, which consists of a total of 142 H_p filter observations, taken between JD 2447869 and 2449013. The photometric data show a small dispersion of 0.009 mag, which certainly cannot be responsible for the observed large RV variations. In fact, according Hatzes (2002), a spot covering 5 % of the stellar surface (corresponding to a decrease of ~ 0.06 mag in the flux if the spot is completely opaque) will induce a RV variation below $100\,\mathrm{m\,s^{-1}}$, on a star having a projected rotational velocity similar to HIP63242 (v_{rot} = 3.6 $\mathrm{k\,m\,s^{-1}}$). Also, no significant periodic signal is observed in the *Hipparcos* photome-

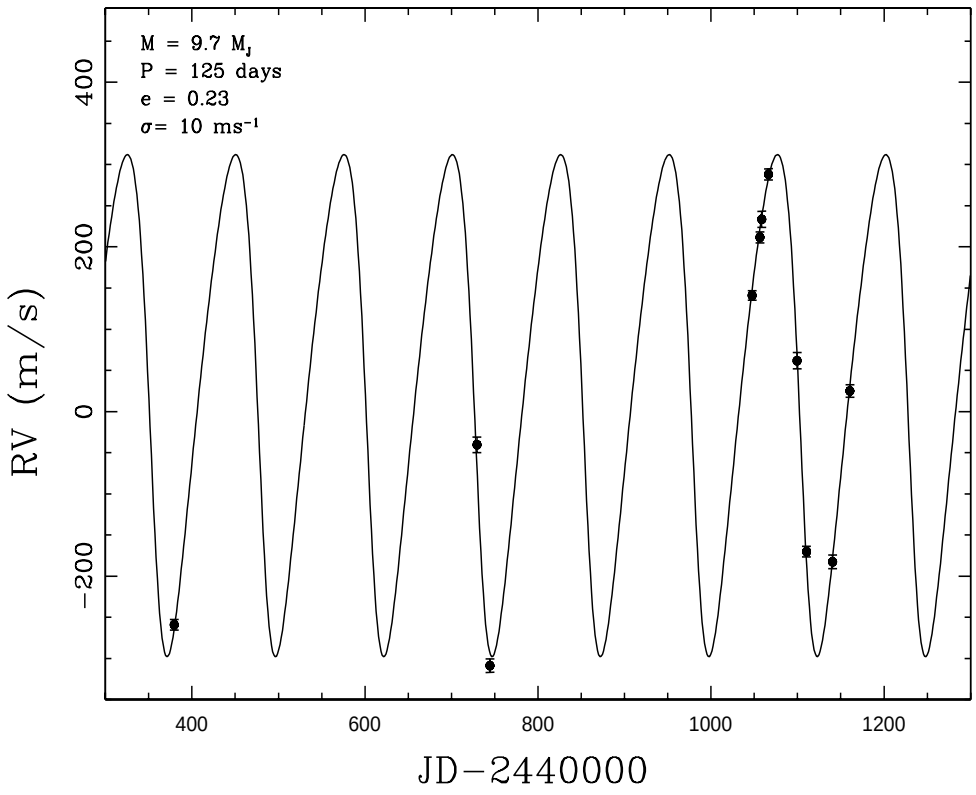

Figure 4.7: RV curve for HIP63242 (black dots). The best keplerian fit is overplotted (black solid line). The orbital parameters are labelled.

try. Hence, rotational modulation can be discarded as the responsible mechanism for the observed RV signal. The second test corresponds to the bisector analysis (Toner & Gray 1988), aimed at detecting assymetries in the line profiles due to oscillations in the outer part of the star. Figure 4.8 shows the bisector velocity span, which corresponds to the velocity difference between the bottom and the top of the CCF, versus the measured radial velocities of HIP63242. The error bars in the bisector velocities were derived simply as the error in the mean from 5 sets of indepedent bisector velocities, computed from the CCF from 5 different orders. Clearly no obvious correlation between both quantities is present, which supports the planetary origin of the RV curve.

The discovery of this planet is very important for two main reasons: 1) this is the first

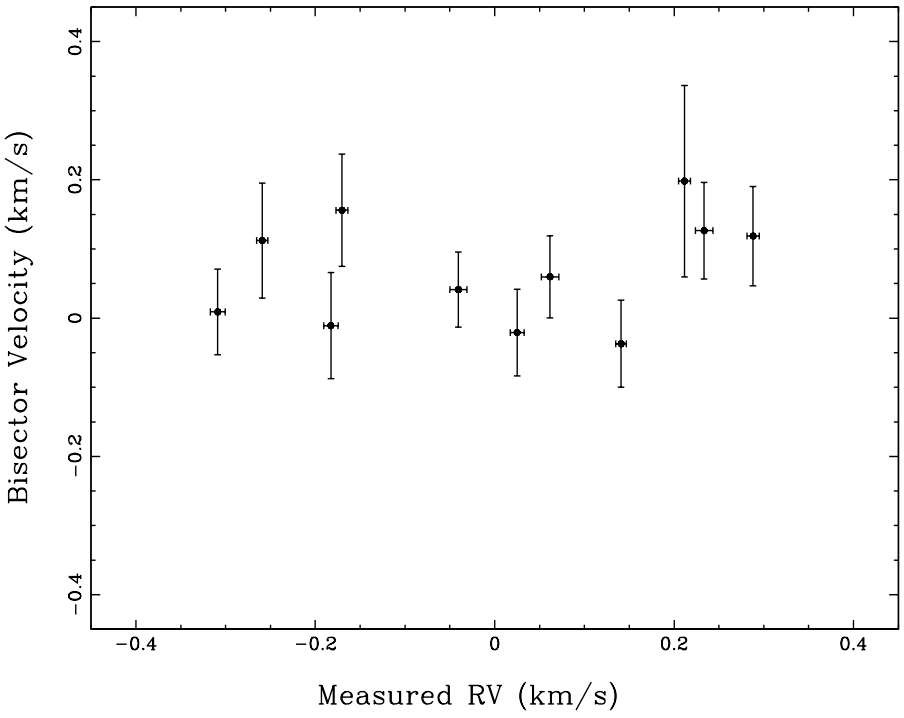

Figure 4.8: Bisector velocity span against the RV's measured for HIP63242. The mean error bars in the bisector velocities is $\sim 70\ \mathrm{m\,s^{-1}}$, much smaller than the RV amplitude observed for this star.

planet discovered between 0.1 and 0.6 AU around an intermediate-mass star, and the first one orbiting within 0.6 AU around an intermediate-mass giant star (see Figure 1.19), and 2) since the host star is ascending the red giant branch, the presence of this planet supports the idea of the planetary destruction by the host star during the late phase of the RGB, especially considering that in this project and in other surveys no planet has been found in this region of the parameter space around a HB star, which is in agreement with the results from RV studies of giant stars conducted by other groups.

4.3.3 Longer period RV signals

In addition to the RV signals discussed above, there are two other stars that show a large periodic RV variability, that might be produced by orbiting planets. The first one (HIP99171) is a RGB stars with a mass of 1.35 $\mathrm{M_\odot}$, showing a doppler shift that is likely induced by a

massive planet ($M_p \sin i = 10.7\ M_J$), with an orbital period of 367.3 days ($a = 1.1$ AU). The RV curve for this object is plotted in Figure 4.9. The solid black line corresponds to the best keplerian fit. The rms of the fit is 10 $m\,s^{-1}$. The orbital parameter are also labelled.

The second object is HIP97233, which probably hosts two giant planets. The RV curve for this star is shown in Figure 4.10. The black solid line correspond to one possible solution, with two giant planets with orbital periods of 243 days ($a = 0.96$ AU) and 1414 days ($a = 3.1$ AU), respectively. The rms of the fit is 9 $m\,s^{-1}$. In both cases, a further analysis is needed to determine the actual nature of the RV variations, but since the amplitudes are large, the rotational modulation cannot be responsible for the observed RV curves.

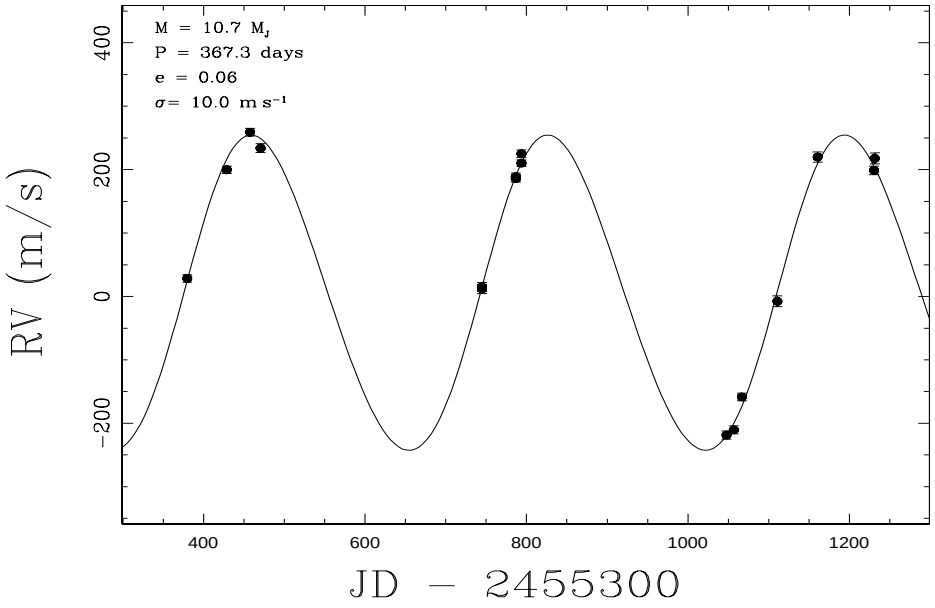

Figure 4.9: RV curve for HIP99171 (black dots). The best keplerian fit is overplotted (black solid line). The orbital parameters are labelled.

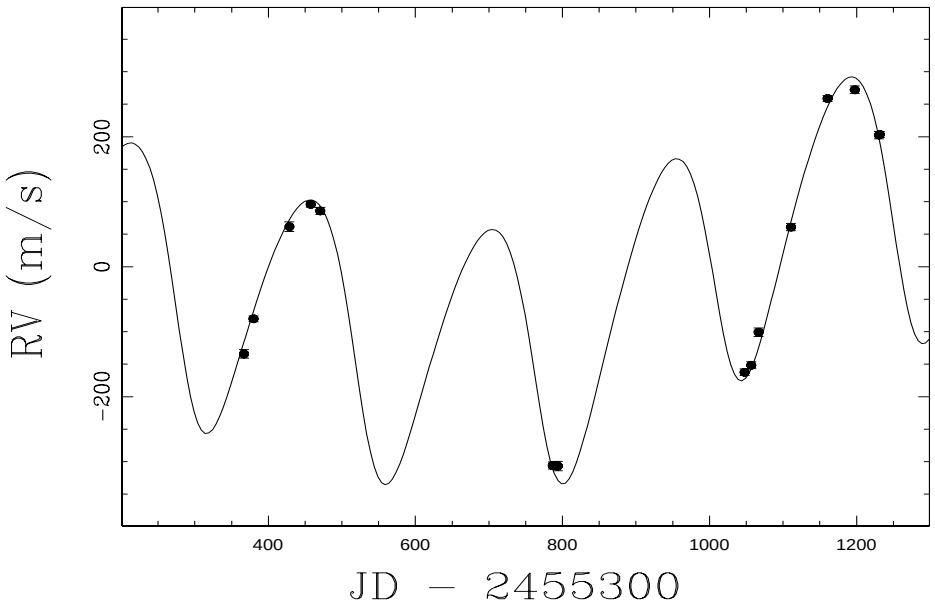

Figure 4.10: RV curve for HIP97233 (black dots). One possible keplerian solution with two planets is overplotted (black solid line).

Chapter 5

Summary and Conclusions

5.1 Summary

5.1.1 Atmospheric and physical parameters

During the last three years a large radial velocity study of a sample of 166 bright giant stars was conducted in the southern hemipshere. Multi-epochs and high-resolution spectra were collected for every target, in order to compute precise RV variation and hence to study the population of close-in planets around RGB and HB stars. The first step of the project was to fully characterize the physical properties and evolutionary states of the stars. In order to do that, their atmospheric parameters (T_{eff}, log$g$, [Fe/H] and microturbulent velocity) were derived using a set of stellar atmosphere models and by imposing local thermodynamic equilibrium. These parameteres were then compared to evolutionary tracks to derive the age and mass of the program stars. Additionally, their rotational velocities were measured using a calibration based on a sample of stars with rotational velocities measured by the Fourier method. A complete catalog with all of this information was built and is available in the VizieR database [1].

[1] ftp://cdsarc.u-strasbg.fr/pub/cats/J/A+A/536/A71/

5.1.2 Clump giants from the CTIO sample

The CTIO sample consists of clump giant stars, i.e., a mixture of massive sub-giants, intermediate-mass RGB stars and low-mass and intermediate-mass Horizontal Branch stars, that occupy a similar region in the HR diagram. In order to derive high-precision RV variations, a molecular iodine cell was used to compute a precise wavelength calibration against which the doppler shift of the star is measured. This technique was used with two different instruments, namely FECH, that was later replaced by CHIRON, both of them mounted on a 1.5m telescope. The RV precision achieved was typically $\sim 10\,\mathrm{m\,s^{-1}}$ and $\sim 5\,\mathrm{m\,s^{-1}}$, respectively. The main results from the RV analysis of the CTIO sample were:

- No giant planet was found in close-in orbits in this sample of 66 giant stars (23 RGB and 43 HB). Since a detailed analysis of each star dataset was performed, no expected observational bias is present, thus reinforcing the observational result about the lack of short period orbit planets around giant stars, already claimed by other groups.

- Several long period signals were detected, which might be either due to stellar activity or induced by the presence of a giant planet or a Brown Dwarf. These targets require follow-up observations in order to determine the actual nature of these signals, and for characterizing the orbital parameters in the case that a planet is present.

- Three new binary systems were discovered during this project, but still more observations in the future are needed to constraint the orbital parameters. These result shows that binary is very common in giant stars, especially considering that in the target selection stars known to host a stellar companion were excluded.

5.1.3 First ascending RGB stars from the FEROS sample

A total of 100 giants stars were observed with FEROS (plus 15 stars in common with the CTIO sample), all of them having B-V color bluer than 1.2. From the total sample, 75 stars have $M_V > 1.5$, meaning that most of them are either at the end of the sub-giant phase or just ascending the RGB phase. Even though, this sample has not been analyzed as was

done for the CTIO sample (because this program is still incomplete in terms of number of observations per star), it is worth to highlight the following emerging results:

- The RV precision achieved with FEROS is better than what was previously expected. During commissioning, the precision obtain for this instrument was $\sim 23\ \mathrm{m\,s^{-1}}$ (Kaufer et al. 1999) and then Setiawan et al. (2007), based on data taken between 2003 and 2006, showed that it is possible to achieve a long-term precision stability at the $\sim 10\ \mathrm{m\,s^{-1}}$ level. Applying the method described in § 4.2, it is possible to reach a long-term precision of $\sim 4\ \mathrm{m\,s^{-1}}$. This is an improvement in 2 or 3 times in the RV precision, showing the huge potential of FEROS as a planet hunter.

- One giant planet was found orbiting at a distance of 0.57 AU, around a first ascending RGB star. This is the closest planet around an intermediate-mass giant star, and the closest one detected around a RGB star[2].

- Two planetary systems, showing large RV amplitudes were detected around two giants, that were identified as RGB stars. In the first case the best keplerian fit is compatible with a massive giant planet ($M \sim 10\ M_{\odot}$) in a nearly circular orbit with ~ 1 year orbital period. In the second case, two massive giant planets are clearly detected in the RV of their host star, the inner one having an orbital period ~ 243 days. More observations are needed to fully constrain the orbit of the second planet in the system.

- Several RV signals are present in the data that might be produced by orbiting planets. In particular, there is one high amplitude signal present in the RV's of a $1.7\ M_{\odot}$ RGB star, with a tentative orbital period of ~ 90 days. Unfortunately, there are only 9 RV epochs for this star, hence still is not possible to come to a firm conclusion about the nature of the periodic signal.

- A total of 16 stars show RV variations that are explained by the presence of either a massive brown dwarf or a stellar companion. This shows that the binary fraction in

[2]There is one planet in a close-in orbit (P = 16 days) around a low-mass HB star (Setiawan et al. 2010, Science, 330, 1642)

giant stars is large. As in the case of the CTIO targets, no previously detected binaries were included in the FEROS sample.

5.2 Conclusions

5.2.1 The Fraction of Planets Around Giant Stars

Based on the results presented in the last section, it is possible to measure the fraction of planets orbiting giant stars by simply compute the ratio between the number of detections and the total number of targets observed. From the FEROS sample, 15 of them have less than 10 observations, hence they will be excluded in this analysis. Also the 16 BD/Binary systems are not included since an analysis of the RV's after substraction of the fits have to be done in order to search for periodicities in the residuals. Hence, a total of three detections will be considered in a a sample of 135 stars. It is worth to emphasize that this is a lower detection limit because there are several stars showing RV signals with periods $\gtrsim$ 180 days, which are currently being monitored in order to determine the actual nature of the observed variability. Additionally, in order to obtain a robust statistical result, planets detected by other groups will be also included in this analysis. Unfortunately, different surveys have different observing strategies, sampling rates, detectability limits, targets selection, etc, thus they cannot be directly compared, which complicates the statistical analysis. However, the results published by some groups can be included in the analysis.

The Okayama Planet Search Program (OPS hereafter; Sato et al. 2005) has monitored a sample of 319 [3] G giants stars (see Takeda et al. 2008 for a detailed description of the targets properties). From the OPS sample, 13 stars hotter than logTeff = 3.72 (hence are clearly subgiant stars) are not included here. To date, a total of 13 planets around giants stars (Brown Dwarfs and subgiant hosts are not included) have been discovered by that survey, covering a wide range in orbital periods. A similar work was done by Hekker et al. (2008), where

[3]Three stars presented in Takeda et al. 2008 are planet hosts that are not part the OPS sample

a sample of 179 giant stars, including clump giants and evolved RGB stars, were analyzed in detail, in order to study the nature of the RV variability observed in giant stars. From that sample, 2 planets were published, having orbital periods of 511 days and and 590 days. In addition, 83 evolved stars, including RGB and clump giants, were studied by Setiawan et al. (2003), from which 5 planets (one double system) were detected, all of them orbiting beyond $\sim$ 1.5 AU. Finally, 62 K giant stars were monitored by the TLS survey (Dollinger et al. 2008), from which 5 giant planets were detected, with orbital periods ranging from 158 days up to 1125 days (0.59 AU $< a <$ 2.36 AU).

Considering the results from the CTIO and FEROS sample and the four different surveys mentioned above, it is possible to compute the fraction planets as a function of the orbital distance. The results are summarized in Table 5.1, where are also listed the values obtained from a sample of 475 solar-type stars presented in Table 1 in Cumming et al. (2008) [4].

Table 5.1: Cumulative fraction (%) of giant planets around dwarfs and giant stars

	0.1 AU	0.42 AU	0.60 AU	1.0 AU	2.0 AU	2.5 AU
FGK dwarfs	0.43	0.85	1.12	1.9	3.9	4.3
Giant stars	0.00	0.00	0.29	1.4	2.9	3.5

It is important to notice from Table 5.1 that the fraction of planets around giant stars is similar to the fraction for dwarfs stars. However, as already mentioned, the results for giant stars are still incomplete (for instance there are a few planet candidates from the CTIO and FEROS samples that still have to be confirmed). In addition, the detectability of planets around giant stars decreases for more massive stars and with the orbital distance. Also, the effect of the stellar jitter complicates the detection of substellar companions, especially when the sampling rate per star is poor (see Figure 3 in Cumming 2004 for the number of

[4]The fraction of planets around dwarfs stars at 0.6 AU and 2.5 AU were linearly interpolated

datapoints needed to detect a planet, given the signal to noise ratio). Hence, the actual fraction of planet around giant stars is probably significantly higher than the one presented here. In fact, based on preliminary results from an extension of the TLS survey, Dollinger et al. (2011) claimed a fraction of $\sim$ 10 - 15 % of giant stars harbouring planets.

5.2.2 The Properties of Planets Around Giant Stars

As has been already mentioned in this thesis, the properties of the planets detected around giant stars are different when compared to solar-type stars. Apparently, two main reasons are responsible for these differences, namely the stellar mass (giants are on average more massive than FGK dwarfs stars by $\gtrsim$ 0.5 $M_{\odot}$) and the stellar evolution. In the next subsections the properties of these systems are investigated.

5.2.2.1 Semimajor Axis Distribution

In Figure 1.19 the mass of the parent star as a function of the orbital distance is plotted, for planets discovered until 2009, around sub-giant and giant stars. After three years, several new planets have been discovered around giant stars, including three detections by this program and the number of planets orbiting sub-giants stars has increased a factor $\sim$ 2. The current semimajor axis distribution is presented in Figure 5.1. The red filled circles and blue stars correspond to giants and subgiants hosts, respectively. The three red triangles correspond to the planets detected during this project. For comparison, also planet hosting MS stars were included (small black dots). It can be noticed that despite the fact that several new planets were added, the lack of close-in planets is still present, even though there are a few new interesting objects that were not present in Figure 1.19. First, there is a planet in a 0.12 AU orbit around a low-mass star, that was identified as a HB stars (Setiawan et al. 2010). However the host stars is an extremely metal poor star ([Fe/H] $\sim$ -2.0) and no parallax have been measured for this object, hence the determination of its evolutionary status and its mass are quite uncertain. In addition, the planet detected during this project around HIP63242 is the closest one around a giant star more massive than $\sim$ 0.8 $M_{\odot}$. This planet has moved the

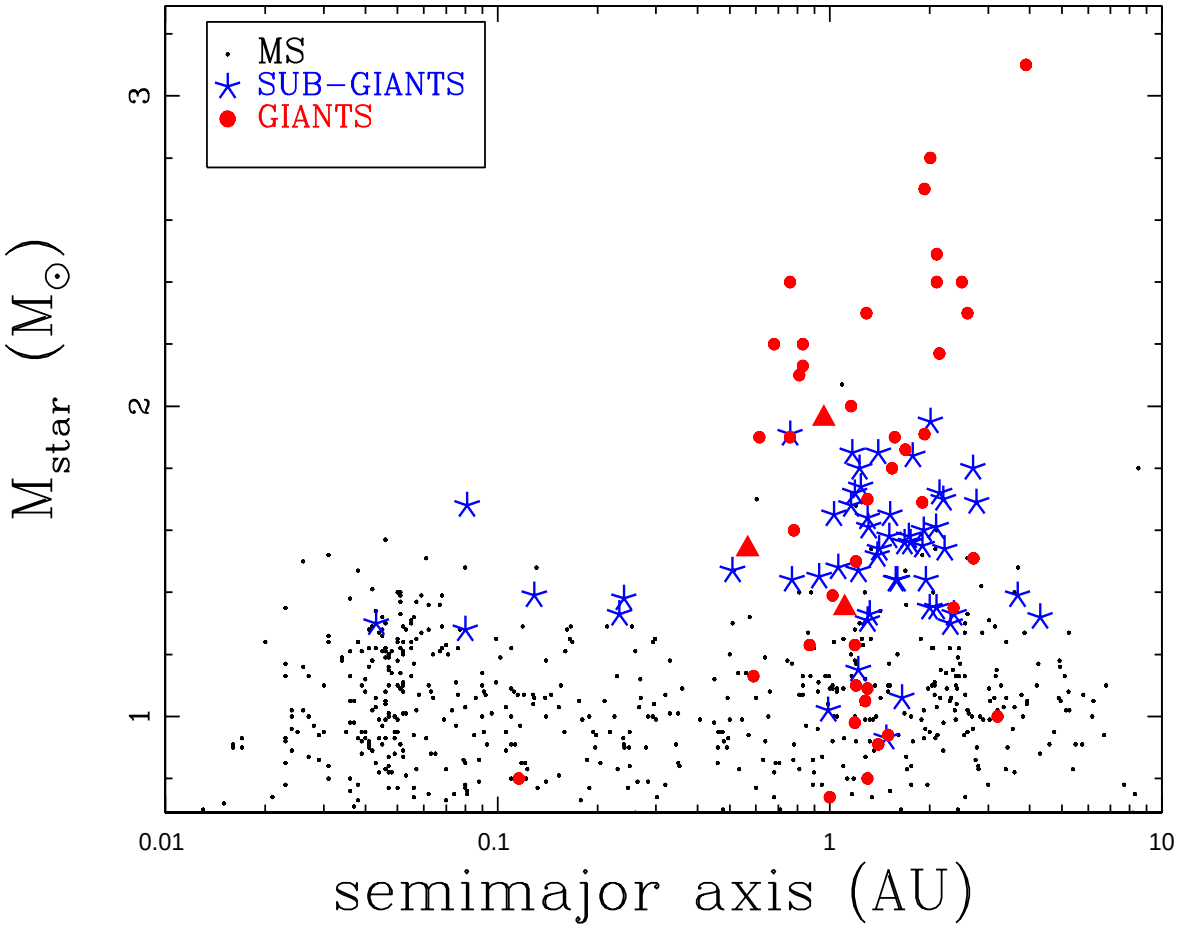

Figure 5.1: Semimajor-axis distribution for planets around evolved stars. The blue stars and red filled circles correspond to sub-giant and giant host stars, respectively. The red triangles correspond to the planets discovered during this project. Planets around MS stars are also plotted (small black dots).

upper boundary of the planet desert a little bit closer to the star. Also it is very important to note that the host star is clearly ascending the RGB, hence no degeneracy in its mass and age are present. Finally, a new planet in a short-period orbit was found around ~ 1.7 $M_{\odot}$ sub-giant star, and several others were detected (by the transit method) orbiting MS stars with $M_{\star} \sim 1.4$ - 1.6 $M_{\odot}$, showing that even though planet in close-in orbits are rare around intermediate-mass stars, they do exist.

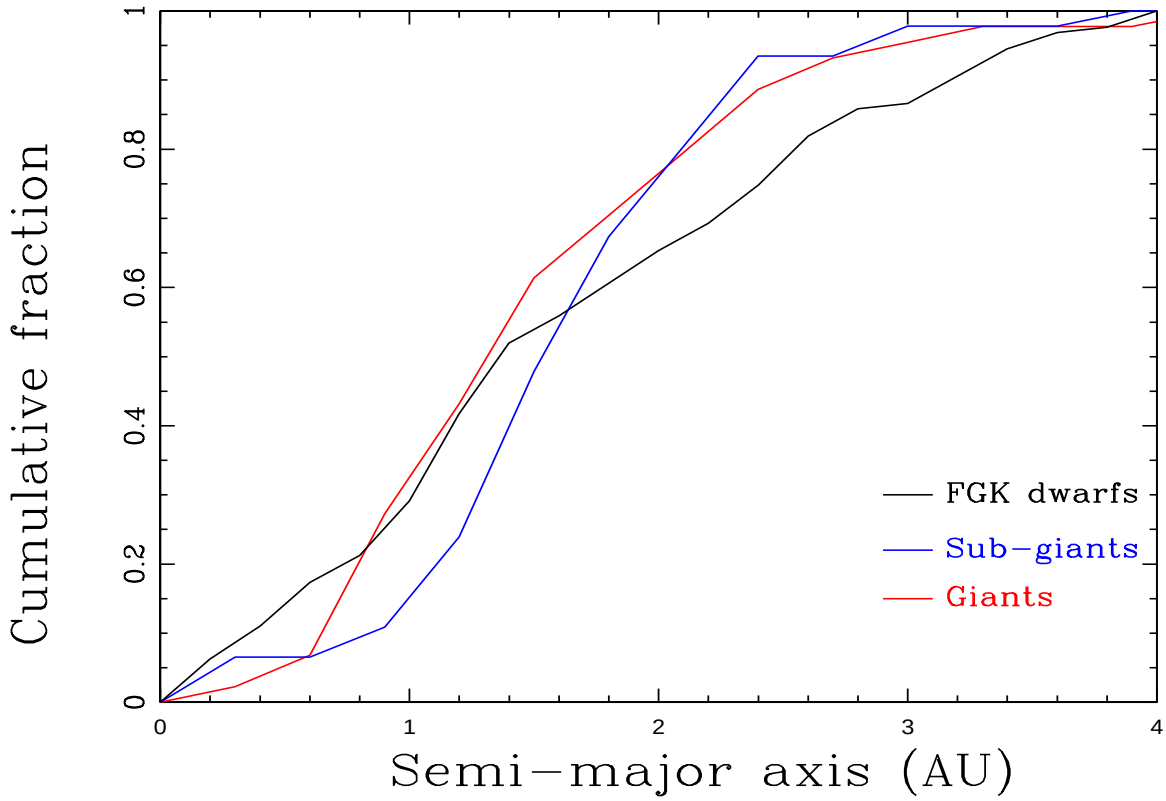

Figure 5.2: Semimajor-axis cumulative fraction of giant planets ($0.9 < M_P/M_J < 13$) around dwarfs ($0.7 < M_\star/M_\odot < 1.2$) and evolved stars. The black, blue and red lines correspond to dwarfs, subgiants and giants hosts, respectively.

The observed gap in the semi-major axis distribution around intermediate-mass stars, has been investigated by Burkert & Lin (2007). They compute a large number of Monte Carlo simulations in order to study whether this planet desert can be theoretically reproduced. They found that for star more massive than 1.2 $M_\odot$, there is a paucity of giant planets more massive than ~ 0.8 M_J, orbiting between 0.1 AU and 0.6 AU from the host star. The main reason causing this discontinuity in the semi-major axis distribution is attributed to a shorter disk depletion timescale, therefore Type II migration [5] is rapidly halted, avoiding the inward motion of gas giant planet from their formation position. A complementary work by Currie (2009) showed that it is possible to reproduce the observed lack of Hot Jupiters

[5]In Type I migration, a small planets creates a spiral pattern in the disk, while in Type II migration a giant planet opens a gap in the protoplanetary disk.

around intermediate-mass stars, by modelling the effect of a stellar-mass-dependent timescale for the disk on type II migration.

In addition, Figure 5.2 shows the cumulative fraction of all of the giant planets (0.9 M_J $< M_p <$ 13 M_J) published, as a function of the orbital distance (up to 4 AU), for MS, subgiant and giant host stars (black, blue and red lines, respectively). In the case of the MS hosts, the mass range was restricted between 0.7 - 1.2 $M_\odot$. It can be noticed in Figure 5.2 the planet desert around evolved stars, i.e., a low fraction of planets orbiting interior to 0.6 AU. It is also worth to mention, that the effect of the stellar mass can be observed in the cumulative fraction of planets around subgiant stars. As can be seen, the fraction of planets up to $\sim$ 1.6 AU, is significantly lower than for MS hosts, which suggests that planets around imtermediate-mass stars are preferably formed in wider orbits. This is also evident in Figure 5.1, since only one planet is found orbiting within $\sim$ 0.7 AU around subgiant stars more massive than $\sim$ 1.5 $M_\odot$. In fact, Bowler et al. (2010) showed that the period distribution of planets around intermediate-mass stars (all of them detected around subgiants) is different than the population of planets around FGK dwarfs, at the $4\,\sigma$ level. Regarding the planetary population around giant stars, there is steep increase in the cumulative fraction between $\sim$ 0.6 AU and 1.5 AU. However, the interpretation of this is extremely difficult to analyze, since the detectability of planets orbiting beyond 2 AU is strongly reduced. For instance, a 1 M_J planet orbiting a 1.5 $M_\odot$ star at a distance of 2 AU induces a RV amplitude of only $\sim$ 16 $\mathrm{m\,s^{-1}}$, barely above the jitter level for the stable giant stars.

5.2.2.2 Mass Distribution

As already noticed by other authors (e.g. Lovis & Mayor 2007; Dollinger et al. 2009) planets around giant stars (or around intermediate-mass stars) are significantly more massive than the substellar companions orbiting solar-type (or low-mass stars). In Figure 5.3 the minimum mass of the planets versus the mass of the parent star are plotted. The black squares, blue triangles and red circles correspond to MS, subgiant and giant host stars, respectively. The

black dashed line represents a RV amplitude of 30 $\mathrm{m\,s^{-1}}$ for a planet orbiting at a distance of 1 AU. It is evident that planets around giant stars are significantly more massive than

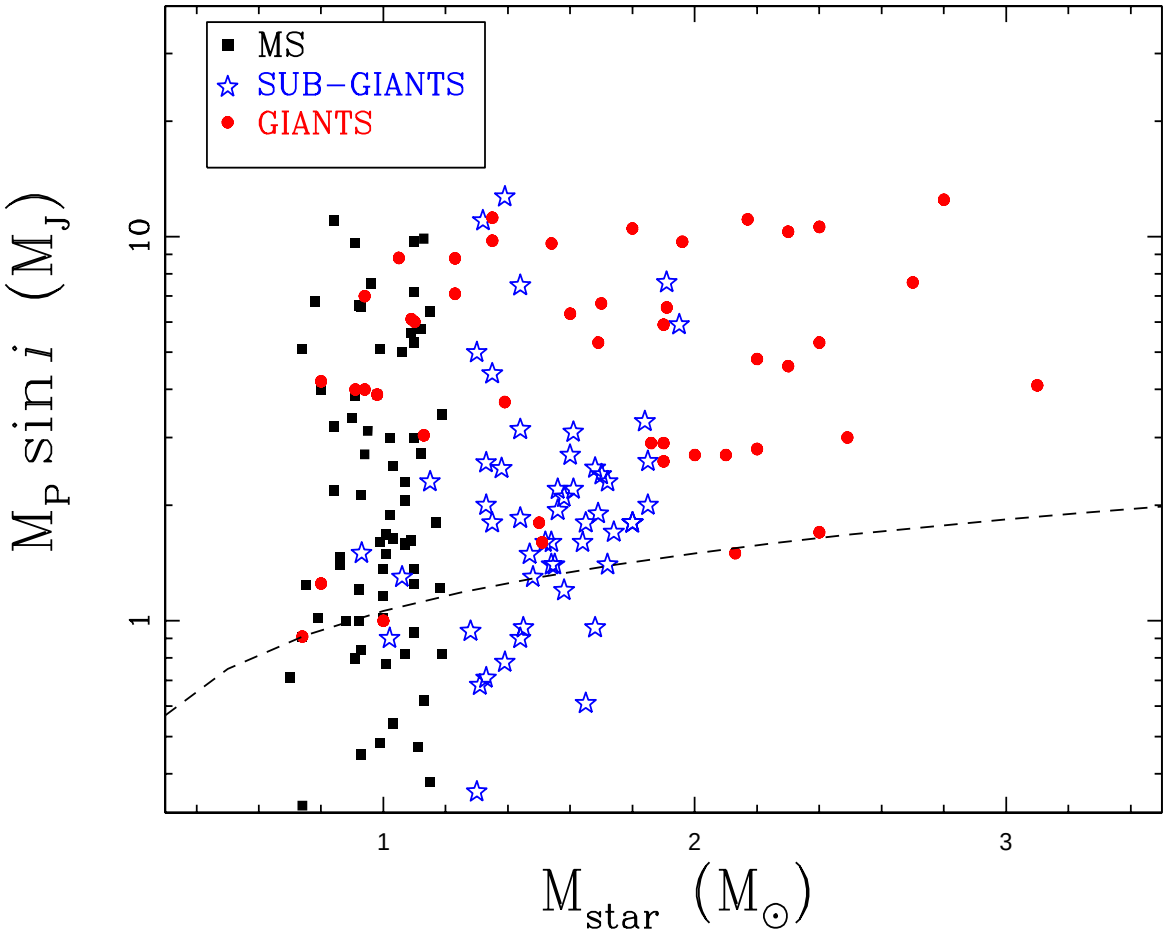

Figure 5.3: Mass distribution for planets orbiting MS (black squares), subgiant (blue triangles) and giant stars (red circles). The black dashed line represents the detection limit ($\mathrm{K = 30\ m\,s^{-1}}$) for a planet orbiting at 1 AU.

around MS and subgiant stars. This result can be interpreted in part due the fact that the properties of substellar companions (in this case the mass of the planets) are strongly affected by the stellar mass, which probably directly correlates with the properties of the protoplanetary disk. Thus probably more massive stars have denser and more massive disk, from where super planets can efficiently be formed. From a theoretical point of view, Kennedy & Kenyon (2008) predicted that the frequency of giant planets increases considerably with the stellar

mass, which explains in part the mass distribution of planets around intermediate-mass stars ($M \gtrsim 1.5$ $M_\odot$). However, the former argument does not explain the difference in the mass distribution between subgiant and giant stars. In order to investigate how different these two population are, only the planets orbiting star with masses between 0.9 $M_\odot$ and 2.0 $M_\odot$ will be considered. In this mass range, there are 53 planets around subgiants and 28 planets orbiting giants. A K-S test gives a probability that both datasets come from the same distribution of only 5×10^{-8} %. The reason of this difference in the planet mass distributions is not clear, but might be attributed to different scenarios.

One possibility is that most of the massive planets detected around giant stars are not planets, but rather the RV variability is intrinsically related to stellar phenomena, such as oscillations or spots. However this option seems to be very unlikey, since these kind of phenomena should translate into a larger photometric variability and/or are expected to be detected in the bisector analysis, especially because these massive planets induce RV amplitudes ~ 100 $m\,s^{-1}$. As explained in section 4.3.2.1, such a large variation should be easily detected in photometric data or in a line profile analysis.

A second option is that the host stars are actually less massive, hence the the mass of the planets derived from equation 1.5 are smaller (since $K \propto {M_\star}^{-1/2}$). Interestingly, Lloyd (2011) suggested that the giant stars hosting exoplanet are the evolved counterpart of late F and early G MS stars, with masses of $\sim$ 1.0-1.2 $M_\odot$. However, even considering that this is the case, this idea cannot be solely responsible for the planets mass distribution around giants stars. For instance, let us consider a stars that was originally identified as a 1.5 $M_\odot$ star, hosting a 10 M_J mass planet. Let us also consider that the actual mass of the host is 1.0 $M_\odot$ instead of 1.5 $M_\odot$. Hence, the mass of planet would decrease a factor $\sqrt{1}.5 = 1.22$, meaning that its mass would be 8.2 M_J. If we repeat this procedure for all of the stars in the region between $\sim$ 0.9 and 2.0 $M_\odot$, there would still remain an overabundance of massive giant planets. Indeed if we assume that all of the giant host stars are a factor 1.5 less massive

than their derived mass, then every planet has a minimum mass ~ 1.22 times smaller. A new K-S test after appliying this correction factor gives a 4×10^{-5} probability that the observed mass of exoplanets around subgiants and giants stars follow the same distribution, hence this option can be discarded.

A third possibility is that, due to tidal decay during the RGB phase, massive planets that are formed beyond ∼2-3 AU move inward, thus are detected around giant stars but are not seen around subgiant stars, since they are too far and produces smaller RV amplitudes. However, this scenario is in disagrement with the theoretical predictions of tidal decay, where the exchange of angular momentum is negligible beyond a certain orbital distance (which also depends on the mass of the planet and the mass of the star). In fact, according to equation 1.14, the strong dependence of the tidal force with the relative orbital distance will produce a very narrow region where the planet is either engulfed by the host star or it survives and its orbital distance remains nearly unchanged (see also Figure 1 in Villaver & Livio, 2009).

Finally, the overabundance of super Jupiters might be due to a growth of the planet size by accretion either from the host star envelope or from the stellar wind. These ideas have been studied from a theoretical point of view in several works (e,.g. Livio & Soker 1983, 1984). In the former hypothesis, even though there might be a significant amount of accreted mass from the stellar envelope, the planet will rapidly spiral inward due to tidal and viscous forces, thus it is dissipated at the bottom of the stellar convective envelope (Siess & Livio, 1999). Also, Livio & Soker (1984) showed that a substellar object more massive than ~ 20 M_J can survive inside the envelope of the star, and indeed accrete a significant amount of mass. As a result the brown dwarf ends up in a very close-in orbit and having a mass $\gtrsim 0.15$ $M_\odot$, hence this scenario can be discarded. On the other hand, accretion from the stellar wind (outside the envelope of the host star) seems to be a possible mechanism to explain the overabundance of super planets around giant stars. Unfortunately, none of the afore mentioned studies focus the discussion on this point, although Livio & Soker (1983) and Villaver

& Livio (2009) explicitly mention that the accretion and evaporation rates are unimportant in the orbital evolution of the planets. Therefore, in order to study the effect of the accretion from the stellar wind, here some basic calculations are presented. Fisrt let us consider only accretion from the stellar wind, thus no evaporation of gas in the outer part of the planet. Under this assumption the rate of change of the planet $\dot{m}$ is simply proportional to the star mass loss rate, given by:

$$\dot{m} = \beta \dot{M}_{\star} \tag{5.1}$$

where $\dot{M}_{\star}$ corresponds to the stellar mass loss rate and β is a proportional constant given by the fraction of the wind that is accreted by the planet. According to Bondi & Hoyle (1944), the accretion rate by an object that is moving at supersonic velocity v in a medium (which is the case of the planet), is given by:

$$\dot{m} = \frac{4\,\pi\,G^2\,m_p^2\,\rho}{v^3} \tag{5.2}$$

where m_p is the mass of the planet, ρ the density of the stellar wind at the position of the planet and G is the gravitational constant. The value of ρ depends mainly of three quantities, namely the mass loss rate, the velocity of the wind and the planet's orbital distance, a. Assuming that the wind is spherically ejected at a velocity v_W, then the value of ρ at the planet distance is given by (Villaver & Livio, 2009):

$$\rho = \frac{\dot{M}_{\star}}{4\,\pi\,a^2\,V_w} \tag{5.3}$$

Hence, equation 5.3 can be replaced in equation 5.2 in order to derive the accreted mass. However, the value of $\dot{M}_{\star}$ in not constant through the RGB phase, thus equation 5.2 have to be integrated along the stellar evolution. However, it is still possible to approximate the results using an average value for $\dot{M}_{\star}$ during the RGB phase and then multiply this number

by the timescale spent by the star in this phase. As an example, let us consider the case of the sun, for which Schroder & Connon (2008) derived a total mass loss of 0.33 $M_\odot$ during the whole RGB phase. Considering a timescale in the RGB for the sun of $\tau_{RGB} \sim 10^9$ years, then the average mass loss during this phase is $\sim 3.3 \times 10^{-10}$ $M_\odot$ yr^{-1}. Using this value it is possible to compute the total accreted mass by a planet, as a function of the planet mass, orbital distance and wind velocity. The result of the calculations are plotted in Figure 5.4. The orbital distance was fixed to 0.5 AU around a 1.0 $M_\odot$ and the afore mentioned mass loss prescription was used. In addition, the mass accreted by the planet was computed for three

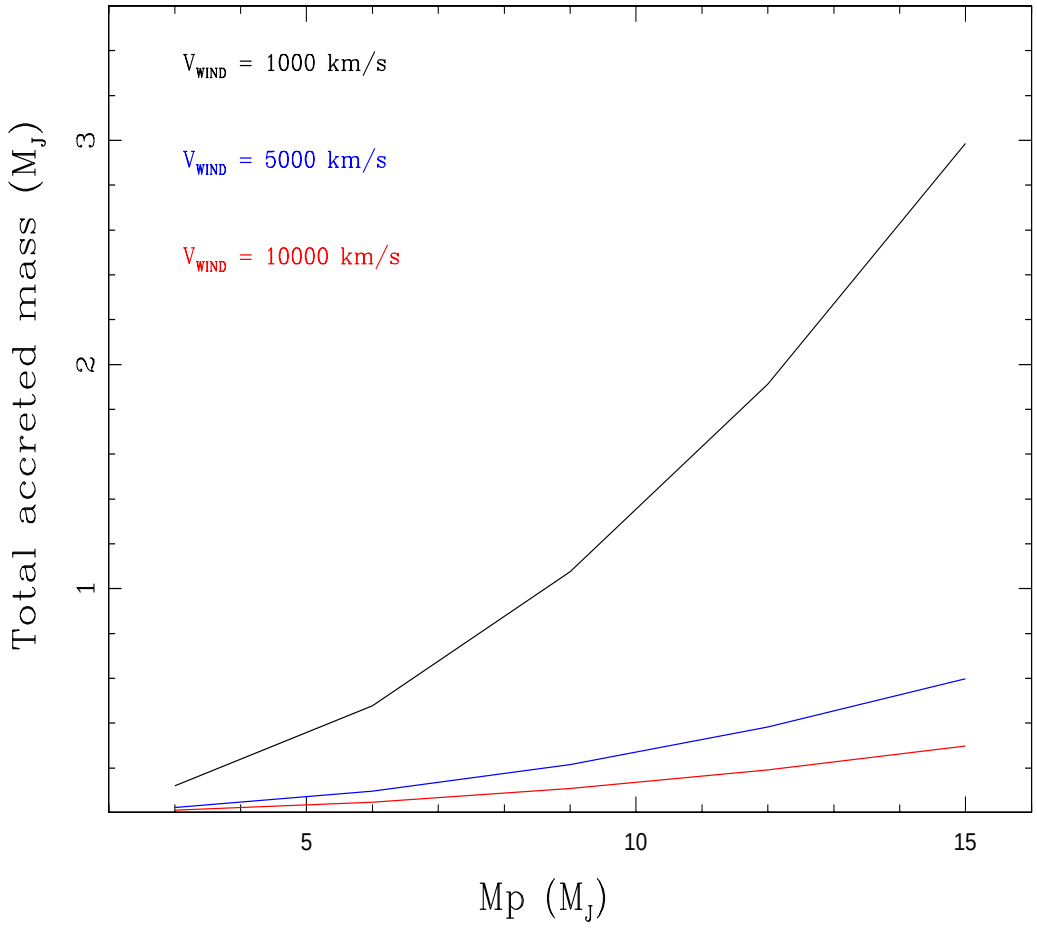

Figure 5.4: Total mass accreted during the RGB phase by a planet as a function of its mass. The orbital distance was fixed to 0.5 AU. The red, blue and black lines correspond to wind velocities of 10000, 5000 and 1000 $km\,s^{-1}$, respectively.

different values of the stellar wind velocity: 1000 $\mathrm{km\,s^{-1}}$ (black line), 5000 $\mathrm{km\,s^{-1}}$ (blue line) and 10000 $\mathrm{km\,s^{-1}}$ (red line). It can be noticed from Figure 5.4 that for lower mass planets and high velocities of the stellar wind, the accretion rate is too slow. The effect of the planet's mass is playing a role in the gravitational radius, within which the material from the wind is accreted, hence the more massive the planet the faster the accretion. On the other hand, the density of the stellar material at the position of the planet is inversely proportional to the wind velocity, thus explaining the three different regimes plotted in Figure 5.4. From these calculations the conclusion is that this mechanism cannot be responsible for the mass differences observed between giant planets around subgiant and giant stars. However, more detailed calculations should be performed to address this problem in a more reliable way (for instance by computing the accretion rates of planets around stars with different masses). On the other hand, the strong dependence of the accretion rate with the mass of the planet (see equation 5.2) suggests that brown dwarf orbiting in relatively close orbits around RGB stars, might increase significantly their mass (actually are predicted to become low-mass stars; Livio & Soker, 1984) thus they might be very rare around post-RGB stars.

5.2.2.3 Metallicity Distribution

The metallicity distribution of MS planet hosts have been studied in detailed by different authors, who have found a strong correlation between the ocurrence probability of a planet and the metallicity of the host stars (e.g. Gonzalez 1997). In particular, Santos et al. 2001 showed that the mean metallicty of planet hosts is [Fe/H]= +0.15, whereas those without planets have a mean metallicity of [Fe/H]= -0.10. In addition, Fischer & Valenti 2004, based on a sample of $\sim$ 850 stars analyzed in a uniform way, showed that the occurrence rate of giant planet scales as $f \propto 10^{\,2\,[\mathrm{Fe/H}]}$. These results have been used in favor of the core-accretion model, where the formation and growth of the planetesimals is highly dependent on the metal content (which form dust) in the protoplanetary disk. On the other hand, in contrast to what is observed for MS hosts stars, the giant stars that harbour planets do not show any trend toward metal richness (e.g. Sadakane, et al. 2005; Pasquini et al. 2007).

Figure 5.5 shows a histogram with the metallicity distribution of planet hosting subgiant (blue dashed line) and giant stars (red solid line). In the subgiants sample, some planets detected by metal-biased surveys (N2K and Elodie Survey) were not included, aswell as the planet around the extremely metal-poor giant star detected by Setiawan et al. (2010). The mean metallicity for both distributions are [Fe/H] = 0.08 ± 0.21 and [Fe/H] = -0.17 ± 0.24, respectively. Here the errors corresponds to the RMS around the mean, as given by Santos et al. 2001). Clearly, the metallicity distribution for the giant host stars contrasts with the trend observed in MS host stars.

Pasquini et al. (2007), argued that the enhanced metallicity of the MS host stars is explained

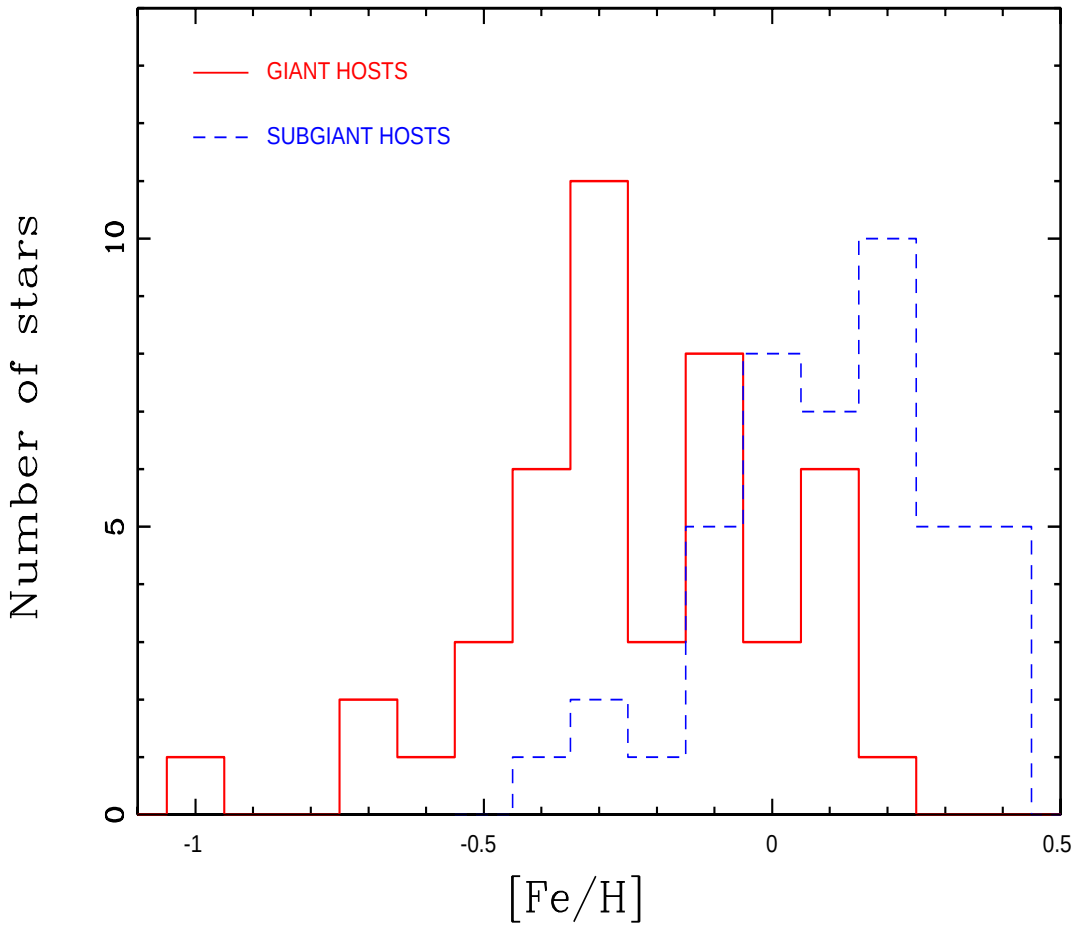

Figure 5.5: Metallicity histogram of post-MS stars harbouring planets.

by pollution, instead to be primordial, i.e., that the cloud from which is formed the star (and thus the protoplanetary disk) is metal rich. In this scenario, a significant amount of material (including planetesimals and/or planets) fall into the star, enhancing the metal abundance in its atmosphere (e.g. Laughlin & Adams 1997). However, after these stars evolve off the MS, they develop large convective envelopes, where the metal excess is rapidly diluted. This idea seems to explain the low metal content of the plantet hosting giant stars, but it does not explain why the subgiant host stars are also on average metal rich. However, since the distribution for MS stars peaks at $\sim +0.15$, it is possible that the subgiant stars have partially diluted the metal excess in their atmospheres, thus the blue dashed distribution might be interpreted to be a "transition" between the MS and giant stars metallicity distributions, since subgiant stars still have smaller convective regions than the giant stars.

Another explanation for this discrepancy is that massive giant planets are preferentially formed by the disk instability mechanism (Boss 1997), which is nearly independent of the amount of metals and dust in the protoplanetary disk. Additionally, in this scenario, giant planets can be rapidly formed ($t \sim 10^3$ yr), prior to gas depletion. Since more massive stars have much stronger radiation field, the disk dissipation timescale (due to strong radiation pressure and photoevaporation) might be too short so that giant planets are not efficiently formed by the core-accretion mechanism ($t \gtrsim 10^6$ yr; e.g. Pollack et al 1996).

5.2.3 Stellar Mass or/and Stellar Evolution?

In order to investigate what is the main reason (stellar mass or evolution of the host star) causing the different properties observed in exoplanets orbiting MS and evolved stars, let us analyze all of the evidence collected in each case.

First, as already mentioned in section 5.2.2.1, Bowler et al. (2010) performed a detailed analysis of the differences in the Period-Mass distribution between low-mass stars (results from the Keck Planet Search; Cumming et al. 2008) and the intermediate-mass (M > 1.5 $M_{\odot}$) subgiant stars (from the Lick Survey; Johnson et al. 2006). They found that the frequency of giant planets orbiting within 3.0 AU is 26^{+8}_{-7} %. This is much higher than the $\sim$ 5 % frequency for low-mass hosts. In addition, Bowler et al. (2010) also studied whether the period distribution is consistent with the one for low-mass stars, which is given by the following parametric model (Cumming et al. 2008):

$$dN = C\, M^{\alpha}\, P^{\beta}\, d\,ln\, M\, d\,ln\, P \tag{5.4}$$

where M and P represent the orbital period and mass of the planet. α and β are equal to -0.31 $\pm$ 0.2 and 0.26 $\pm$ 0.1, respectively. Finally, C is a constant that gives the total fraction of planets having orbital periods up to $\sim$ 2000 days. They found, that even by scaling the value of C to the $\sim$ 26 % occurrence rate for intermediate-mass star, the given values of α and β cannot reproduce their results. In fact, they found a probability of only 0.002 % (after rescaling the value of C) that the planets around intermediate-mass stars follows the same P-M distribution as the one presented in equation 5.4. This result appears as an extension to the intermediate-mass regime of previous studies on MS stars. For instance, Butler et al. (2006) showed that the frequency of giant planets orbiting up to 2.5 AU increases from f = 1.8 $\pm$ 1.2, for M and late F dwarfs (M $\lesssim$ 0.6) to f = 5.6 $\pm$ 1.6, for FGK host stars (0.5 $M_{\odot}$ < M< 1.1 $M_{\odot}$). Based on these results, it is clear that the properties of the planetary

systems are strongly correlated with the mass of the host star.

On the other hand, the effect of the stellar evolution in the orbits of planets can be studied by comparing the properties of exoplanets around subgiants or RGB stars with those orbiting post-RGB stars. The main observational evidence supporting this scenario is the lack of close-in planets around giant stars, which is in part explained by the effect of the stellar mass. In fact, as can be seen in Figure 5.1, planets are very rare around intermediate-mass subgiants, thus they are not detected around giant stars not because of the stellar evolution but probably because they are not formed in that region. However, the planet desert is still present around giant stars with mass between $\sim$ 1.0 - 1.5 $M_{\odot}$. In this region of the parameter space, four planets were detected orbiting subgiant stars interior to 0.25 AU, and several other short-period systems are found around MS hosts. Nevertheless, this result might be also attributed to the fact that only few giant targets with masses between $\sim$ 1.0 - 1.5 $M_{\odot}$ have been monitored. For instance, according to the results presented in Takeda et al. (2008), out of the 319 stars observed by the OPS, only 12 of them are less massive than 1.5 $M_{\odot}$. In addition, as shown in Table 2.2, only 41 stars presented in this thesis have $M_{\star}$ < 1.5 $M_{\odot}$. Having this premise in mind, it is not surprising that still no close-in planet was detected. In fact, for solar-mass stars, the fraction of stars harbouring planets within 0.5 AU is $\sim$ 1% (see Table 5.1).

In summary, the current statistics (including the new detections during this project) are still poor, thus no firm conclusion can be drawn regarding the effect of the stellar evolution on the orbits of close-in planets. In order to obtain a stronger result and to disentangle the effect of the stellar mass from the stellar evolution in the planetary population around giant stars, a larger sample of giant stars should be monitored, especially in the stellar mass range between 1.0-1.5 $M_{\odot}$. In fact, according to stellar evolutionary models, the effect of the tidal decay is much stronger for a 1.0 $M_{\odot}$ than for a 3.0 $M_{\odot}$, because the stellar radius at the end of the RGB phase decreases with increasing mass.

5.2.4 Future Work

Although, the first results of this long-term RV survey have been presented in this thesis, a subsample of giant stars are currently being monitored. Additional RV epochs are required for the following reasons:

- **Follow-up of the CTIO planet candidates.** As already explained in chapter 3, there a a bunch of stars that show RV variations that might be induced by giant planets or brown dwarfs. These planet candidates are currently being observed with CHIRON, and further telescope time was requested for 2013, in order to determine if these RV variations are actually induced by planets or if they are related to stellar activity. In addition the orbital parameters of the three binaries detected in the CTIO sample are still to be resolved.

- **Finishing the FEROS program.** As mentioned in chapter 4 the FEROS sample is still incomplete in term of the number of observations. Out of the sample of 100 stars, $\sim$ 25 of them still have between 7 and 10 spectra (hence 6-9 RV epochs, because one spectrum is used as a template). Also, the three planetary systems candidates presented in chapter 4 will be reobserved in order to put strong constraints in their orbital properties. In particular, many additional RV epochs are needed to fully resolve the parameters of the double system around HIP97233. Finally, the time coverage for several binary stars present in the FEROS sample is still too short, therefore further RV epochs are needed to cover at least half of their orbital period. During the current period three more nights were awarded for this project. Further telescope time was requested for the next semester.

- **Asteroseismic study of giant stars.**

  Multiple RV epochs were obtained in two different nights for two stars in the FEROS sample. The idea behind this procedure is to study whether it is possible to substract the strongest oscillation modes (timescales of several hours) of the stars from the RV variations, which might help to push the detection limits towards smaller planets.

In terms of the scientific outcome, the following topics will be studied (after the data acquisition):

- **Detection fraction in the FEROS sample.** A detailed analysis (via periodogram and RV variability) will be done for the FEROS sample, in order to derive the fraction of close-in giant planets (as presented in chapter 3).

- **Confirmation of planetary systems.** The exoplanets detected during this project will be published, including a detailed analysis of the stellar activity indicators (bisector study, photometric variability, Ca II lines emission).

- **The fraction of brown dwarfs around giant stars.** A study of the fraction and properties of the Brown dwarfs detected during this project (if any) will be presented. Using published data in the literature it might be possible to test the hypothesis of the brown dwarf growth via accretion from either the stellar wind or from the envelope of the star, as discussed in section 5.2.2.2.

- **Binary fraction among giant stars.** In this project, a total of 19 binary systems were discovered (some of them might be actually massive brown dwarfs). The properties of the binaries will be published, including the analysis of binary fraction among giant stars. Also, there is at least one system in the FEROS sample corresponding to a pre-common envelope system, for which it is worth to study its dynamical evolution.

- **FEROS pipeline.** An improvement of the FEROS RV computation method will be done. In particular a fully automatic pipeline will be developed in order to compute high precision radial velocities. Second order effects will be included, such as a the fiber-to-fiber drift during the night. The main goal is to reach a 3 $\mathrm{m\,s^{-1}}$ precision using high signal to noise ratio spectra.

In addition to the science cases listed above, it would be desirable to increase the sample of giant stars presented in this thesis, in order to search for new planetary systems that might give us some clues regarding the effect of the stellar evolution. In this case it might be worth

to bias the data sampling, assigning a higher priority to those stars showing an excess of RV variability, which could be an indication of the presence of a substellar companion in a close-in orbit.

References

Alibert, Y. et al. 2005, A&A, 434, 343

Alonso, A., Arribas, S. & Martinez-Roger, C. 1999, A&A, 140, 261

Anglada-Escude, G. et al. 2012, ApJ, 751, 16

Arenou, F., Grenon, M. and Gómez A. 1992, A&A, 258, 104

Bailes, M., Lyne A. G. & Shemar S. L. 1991, Nature, 352, 311

Barban C. et al. 2004, ESA SP, 559, 113

Bedding T. R. et al. 2010, ApJ, 713, 176

Belmonte, J. A. et al. 1990, ApJ, 358,595

Bondi, H. & Hoyle, F. 1944, MNRAS, 104, 273

Boss, A. P. 1997, Science, 276, 1836

Bowler, B. P. et al. 2010, ApJ, 709, 396

Buonanno, R. et al. 1994, A&A, 290, 69

Burbidge, M. et al. 1957, Phys. Rev., 29, 547

Burkert & Ida 2007, ApJ, 660, 845

Butler R. P. et al. 1996, PASP, 108, 500

Butler R. P. et al. 2006, PASP, 118, 1685

Carlberg, J. K., Majewski S. R. & Arras, P. Carney B. W. et al. 2008, AJ, 135, 892

Carretta E. et al. 2004, A&A, 422, 951

Charbonneau, D. et al. 2002, ApJ, 568, 377

Charbonnel, C. et al. 1993, A&AS, 101, 415

Chauvin et al. 2004, A&A, 425, 29

Cumming, A. 2004, MNRAS, 354, 1165

Cumming, A. et al. 2008, PASP, 120, 531

Currie, T. 2009, ApJ, 694, 171

da Silva, L. et al. 2006, A&A, 458, 609

D. S. P. Dearborn, J. C. Lattanzio, & P. P. Eggleton 2006, ApJ, 639, 405

Dollinger, M. P. et al. 2007, A&A, 472, 649

Dollinger, M. P. et al. 2009, A&A, 505, 1311

Dollinger, M. P. et al. 2011, AIPC, 1331, 79

Dorren, J. D. & Guinan, E. F. 1994, ApJ, 428, 805

Doyle L. R. et al. 2011, Science, 333, 1602

Dumusque et al. 2012, Nature, Accepted for publication

Figueira, P. et al. 2010, A&A, 513, 8

Fischer, D. & Valenti, J. 2005, ApJ, 622, 1102

Fitzpatrick, M. J. 1993, ASPC, 52, 472

Forveille, T. et al. 2011, arXiv:1109.2505

Frandsen, S. et al. 2002, A&A, 394, 5

Ghezzi, L. et al. 2010, ApJ, 725, 721

Girardi, G. et al. 2002, A&A, 391, 195

Goldreich, P. & Soter, S. 1966, Icarus, 5, 375

Gonzalez, G. 1997, MNRAS, 285, 403

Gratton, R. G., Carretta, E. and Castelli, F. 1996, A&A, 314, 191

Gratton, R. G. et al. 1999, A&A, 350, 955

Gratton, R. et al. 2003, A&A, 404, 187

Gray D. F. 1982, ApJ, 262, 682

Gray D. F. 1989, ApJ, 347, 1021

Gray D. F. 2005, The Observation and Analysis of Stellar Photospheres, 3rd Edition, by D. F. Gray (UK: Cambridge University Press, 2005)

Hatzes, A. 2002, AN, 323, 392

Hekker, S. et al. 2006, A&A, 454, 943

Hekker, S. & Meléndez, J. 2007, A&A, 475, 1003

Hekker, S. et al. 2008, A&A, 480, 215

Hekker, S. et al. 2009, A&A, 506, 465

Holman, M., Touma, J. & Tremaine, S. 1997, Nature, 386, 254

Huelamo, N. et al. 2008, A&A, 489, 9

Levison, H. F., Lissauer, J. J. & Duncan, M. J. 1998, AJ, 116, 1998

Lin, D. N. C. & Ida, S. 2007, ApJ, 477, 781

Lovis C. et al. 2011, arXiv:1107.5325

Ida, S. & Lin, D. N. C. 2004, ApJ, 604, 388

Jenkins, J. S. et al. 2008, A&A, 485, 571

Jenkins, J. S. et al. 2009, MNRAS, 398, 911

Jenkins, J. S. et al. 2011, A&A, 531, 8

Johnson, J. A. et al. 2006, ApJ, 652, 1724

Johnson, J. et al. 2007, ApJ, 665, 785

Johnson, J. A. et al. 2011, ApJS, 197, 26

Jones H. R.A. et al. 2003, MNRAS, 341, 948

Jones, M. I. et al. 2011, A&A, 536, 71

Jones, M. I. et al. in preparation

Kalas, P. et al. 2008, Science, 322, 1345

Kallinger, T. et al. 2008, A&A, 478, 497

Kallinger, T. et al. 2009, ASPC, 404, 307

Kaufer, A. et al. 1999, The Messenger 95, 8

Kennedy, G. M. & Kenyon S. J. 2008, ApJ, 673, 502

Kunitomo, M. et al. 2011, ApJ, 737, 66

Kurucz, R. L.: ATLAS9 Stellar Atmosphere Programs and 2 km/s Grid, CD-ROM No. 13 (Smithsonian Astrophysical Observatory, Cambridge 1993)

Laughlin, G. & Adams, F. C. 1997, 1997, ApJ, 491, 51

Livio, M. 1983: Star-Planet Systems and their Relations to Low Mass Cataclysmic Variables (Astrophysics and Space Science Library)

Livio, M. & Soker, N. 1983, A&A, 125, 12

Livio, M. & Soker, N. 1984, MNRAS, 208, 763

Lovis, C. & Mayor, M. 2007, A&A, 472, 657

Lovis, C. et al. 2011, A&A, 528, 112

Lloyd, J. P. 2011, ApJ, 739, 49

Luck, R. E. and Heiter, U. 2007, AJ, 133, 2464

Lyne A. G.& Bailes M. 1992, Nature, 355, 213

Marigo, P. et al. 2008 A&A, 482, 883

Marino A. F. et al. 2008, A&A, 490, 625

Marois, C. et al. 2008, Science, 322, 1348

Mayor, M. & Queloz, D. 1995, Nature, 378, 355

Mc William, A. 1990, ApJS, 74, 1075

Melo C. H. F., Pasquini L. and De Medeiros R. 2001, A&A, 375, 851

Merline W. J. 1999, ASPC, 185, 187

Meschiari, S. et al. 2009, PASP, 121, 1016

Mocak, M. et al. 2008, A&A, 490, 265

Monaco, L. et al. 2005, A&A, 441, 141

Moni Bidin, C. 2009, Ph.D. Thesis, Universidad de Chile

Niedzielski, A. et al. 2009, ApJ, 696, 276

Nordhaus, J. et al. 2010, MNRAS, 408, 631

O'toole, S. J., Tinney, C. G. & Jones H. R. A. 2008, MNRAS, 386, 516

Pasquini, L. et al. 2007, A&A, 474, 979

Pepe, F. et al. 2011, A&A, 534, 58

Perryman, M. A. C. et al. 1997, A&A, 343, L49

Pollack, J. B. et al. 1996, Icarus, 124, 62

Queloz, D. et al. 2001, A&A, 379, 279

Randich, S. et al. 1999, A&A, 348, 487

Rasio et al. 1996, ApJ, 470, 1187

Saar, S. H. et al. 1998, ApJ, 498, 153

Sadakane, K. et al. 2005, PASJ, 57, 127

Salasnich, L. et al. 2000,A&A, 361, 1023

Santos, N. C., Israelian, G. and Mayor, M. 2001, A&A, 373, 1019

Sato, B. et al. 2005, PASJ, 57, 97

Sato, B. et al. 2008, PASJ, 60, 539

Sackmann I., Boothroyd, A. & Kraemer, K. 1993, ApJ, 418, 457

Schrijver C. J. & Pols O. R. 1993, A&A, 278, 51

Schroder K. P. & Connon Smith, R. 2008, MNRAS, 386, 155

Schwab, C. et al., 2010, Proc. SPIE, Vol. 7735, 77354

Sestito, P. et al. 2006, A&A, 458, 121

Setiawan, J. et al. 2000, Messenger, 102, 13

Setiawan, J. et al. 2003, A&A, 397, 1151

Setiawan, J. et al. 2004, A&A, 421, 241

Setiawan, J. et al. 2007, ApJ, 660, 145

Setiawan, J. et al. 2010, Science, 330, 1642

Siess & Livio 1999, MNRAS, 308, 1133

Smith, P. H., McMillan, R. S., & Merline, W. J. 1987, ApJ, 317, 79

Sneden, C. 1973, ApJ, 184, 839

Sousa, S. G. et al. 2007, A&A, 469, 783

Spronck, J. et al. 2011, AAS Meeting 218, 40903

Stello, D. et al. 2009, MNRAS, 400, 80

Takeda, Y. 1995, PASJ, 47, 337

Takeda, Y., Sato B. & Murata, D. 2008, PASJ, 60 , 781

Tokovinin, A. et al. 2012, in preparation

Toner, C. G. & Gray, D. 1988, ApJ, 334, 1008

Tonry, J & Davis, M. 1979, AJ, 84, 1511

Tuomi, M. et al. 2012, arXiv:1212.4277

Udry S., Mayor M. & Snatos, N. C. 2003, A&A, 407, 369

Unsöld, A. 1955, Physik der Sternatmosphären

Valenti, J. A. and Fischer, D. A. 2005, ApJS, 159, 141

Van Leeuwen, F. 2007, A&A, 474, 653

Villaver, E. & Livio, M. 2009, ApJ, 705, 81

Wolszczan, A. & Frail, D. A. 1992, Nature, 355, 145

Zakamska, N. L. & Tremaine, S. 2004, AJ, 128, 869

Zechmeister, M. et al. 2008, A&A, 491, 531

Zhao Ming et al. 2012, ApJ, 748, 8

Appendix A

Local Thermodynamic Equilibrium

Under LTE the density population of electrons in atoms or molecules is described by the Boltzmann equation, given by:

$$\frac{n_i}{n_j} = \frac{g_i}{g_j} exp\left(\frac{-h\nu}{KT}\right) \tag{A.1}$$

where n_i and n_j are the density of electrons in the energy states i and j and $h\nu$ is the energy difference between both states. T is the temperature, h is the Planck constant and K is the Boltzmann constant. The electron density of a given state, n_i is related to the total density n_{tot} by:

$$\frac{n_i}{n_{tot}} = \frac{g_i}{Z} exp\left(\frac{-\chi_i}{KT}\right) \tag{A.2}$$

where Z correspond to the partition function, given by:

$$Z = \sum g_j exp\left(\frac{-\chi_j}{KT}\right) \tag{A.3}$$

Additionally, when the temperature is high enough so that the ionization of atoms or molecules is significant, the Saha-Boltzmann equation is used to computed the ratio between the density of them in two different stages of ionization. This equation is expressed by:

$$\frac{N_{r+1}}{N_r} N_e = A \frac{Z_{r+1}}{Z_r} exp\left(\frac{-\chi_r}{KT}\right) \tag{A.4}$$

where N_r is the density of particules in the r-th ionization state (i.e. r times ionized), Z$-r$ is the partition function for the atom or molecule in that specific ionization stage and N_e is the total free electron density. The proportional constant is given by:

$$A = \frac{2}{h^3} (2\,\pi\, m\, KT)^{2/3} \tag{A.5}$$

Appendix B

Interpolation Method

In order to determine the mass of the star we searched for the closest models (isomass tracks) in the $T_{\rm eff}$- $\log L$ plane by minimizing the following quantity:

$$\chi^2 = \frac{(T_{\rm eff} - T_{\rm eff}^M)^2}{\sigma_{T_{\rm eff}}^2} + \frac{(L_{bol} - L_{bol}^M)^2}{\sigma_{L_{bol}}^2}, \tag{B.1}$$

where $T_{\rm eff}$ and L_{bol} are the effective temperature and the bolometric luminosity of the star. The quantities carrying an upper script are the corresponding values of the model. The luminosities were derived using the bolometric corrections given in Alonso et al. (1999), and are listed in column 10 of Table 2.2. Since the evolutionary tracks are given for different metallicities, we computed a χ^2 for the two set of models containing the metallicity of the star (Z), i.e., $Z_1^M \leq Z \leq Z_2^M$. Then, we used a linear weighting to determine the total χ^2, by applying:

$$\chi_{tot}^2 = \alpha\chi_1^2 + \beta\chi_2^2 \tag{B.2}$$

where α and β correspond to the statistical weights given by:

$$\alpha = 1 - \frac{Z - Z_1}{Z_2 - Z_1} \qquad \beta = 1 + \frac{Z - Z_2}{Z_2 - Z_1} \tag{B.3}$$

We repeated this procedure for the two isomass tracks that yielded the lowest total χ^2 values ($\chi^2_{tot,1}$ and $\chi^2_{tot,2}$). We finally obtain the mass of the star using a linear weighting of the two closest solutions:

$$M = k_1 M_1 + k_2 M_2 \tag{B.4}$$

where M_1 and M_2 correspond to the mass of the two isomass tracks. The weigthing constants are given by:

$$k_1 = \frac{\chi_1^2}{\chi_1^2 + \chi_2^2} \qquad k_2 = \frac{\chi_2^2}{\chi_1^2 + \chi_2^2} \tag{B.5}$$